Modeling and Analysis of Electrical Network Activity in Neuronal Systems

by

Casey O. Diekman

A dissertation submitted in partial fulfillment
of the requirements for the degree of
Doctor of Philosophy
(Industrial and Operations Engineering and Bioinformatics)
in The University of Michigan
2010

Doctoral Committee:

Associate Professor Daniel B. Forger, Co-Chair
Professor Vijayan N. Nair, Co-Chair
Research Assistant Professor K.P. Unnikrishnan, Co-Chair
Professor Lawrence M. Seiford
Assistant Professor Victoria Booth

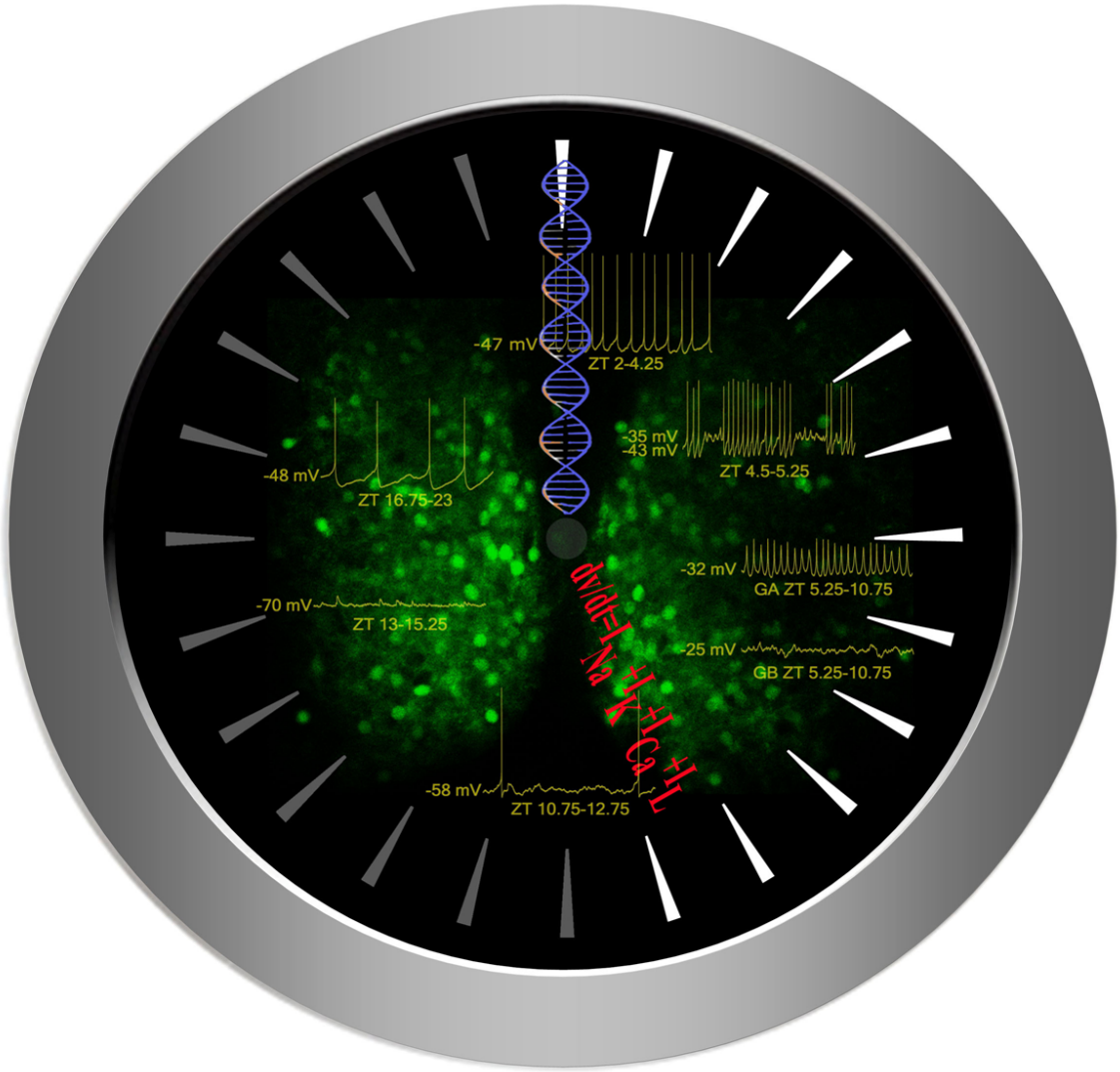
-47 mV
ZT 2-4.25
-35 mV
-43 mV
ZT 4.5-5.25
-48 mV
ZT 16.75-23
-32 mV
GA ZT 5.25-10.75
-70 mV
ZT 13-15.25
-25 mV
GB ZT 5.25-10.75
-58 mV
ZT 10.75-12.75
dv/dt=-I_Na ±I_K ±I_Ca ±I_L

ACKNOWLEDGEMENTS

I have been very fortunate as a graduate student to have had multiple faculty members take me under their wing. Each of the Co-Chairs of my committee has generously devoted much time and effort to my training. I would like to thank Vijay Nair for 6 years worth of advice, dating back to our work together at Chrysler, an experience which was a driving force behind my decision to pursue a PhD at Michigan. Thank you, Vijay, for giving me the freedom to pursue the research topics that fascinated me, for always looking out for my best interests, and, when times were difficult, for reassuring me with the wise words of Jerzy Neyman, that "Life is complicated, but not uninteresting." I would like to thank Daniel Forger for noticing me in his MATH 463 class and for inviting me for a cup of coffee that changed the trajectory of my research career. Thank you, Danny, for encouraging me to pursue a degree in Bioinformatics, for introducing me to the circadian and computational neuroscience fields, and for the countless hours spent advising me on my research and on the academic world in general. I would like to thank K.P. Unnikrishnan for introducing me to the problem of spike train analysis. Thank you, Unni, for sharing with me your enthusiasm for "discovering the neural code" and for graciously integrating me into your research team. And thanks for taking me sailing!

I would like to thank Victoria Booth and Larry Seiford for kindly serving on my committee. Thank you, Victoria, for helpful discussions on neuronal modeling over the years. Thank you, Larry, for all of the support you provided me during your tenure as IOE Department Chair. I would also like to thank Monroe Keyserling and

Dan Burns for making my interdepartmental degree between IOE and Bioinformatics possible. Thank you, Dan, for the guidance and thoughtful advice shared on many different occasions.

I would like to thank Hugh Piggins and Mino Belle for the wonderful collaboration begun during the course of this dissertation. Mino, you are a brilliant scientist and a great friend and I look forward to being involved in many more of your exciting discoveries in the future. I would also like to thank P.S. Sastry, Debprakash Patnaik, Fred Eisele, and Kohinoor Dasgupta for fruitful collaborations. Kohinoor, keep up the good work!

I thank my fellow students in both IOE and Bioinformatics for making my time at Michigan so enjoyable. I also thank the faculty in the mathematical biology community, especially Richard Yamada, Cecilia Diniz Behn and Santiago Schnell, for various opportunities and pieces of advice that they have given me. I thank the staffs of IOE and Bioinformatics, especially Tina Blay, for all their help and for creating such welcoming environments. I would also like to recognize the National Science Foundation and the Air Force Office of Scientific Research for their funding support.

My deepest thanks go to my family, whose love and encouragement I can always count on. Mom and Dad, it is amazing to me how faithfully you have supported me in every way imaginable, without fail, my entire life. Brian, it has been fun going through graduate school at the same time as you, thanks for sharing your experiences and the lessons you have learned along the way with me. Rachel, thank you for your incredible patience and understanding these last 4 years– and going forward!

PREFACE

The work in Chapters 2 through 4 of this dissertation was advised by Daniel Forger. Chapter 2 was previously published as: Diekman CO and Forger DB, *Journal of Biological Rhythms* **24**:322-333 (2009). Chapters 3 and 4 involved a collaboration with Mino Belle and Hugh Piggins of the University of Manchester, and Chapter 3 appeared as part of: Belle MDC, Diekman CO, Forger DB, and Piggins HD, *Science* **326**:281-284 (2009).

The work in Chapters 5 and 6 was advised by Vijay Nair and K.P. Unnikrishnan. Chapter 5 involved a collaboration with P.S. Sastry of the Indian Institute of Science, and was previously published as: Diekman CO, Sastry PS, and Unnikrishnan KP, *Journal of Neuroscience Methods* **182**:279-284 (2009). The work in Chapter 6 involved a collaboration with Kohinoor Dasgupta, and will be submitted for publication as: Diekman CO, Dasgupta K, Nair VN, and Unnikrishnan KP (2010).

TABLE OF CONTENTS

LIST OF FIGURES

Figure

LIST OF TABLES

Table

LIST OF APPENDICES

Appendix

CHAPTER I

Introduction

Electrical activity in networks of neurons is an essential part of most brain functions. In Part I of this dissertation, we focus on the particular brain function of biological timekeeping, and develop the first detailed mathematical model of the electrophysiology of the specific neuronal network responsible for the generation of circadian (∼24-hour) rhythms in mammals. In Part II of this dissertation, we develop a new statistical method for inferring the functional connectivity of neuronal networks from multi-neuronal spike trains that is applicable in many different brain areas.

1.1 Part I

Circadian rhythms are 24-hour oscillations in physiological processes and behavior, such as metabolism and the sleep/wake cycle. Disruption of the circadian system due to night-shift work or travel across time zones (jet lag) can cause negative health effects such as sleep disorders, and has also been linked to higher rates of cancer, bipolar disorder, and Alzheimer's disease. Mammalian circadian rhythms are controlled by a group of about 20,000 neurons in the hypothalamus called the suprachiasmatic nucleus (SCN). While individual SCN neurons can have an internal molecular clock mechanism consisting of clock genes and transcriptional/translational feedback loops, SCN neurons are also coupled to each other and it is their electrical activity that sends

the timing signal to other brain regions.

In Chapter 2, we develop a model of action potential firing in the SCN network. With this model we can simulate and track the action potentials of thousands of model SCN neurons, while experimentally it is only possible to record the activity of a few dozen SCN neurons at the same time. Our simulations predict that subgroups, or clusters, of SCN neurons form within which neurons synchronize their firing at a millisecond time scale. Furthermore, our simulations demonstrate how this clustering leads to the silencing or adjustment of neurons whose firing is out of phase with the rest of the population at the 24-hour time scale, giving insight into how the circadian clock may operate at the network level.

In Chapter 3, we explore a prediction of our model that SCN neurons can exhibit unusual depolarized states. This prediction has been verified by experimental recordings, and we use the model to show that the observed electrical behaviors can be explained by existing data on ionic currents measured within SCN neurons. These behaviors are surprising as they run counter to the traditional view that SCN neurons express time of day by changing their firing frequency, with high rates during the day and lower rates at night. We find that clock-containing SCN neurons are actually not firing at all during the afternoon, when they were thought to be firing the fastest.

In Chapter 4, we refine our model to gain insight into these depolarized states. We make predictions regarding their role in intercellular communication within the SCN, and in the ability of external light input to phase shift the circadian clock.

1.2 Part II

In multi-neuronal recordings from other brain areas, precise firing sequences with fixed time delays between neurons have been observed. To determine whether the detected temporal patterns of firing are meaningful, it is important to know whether they are occurring more or less often than would be expected due to chance alone.

To address this question, we have developed statistical methods for assessing when the number of occurrences of precise firing sequences is significant. The significant patterns discovered in multi-neuronal data can be used to infer the functional connectivity between neurons, and potentially represent circuits in the underlying neural tissue.

In Chapter 5, we develop a method for analyzing the significance of sequential firing patterns that goes beyond the currently available techniques by allowing the null hypothesis to include "weak dependence" among neurons and by rank ordering significant patterns according to the "strength of influence" among participating neurons. We demonstrate the effectiveness of our method on simulated neuronal networks.

In Chapter 6, we develop a method for assessing significant patterns when we do not have a count of all the occurrences of a pattern, but rather a count for a certain well-defined subset called the "non-overlapped" occurrences. The motivation for this work is that a class of data mining algorithms has recently been shown to be able to efficiently obtain the non-overlapped counts. Since our approach is computationally efficient, we can detect significant patterns involving many neurons whereas previous methods were limited to patterns involving only a few neurons. We demonstrate the effectiveness of our method on simulated neuronal networks, and then apply the method to discover the significant connections in spike train data from cultures of cortical neurons.

CHAPTER II

Clustering predicted by an electrophysiological model of the suprachiasmatic nucleus

2.1 Introduction

Circadian (∼24-hour) clocks within cells time many biological processes in a broad range of organisms. In mammals, timing is coordinated by the bilateral suprachiasmatic nuclei (SCN) of the hypothalamus. This neuronal network processes signals from the body and the external world, coordinates intracellular rhythms throughout the SCN, and sends signals to the rest of the body to time rhythms in other tissues. While the majority of recent circadian research has focused on the intracellular events that generate timekeeping, there is a growing interest in the network behavior of the SCN (*Herzog*, 2007); (*Liu et al.*, 2007); (*Freeman et al.*, 2008). This network operates on multiple scales, as each unilateral SCN contains approximately 10,000 heterogeneous neurons which control rhythms on the time scale of 24 hours by the generation of action potentials on time scales quicker than a second.

Because of the complexity of the SCN, many researchers have turned to mathematical modeling to help understand its behavior. Several mathematical models exist for the intracellular generation of circadian rhythms (*Leloup and Goldbeter*, 2003; *Forger and Peskin*, 2003, 2005; *Forger et al.*, 2007) and for the behavior of the

overall circadian system (*Daan and Berde*, 1978; *Kronauer et al.*, 1999; *Forger et al.*, 1999). Recent modeling work has focused on the synchronization of cellular clocks within the SCN on a 24-hour time scale (*Indic et al.*, 2007, 2008; *To et al.*, 2007; *Bernard et al.*, 2007; *Gonze et al.*, 2005; *Bush and Siegelman*, 2006) and is part of a growing field studying coupled oscillators (*Strogatz*, 2000). However, none of these aforementioned studies explicitly model the generation of action potentials by SCN neurons.

Mathematical modeling has also become an established tool for understanding the firing behavior of neurons, beginning with the publication of the Hodgkin-Huxley model of action potential generation in the squid giant axon (*Hodgkin and Huxley*, 1952). Despite the wealth of experimental data on the electrical activity of SCN neurons, and the well-established modeling techniques in the field of computational neuroscience, modeling the electrical activity of the SCN is relatively new. A Hodgkin-Huxley-type model for the electrical behavior of a single SCN neuron has recently been developed (*Sim and Forger*, 2007). Here, we use this model to generate the first detailed mathematical model of the electrical activity of the SCN at the tissue level.

The electrical activity of the model SCN could be studied on multiple time scales. One could focus on the 24-hour time scale and coarse changes in the frequency of neuronal firing. On this slow time scale, the model would be similar to previous studies (*Rohling et al.*, 2006a,b; *Brown and Piggins*, 2009). Instead, we focus on the electrical activity over a shorter time scale (up to 1 minute), where the circadian clock within individual neurons can be thought of as occupying a set circadian phase. Thus, we are interested in the specific neuronal signals which encode a set circadian phase, analogous to the position of hands on a clock. Even the dynamics of neuropeptides such as vasoactive intestinal peptide (VIP), which can synchronize 24-hour rhythms (*Aton et al.*, 2005), are likely slow on this fast time scale (*Pakhotin et al.*, 2006). On this fast time scale, our model can predict the activity of every neuron within

the network. We will study the patterns that emerge, including synchronous or asynchronous firing of action potentials across the network. Since we will discuss both the phase of circadian rhythms (time scale of hours) and the phase of neuronal firing (time scale of seconds), we will use the term "circadian phase" to refer to the former and the term "neuronal phase" to refer to the latter in order to delineate these two cases.

Several neurotransmitters have been proposed as candidate synchronizing factors within the SCN, such as VIP, gastrin-releasing peptide (GRP), and γ-aminobutyric acid (GABA). Of these, only GABA is synthesized by most, if not all, SCN neurons (*Aton and Herzog*, 2005). GABA receptors are also found all throughout the SCN, and, while GABA is known to mediate predominantly inhibitory postsynaptic currents, there is also evidence that GABA can be excitatory in the SCN (*Choi et al.*, 2008). In this chapter we use a mathematical model of the electrophysiology of SCN neurons in a network with fast $GABA_A$ inhibition and excitation to predict the electrical activity of the SCN. Since current experimental techniques can only record from a small percentage of SCN neurons, this model gives the first glimpse of the electrical activity of all SCN neurons simultaneously.

2.2 Methods

2.2.1 Network model

We simulated the electrophysiology of the SCN using networks of N=10,000 interconnected SCN neurons. The dynamics of each neuron i, $i = 1, \ldots, N$, was modeled using the Hodgkin-Huxley formalism including sodium, potassium, calcium, background, and synaptic currents as in *Sim and Forger* (2007). The model equations for the i^{th} neuron were:

$$C\frac{dV_i}{dt} = g_{Na}m_i^3h_i(E_{Na}-V_i)+g_Kn_i^4(E_K-V_i)+g_{Ca}r_if_i(E_{Ca_i}-V_i)+g_L(E_L-V_i)+I_{syn_i}(t)$$

$$\frac{dq_i}{dt} = \frac{q_{i,\infty}-q_i}{\tau_{q_i}} \qquad q_i = m_i, h_i, n_i, r_i, f_i \tag{2.1}$$

The model parameters were taken from the literature or fit to experimental data on individual ionic currents within SCN neurons (see *Sim and Forger* (2007) for a complete description of the model formulation). All parameter values used in this chapter are given in Appendix A and were identical to *Sim and Forger* (2007), except for the equilibrium values of the sodium gating variables m_∞ and h_∞, which were given slightly modified forms based on re-evaluation of experimental data (data not shown):

$$m_{i,\infty} = \frac{1}{1+exp(-\frac{V_i+35.2}{8.1})} \tag{2.2}$$

$$h_{i,\infty} = \frac{1}{1+exp(\frac{V_i+62}{4})} \tag{2.3}$$

However, we note that all of the behaviors reported in this chapter can be obtained using the m_∞ and h_∞ functions that originally appeared in *Sim and Forger* (2007) as well (data not shown).

To model inhibitory $GABA_A$ coupling in the SCN, we induce an inhibitory current in all neurons which are postsynaptic to a neuron that just fired. We based the form of this inhibitory postsynaptic current (IPSC) on experimental measurements of spontaneous inhibitory postsynaptic potentials (IPSPs) recorded in SCN neurons (*Kim and Dudek*, 1992). On average, the spontaneous IPSPs reported in *Kim and Dudek* (1992) had a rise-to-peak time of 7.2 ms and a decay time constant of 14

ms. To produce IPSPs with a similar decay in our model, we use IPSCs that decay exponentially with a time constant of 2 ms. Since the rise time of IPSPs is fast compared to their decay, we assume the rise of the IPSCs are instantaneous to gain computational efficiency. The coupling among SCN neurons is implemented through the synaptic current $I_{syn}(t)$:

$$I_{syn_i}(t) = -g_{syn} \sum_{j=1}^{N} \sum_{k} c_{ij} exp(-(t - t_{j,k})/2) \tag{2.4}$$

The coupling strength is set by the parameter g_{syn} (higher g_{syn} values result in larger amplitude postsynaptic currents). The binary matrix c keeps track of which neurons are connected (c_{ij}=1 if neuron j is presynaptic to neuron i and 0 otherwise, $j = 1, \ldots, N$), and $t_{j,k}$ is the time of the k^{th} spike from cell j. By specifying the connectivity matrix in different ways, we simulated different types of connectivity in the SCN. For example, to simulate all-to-all coupling (every SCN neuron connected to every other SCN neuron), we set c_{ij}=1 for all i, j. For sparse connectivity, for each neuron we randomly choose a subset of the N neurons as presynaptic to that neuron (e.g. to simulate 10,000 neurons with 10% connectivity, for each i we set c_{ij}=1 for 1,000 randomly chosen j's). To simulate an uncoupled network, we set c_{ij}=0 for all i, j (or alternatively we set g_{syn}=0). To model excitatory $GABA_A$ coupling in the SCN, we simply reverse the sign of all synaptic currents entering a subset of the neurons. All simulations and analysis were conducted using C and MATLAB R2007a (The Mathworks Inc., Natick, MA). The equations were solved using a fifth-order Runge-Kutta method with adaptive stepsize control (*Press et al.*, 1992) and a maximum time step of 1 ms.

2.2.2 Neuronal heterogeneity

Dissociated SCN neurons grown in low-density cultures maintain circadian rhythms in their electrical activity, but the circadian phase is not synchronized across neurons

(*Welsh et al.*, 1995). Thus at any given point of time, the state of the intracellular clock within each neuron is not identical throughout the population. Moreover, since the concentration of intracellular calcium, $[Ca^{2+}]_i$, is under the control of the clock (*Ikeda et al.*, 2003), we would expect there to be variation in the levels of $[Ca^{2+}]_i$ across a population of isolated neurons as a function of the circadian phase of their intracellular clocks. Since $[Ca^{2+}]_i$ is related to the model parameter E_{Ca} (the equilibrium potential for calcium) through the Nernst equation, we simulate this heterogeneity by assigning different values of E_{Ca} to the neurons in our network. We take each neuron's $E_{Ca,i}$ from a normal distribution with a mean of 61 mV and a standard deviation of $\sigma_{E_{Ca}}$. This gives each neuron a slightly different intrinsic firing frequency. To simulate identical neurons, we set $\sigma_{E_{Ca}}$=0.

Although the intracellular calcium concentration is not the only factor that contributes to the heterogeneity of SCN cells, we find that varying $[Ca^{2+}]_i$ alone is sufficient to create significant changes in the intrinsic firing rate of our model SCN neurons. Alternatively, variations in calcium channel conductance (g_{Ca}) or potassium channel conductance (g_K) could be used to alter firing rates in the model as shown in *Sim and Forger* (2007).

2.2.3 Noise mechanisms

Synaptic transmission can be a highly unreliable process, with the probability of neurotransmitter release at an individual synapse ranging from 0.1 to 0.9 in central neurons *in vitro* (*Koch*, 1999). We simulate this type of synaptic noise by treating synaptic transmission as a binary event with a probability of success p. Whenever a presynaptic neuron fires a spike, for each postsynaptic neuron we draw a random number q from a (0,1) uniform distribution, and if $q \leq p$ we induce a postsynaptic current in that neuron. Setting p=1 makes synaptic transmission 100% reliable, while setting p=0 corresponds to uncoupled neurons.

In addition to synaptic transmission being a probabilistic event, there is also randomness in the amplitude of the postsynaptic response. In a study of a rat neocortical pyramidal cell, the variance in the size of evoked postsynaptic potentials was as large as the mean (*Koch*, 1999). To incorporate this type of variability in our simulations, for each successful synaptic transmission we randomly choose the synaptic conductance for that event to be anywhere in the interval $[g_{syn} \pm k \times g_{syn}/2]$. Setting k=0 corresponds to no randomness in the amplitude of postsynaptic currents. In this chapter we limit ourselves to $k \leq 1$.

2.2.4 Order parameters

To quantify the synchrony of a population of spiking neurons, we compute an order parameter R (*Garcia-Ojalvo et al.*, 2004; *Golomb and Rinzel*, 1994). *Golomb and Rinzel* (1994) defined the order parameter as the ratio of the time-averaged fluctuations of the population-averaged voltage across all N neurons, $V(t) = \frac{1}{N}\sum_{i=1}^{N} V_i(t)$, over the population average of each cell's time-averaged V_i fluctuations:

$$R = \frac{var(V)}{\frac{1}{N}\sum_{i=1}^{N} var(V_i)} \tag{2.5}$$

If the population is completely disordered then $R \approx 0$, on the other hand if the population is fully synchronized then $R \approx 1$. An intermediate R value indicates partial synchronization.

In addition to R, we also calculate the higher-order parameters, z_n, which detect the segregation of a population of coupled oscillator into n clusters as described in *Golomb and Hansel* (2000):

$$z_n = \frac{1}{N}\sum_{i=1}^{N} e^{in\phi_i} \tag{2.6}$$

where ϕ_i is the neuronal phase of the i^{th} neuron (defined below). For example, if a

population forms 3 equally sized clusters oscillating 1/3 out of neuronal phase with each other, then z_1=z_2=0 while z_3=1. We define ϕ_i as:

$$\phi_i(t) = \left(\frac{t - t_{lap}}{t_{nap} - t_{lap}} \right) \times 2\pi \tag{2.7}$$

where t_{lap} is the time of the last action potential from neuron i before t, and t_{nap} is the time of the next action potential from neuron i after t. Neurons which did not fire were excluded from higher-order parameter analyses.

2.3 Results

Here, we describe results from simulations that predict the electrical activity of the SCN. Our simulations contained 10,000 individual SCN neurons which communicated via inhibitory GABA postsynaptic potentials. Inhibitory coupling did not lead to desynchronized firing throughout the SCN, rather we found that large "clusters" of SCN neurons fired synchronously (e.g. see Fig. 2.1B-C).

We then studied how the clustering depends on network properties such as the synaptic strength and density, as well as the amount of heterogeneity in the neuronal population. Our simulations tracked the electrical behavior of every SCN neuron within a lobe. Since it is only possible to experimentally record from 100 or fewer of the 10,000 SCN neurons, we make testable predictions about the clustering of electrical activity in recordings from a small number of neurons by analyzing the behavior of 100 neurons randomly sampled from the 10,000 neurons in our simulations.

2.3.1 Order and Disorder in the SCN

Simulation of 10,000 uncoupled SCN neurons (g_{syn}=0) with random initial states showed spontaneous, desynchronized firing. In these uncoupled network simulations, we found no evidence of coordinated firing throughout the SCN (see Fig. 2.1A-B).

This disordered state was characterized by an order parameter near zero (R=1.35E-4 ± 3.39E-5, mean ± SD of 100 simulations for the uncoupled case with different initial conditions). To simulate the effect of fast $GABA_A$ inhibitory post-synaptic potentials, the most prevalent signal among SCN neurons, we modeled inhibitory coupling between SCN neurons. Our initial simulations coupled each neuron to all other neurons (all-to-all coupling). While neurons in these simulations started in random initial states, we found that coordinated behavior emerged within the first few seconds of the simulations. The inhibitory coupling caused the formation of clusters where large fractions of the SCN fired synchronously. Given sufficient time, we found that this clustered firing behavior occurred for all coupling strengths. Figure 2.1C-F shows this behavior for two coupling strengths. In each case, three groups of firing neurons were formed and the time between the firing of each cluster was approximately constant. Here, the order parameter R was approximately 1/3, which indicated partial synchronization and also suggested the presence of three synchronously firing groups (R=0.29 ± 5.91E-4 over 100 simulation replications with g_{syn}=0.001). We verified the existence of a 3-cluster state visually using the voltage traces and by calculating higher-order parameters z_1 through z_5 (e.g. see Figures 2.1 and 2.2). We consistently found agreement between the clustered state seen visually and the values of R and higher-order parameters. We also noticed that the order parameter decreased slightly for the higher coupling strength (R=0.27 ± 5.91E-4 over 100 simulation replications with g_{syn}=0.01). In this case the SCN was divided into four clusters, three clusters firing out of neuronal phase with the other clusters and a fourth group of neurons that did not fire. These results led us to hypothesize that $GABA_A$ coupling could indeed produce an ordered state of the SCN.

At both coupling strengths, we found that the size of the clusters varied depending on initial conditions. For example, with g_{syn}=0.001 the size of the largest of the three clusters ranged from 3,379 to 3,459 while the size of the smallest cluster ranged from

3,194 to 3,286 over the 100 simulation replications. With g_{syn}=0.01, the number of neurons that were silenced ranged from 1,376 to 2,178.

2.3.2 Exploring Network Properties of the SCN

Many of the network properties of the SCN, such as the coupling strength and the degree of connectivity, are difficult to measure experimentally. We can explore such properties using our model, and determine if the clustering behavior persists for a wide enough range of parameter values to include those likely present in the SCN. We first lowered the coupling strength (Fig. 2.2A-B) and found that even at very low coupling strengths (e.g. 100 fold less than those used in Fig. 2.1E-F), clustering of neuronal states still emerged. The transition from a disordered state to an ordered state was delayed by up to a minute at low coupling values. Figure 2.2B shows a network that is transitioning to the ordered state and the consolidation of spikes into a cluster. We also explored higher coupling strengths, and found that for $g_{syn} \geq$0.1 all-to-all coupling produced large hyperpolarizations of the membrane (data not shown).

In the actual SCN, a given neuron only synapses onto a fraction of other SCN neurons. To explore the effect of partial connectivity, we performed a series of simulations with increasing connectivity, beginning with simulations where each neuron synapses onto just 1% of the network up to simulations with 99% connectivity. In each simulation the specific synaptic connections were chosen randomly. For each connected SCN, we also simulated a variety of coupling strengths. At the moderate and high coupling strengths, clusters began forming within the first 60 seconds of simulation with network connectivity as low as 5-10% (Fig. 2.2C). At low coupling strength and low connectivity, clustering was not observed during the first 60 seconds of simulation (Fig. 2.2C), but clusters did form after a long initial transient (data not shown) similar to the simulations shown in Fig. 2.2A.

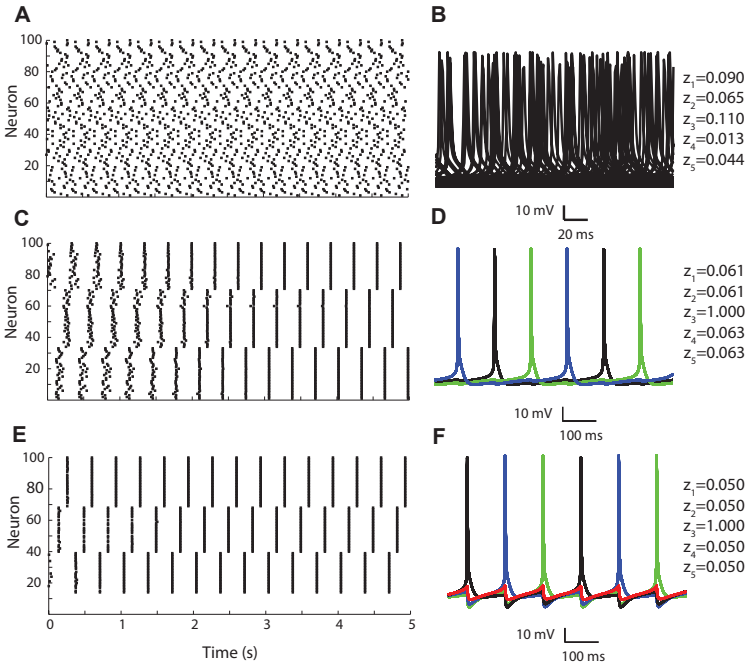

Figure 2.1: Formation of clusters in simulations of 10,000 homogeneous suprachiasmatic nuclei neurons. (**A,B**) Uncoupled neurons. (**A**) Spike raster of 100 randomly chosen neurons demonstrate that without coupling each neuron spikes regularly with its phase dependent only on initial conditions. No patterns in spike timings across the population are evident. (**B**) Voltage traces of the 100 neurons for the 20th second of simulation. Order parameter $R \approx 0$ and low values of the higher-order parameters (z_1 through z_5 at t=19 sec) indicate the voltage trajectories are completely asynchronous. (**C,D**) Inhibitory all-to-all coupling, g_{syn}=0.001. Neurons quickly segregate into 3 clusters; within each cluster all neurons spike in synchrony and follow the same voltage trajectory. (**D**) The blue, black, and green clusters contain 3406, 3364, and 3230 neurons, respectively. The presence of 3 clusters is confirmed by the higher-order parameter z_3=1.00 at t=19 sec. The 3 clusters themselves fire out of phase with each other, resulting in an R value around 0.29. (**E,F**) Inhibitory all-to-all coupling, g_{syn}=0.01. Neurons almost immediately segregate into 4 clusters, 3 of which consist of spiking neurons while the neurons in the 4th cluster never spike. (**F**) The blue, black, green, and red clusters contain 2865, 2844, 2793, and 1498 neurons, respectively. z_3=1.00 at t=19 sec (calculated based on the phases of spiking neurons only) confirms there are 3 clusters of spiking neurons. The presence of the silenced cluster leads to a slightly lower R value (0.27) than the 3-cluster state.

Recordings from small populations of SCN neurons show that at a given time of day there is heterogeneity in the firing frequencies of individual neurons (*Brown and Piggins*, 2007). We simulate heterogeneity in firing frequency through variation in the equilibrium potential for calcium (E_{Ca}) of the neurons. The rationale for this approach is that E_{Ca} is related to the intracellular calcium concentration of SCN neurons, which has been demonstrated to be under the control of the circadian clock (*Ikeda et al.*, 2003). Moreover, a study by *Quintero et al.* (2003) suggests a correlation between the firing frequency of a SCN neuron and the state of its intracellular clock (*Brown and Piggins*, 2007). By allowing different values of E_{Ca} for the neurons in our simulation, each neuron has slightly different dynamics and firing frequency corresponding to the circadian phase of its intracellular clock. When these heterogeneous SCN neurons were simulated, we found that clustering could still occur. However, larger amounts of heterogeneity required larger coupling strengths for clustering (Fig. 2.2E). The firing within clusters from the heterogeneous network was not perfectly synchronized, referred to as "smeared clusters" (*Golomb and Hansel*, 2000), and not all neurons were firing as part of a cluster during the 60th second of simulation (Fig. 2.2F). This explains why the order parameters for these simulations were below 1/3.

While the majority of GABA transmissions between SCN neurons are inhibitory, excitatory effects of GABA have been reported in a minority (less than 25%) of SCN neurons (*Choi et al.*, 2008). To test whether such excitatory responses affect the behavior of our network simulations, we had GABA induce EPSPs rather than IPSPs in a subset of the neurons in our network. Even if 25% of the neurons responded to GABA with excitation, the network simulations and clustering behavior were relatively unaffected. However, if the majority of connections were excitatory, the network could organize into a state where all neurons fire synchronously in one cluster (data not shown). Interestingly, having an excitatory effect of GABA on a minority of neurons in the network seems to lead to increased coherence within the clusters

compared to an all-inhibitory network (compare Fig. 2.2F and 2.3B) suggesting a possible functional role for excitatory GABA in the SCN.

2.3.3 Dynamic Clustering in the SCN

A morphometric study by *Guldner* (1984) estimated an average of 11,900 neurons and 1,264 synaptic appositions per neuron in the SCN of female rats. Based on this experimental estimate, we, from now on, examine closely the results of simulations with 10% connectivity in order to predict the firing behavior of the SCN. In simulations with 10% connectivity and heterogeneity ($\sigma_{E_{Ca}}$=0.5), we detected the presence of clusters with near synchronous firing by calculating the instantaneous firing rate of the population (the total number of spikes being fired across the SCN in each millisecond) as shown in Figs. 2.4A-B. Without coupling (g_{syn}=0), there was a relatively constant low level of firing across the network throughout time (Fig. 2.4A). With coupling (g_{syn}=0.1), there were extended periods of inactivity with very little firing across the network punctuated by bursts of 500 or more neurons firing synchronously (Fig. 2.4B). Each time a cluster fired, the total number of neurons firing together was not necessarily the same as in the previous firing of that cluster (Fig. 2.4B). This behavior can be understood via the raster plot in Fig. 2.4C, showing spiking from 100 neurons randomly chosen from the network. The neurons are sorted vertically according to their earliest spike time (after the 15th second) to make the three clusters clearly visible. The membership of the clusters was not constant but rather changed over time, referred to as "dynamic clustering" (*Terman et al.*, 2008). A few examples of individual neurons that do not reliably fire within the same cluster throughout the 5 seconds of simulation are shown in Fig. 2.4C: (1) neuron 57 originally fired with the middle cluster, but after two cycles it switched and joined the bottom cluster; (2) neuron 78 initially fired with the top cluster, but did not fire in the last several cycles; and (3) neuron 25 was silent for the first 14 cycles, but then

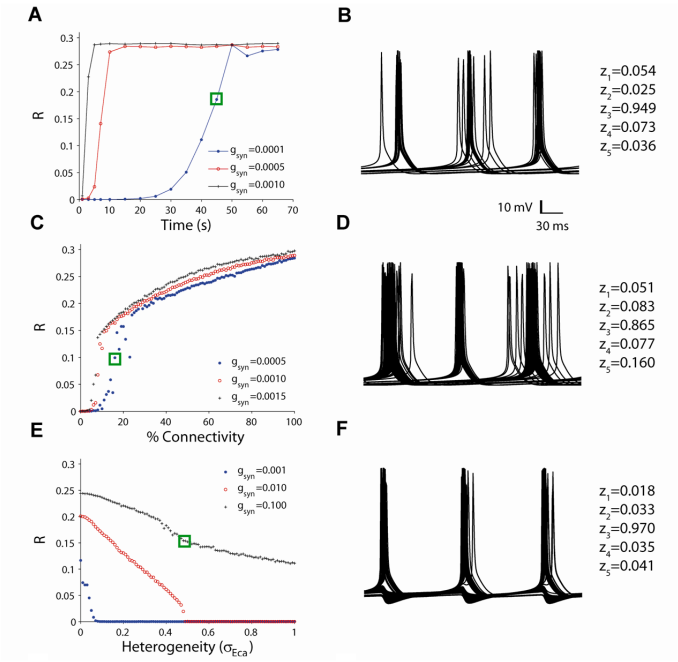

Figure 2.2: Clustering depends on network properties. (**A,C,E**) Each R value is computed for the 60th second of a 10,000 neuron simulation. In A-D the neuronal population is homogeneous. (**A**) As the coupling strength (g_{syn}) decreases, it takes longer for the 3-cluster state to form ($R \approx 0.3$). Simulations are with all-to-all coupling. (**B**) Voltage traces of 100 randomly chosen neurons for the 45th second of simulation with g_{syn}=0.0001 and z_3=0.95 at t=44 seconds indicate that the network is transitioning to the 3-cluster state but that some neurons have not yet joined a cluster. (**C**) The synaptic density (% connectivity) of the network affects the degree of clustering. With very low connectivity, the network behaves as if the neurons are uncoupled. For each coupling strength (g_{syn}), as the connectivity is increased there appears to be a value at which the network transitions from a disordered state ($R \approx 0$) to one that exhibits some order ($R > 0$). As the connectivity approaches 100% (all-to-all coupling), the network goes to the 3-cluster state ($R \approx 0.3$). At lower connectivities, R values close to 0.3 are occasionally seen for certain initial conditions (data not shown). (**D**) Voltage traces of 100 neurons randomly chosen from a network with g_{syn}=0.0005 and 16% connectivity show 3 clusters still in the process of forming (z_3=0.87 at t=59 sec). (**E**) As the amount of heterogeneity in the intrinsic firing rate and dynamics of the neuronal population ($\sigma_{E_{Ca}}$) is increased, the degree of order in the network decreases. Simulations are with 10% connectivity. (**F**) Clustering is still evident in a network with g_{syn}=0.1, 10% connectivity, and $\sigma_{E_{Ca}}$=0.5 (z_3=0.97 at t=59 sec).

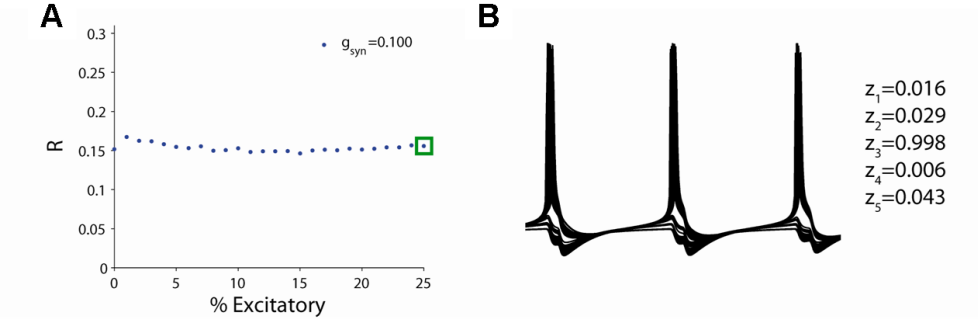

Figure 2.3: Clustering persists in the presence of some excitatory connections. (**A**) Each R value is computed for the 60th second of a 10,000 neuron simulation. As the percentage of neurons in the network that respond to GABA with excitation rather than inhibition is increased from 0 to 25%, little effect is seen on the clustering behavior (R nearly constant). Simulations are with 10% connectivity and $\sigma_{E_{Ca}}$=0.5. (**B**) The coherence of neurons within each cluster appears to be enhanced by including excitatory effects of GABA in 25% of neurons in the network compared with the all-inhibitory network of Fig. 2.2F (z_3=1.00 at t=59 sec).

fired with the bottom cluster in the last two cycles.

2.3.4 Output Signal of the SCN

The clustering of SCN neurons has a major effect on the firing rate of individual neurons, which is the main output signal of the SCN. When uncoupled, simulated heterogeneous neurons fired regularly between 3 and 3.9 Hz (firing rates approximately normally distributed, 3.45 $\pm$ 0.11 Hz). When coupled, the majority of neurons ($\sim$6,000) fired at around 3 Hz, but a substantial portion ($\sim$2,000 neurons) were silenced. The remaining neurons fired at rates anywhere between 0 and 3 Hz. By comparing an individual neuron's firing rate when uncoupled to its firing rate in the coupled network, we see that neurons with lower intrinsic firing rates are silenced (compare Fig. 2.5A and C). Also, neurons that have higher intrinsic firing rates are slowed down to 3 Hz (compare Fig. 2.5B and D). Thus, the coupling and the resulting clustering of SCN neurons allows the majority of heterogeneous SCN neurons to

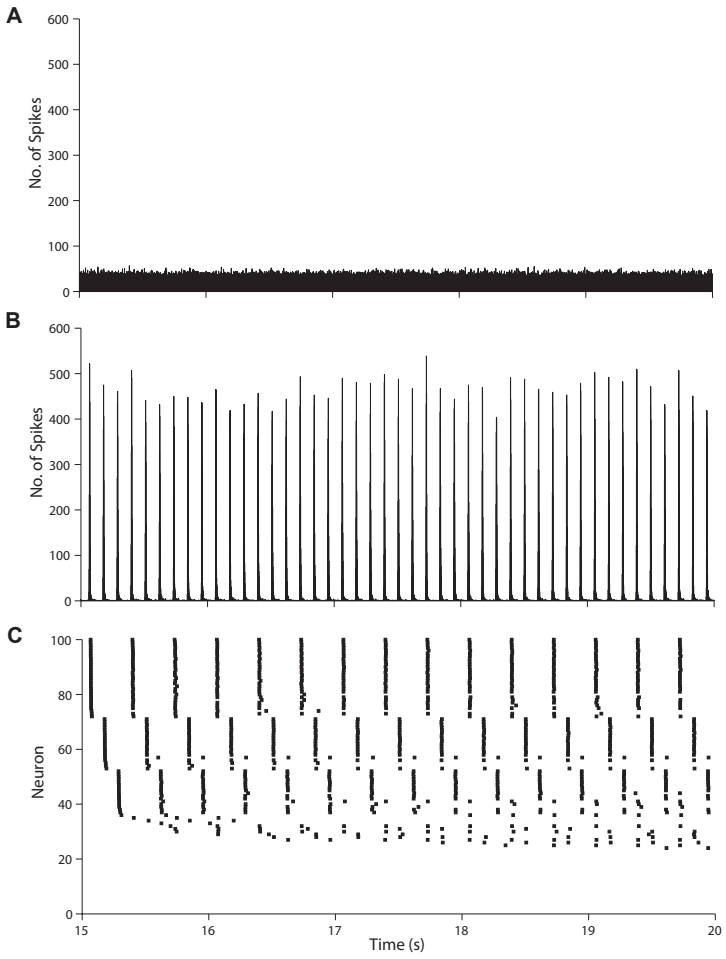

Figure 2.4: Dynamic clustering in a 10,000 neuron network with sparse coupling and heterogeneity. (**A**) Uncoupled neurons with heterogeneity. The instantaneous firing rate of the population, calculated as the number of action potentials per millisecond, randomly fluctuates around a mean value of 50 throughout the simulation. (**B**) Sparse coupling (10% connectivity, g_{syn}=0.1) with heterogeneity (σ_{ECa}=0.5). The instantaneous firing rate of the population is near zero for most of the time bins, punctuated by bursts of activity where up to 500 neurons fire in the same millisecond time bin. (**C**) The spike raster of 100 randomly chosen neurons reveals that these bursts of spiking activity correspond to three clusters of neurons. However, unlike the clusters in homogeneous networks with all-to-all coupling, the size and membership of the clusters in heterogenous networks with sparse coupling are not constant over time. The neurons are sorted vertically so that during the 15th second of simulation the neurons that spike together in a cluster are plotted contiguously. Neuron 57 is initially in the middle cluster but by the 16th second of simulation has joined the bottom cluster. Neuron 78 initially fires with the top cluster 4 out of 5 cycles but then does not fire during the next 3 seconds of simulation. Neurons 1 through 24 do not fire at all during these five seconds of simulation.

agree on a single firing rate (interquartile range of firing rates was 0.1 Hz for neurons in Fig. 2.5B and 0 Hz for neurons in Fig. 2.5D), while most neurons that are too slow to keep up with this rate are silenced. Presumably this coordination of firing rates strengthens the output signal of the SCN in order to more reliably time rhythms throughout the body.

We also computed interspike interval (ISI) histograms (Fig. 2.5E-F) for individual neurons in a coupled simulation in order to compare to previously published experimental data on SCN firing. In *Kononenko and Dudek* (2004), recordings from neurons in slices of rat SCN revealed two distinct firing behaviors for SCN neurons. Some of the neurons they recorded from exhibited "regular" firing, characterized by an approximately normal ISI distribution, while other SCN neurons exhibited slower "irregular" firing, characterized by a skewed ISI distribution with a long right tail. We find both of these behaviors in our network simulations: a neuron firing regularly at ∼3 Hz shows an approximately normal ISI distribution (Fig. 2.4F) while a neuron firing irregularly at ∼0.5 Hz exhibits a skewed ISI distribution (Fig. 2.5E).

2.3.5 Clustering in the Presence of Synaptic Noise

Synaptic transmission is stochastic and not 100% reliable (*Koch*, 1999). To investigate the effect of this stochasticity on the coupled network, we simulated synaptic noise by varying the probability with which presynaptic spikes resulted in a postsynaptic current (Fig. 2.6A). We also incorporated variation in the magnitude of the postsynaptic currents in response to a presynaptic spike (Fig. 2.6B). Even when both of these sources of noise are present, the instantaneous firing rate of the population indicates that clustering still persists (Fig. 2.6C). Since we find clustering in a noisy network of sparsely connected heterogeneous SCN neurons, we predict that clustering may indeed be occurring in the SCN *in vivo*.

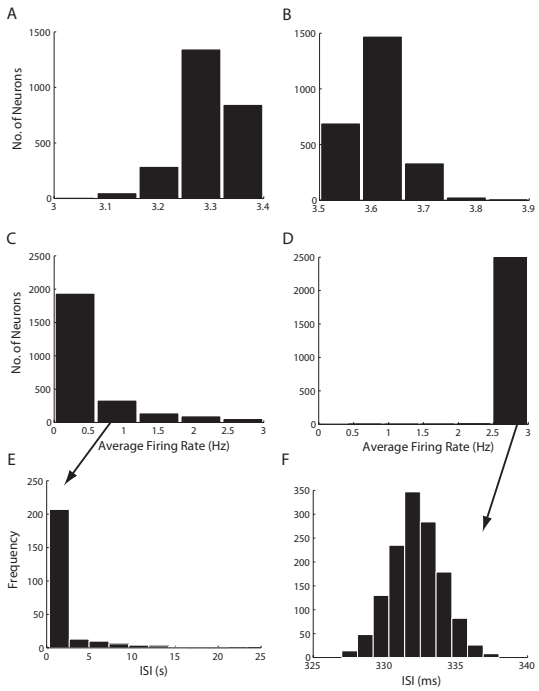

Figure 2.5: Effect of dynamic clustering on the output signal of the SCN. (**A-B**) 10,000 uncoupled neurons (same simulation as Fig. 2.4A). The firing rates of individual neurons (averaged over the last 10 seconds of simulation) are normally distributed due to heterogeneity in the equilibrium potential for calcium (E_{Ca}) across the network. (**A**) Histogram of the firing rates for the 2,500 neurons with the slowest intrinsic firing rate (E_{Ca} $\leq$60.66 mV). (**B**) Histogram of the firing rates for the 2,500 neurons with the fastest intrinsic firing rate (E_{Ca} $\geq$61.33 mV). (**C-D**) Sparse coupling (10% connectivity, g_{syn}=0.1) with heterogeneity ($\sigma_{E_{Ca}}$=0.5) (same simulation as Fig. 2.4B). Around 6,000 neurons fire regularly with a cluster at around 3 Hz while almost 2,000 are silenced. The remaining neurons have intermediate firing rates due to switching between clusters or being silenced transiently. The neurons that have slower intrinsic firing rates (due to the state of their intracellular clock) tend to be silenced by the network, while neurons with medium to higher intrinsic firing rates (again due to the state of their intracellular clock) are slowed down to agree on a firing rate of 3 Hz. (**C**) Histogram of the firing rates for the 2,500 neurons with the slowest intrinsic firing rate (E_{Ca} $\leq$60.66 mV). (**D**) Histogram of the firing rates for the 2,500 neurons with the fastest intrinsic firing rate (E_{Ca} $\geq$61.35 mV). (**E**) Interspike interval (ISI) histogram for an individual neuron with an average firing rate of 0.5 Hz. The ISI distribution is skewed to the right, matching experimental data from irregularly firing SCN neurons *Kononenko and Dudek* (2004). (**F**) ISI histogram for an individual neuron with an average firing rate of 3 Hz. The ISI distribution is approximately normal, matching experimental data from regularly firing SCN neurons (*Kononenko and Dudek*, 2004).

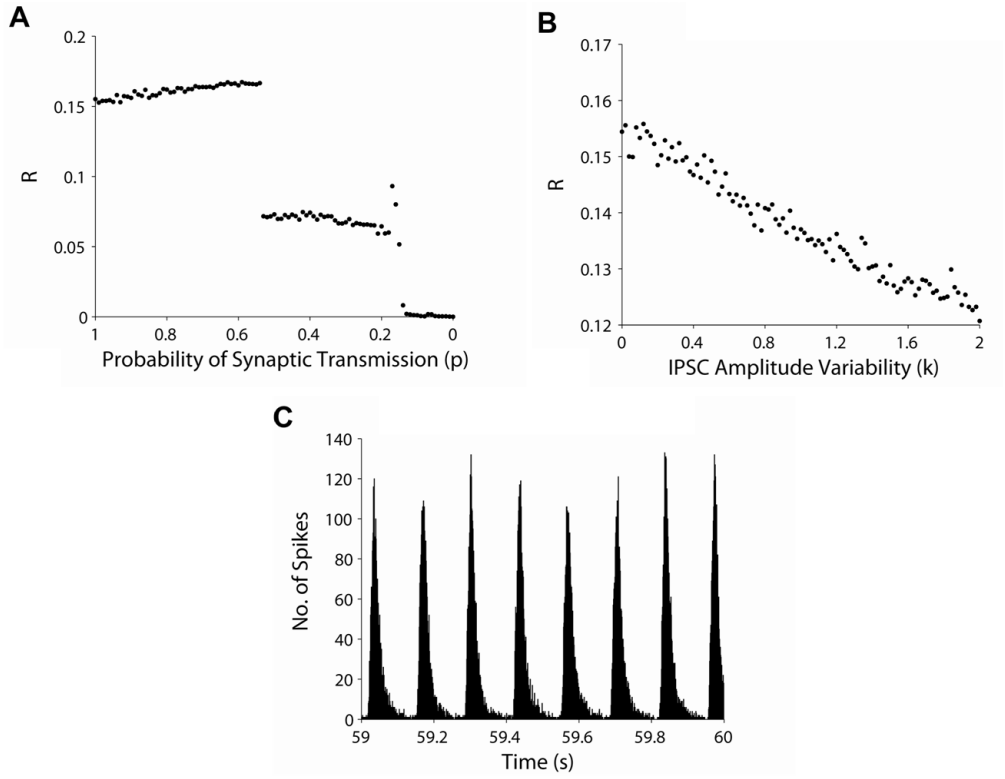

Figure 2.6: Clustering persists in the presence of synaptic noise. (**A**) The probability of a successful synaptic transmission is lowered from 100% reliable (p=1) to no transmission (p=0). Clustering is unaffected in simulations with g_{syn}=0.1, 10% connectivity, and $\sigma_{E_{Ca}}$=0.5 up to approximately p=0.5. For p=0.2-0.5, the network switches to a more disordered state, although three smeared clusters are still present. For $p < 0.2$, no clustering is detected. (B) Variability in the amplitude of IPSCs is increased from no variability (k=0) to the maximum variability possible while still ensuring all PSCs are inhibitory (k=2) with g_{syn}=0.1 (see Material and Methods for details). Clustering persists throughout this range (simulations are with 10% connectivity, $\sigma_{E_{Ca}}$=0.5, and p=1). (**C**) Simulation with both types of synaptic noise (g_{syn}=0.1, 10% connectivity, $\sigma_{E_{Ca}}$=0.5, p=0.5, and k=1). The instantaneous firing rate of the population, calculated as the number of action potentials per millisecond, indicates clustering persists despite this noise.

2.4 Discussion

Based on simulations of the SCN as an inhibitory network, we predict that the SCN forms clusters where neurons fire in near synchrony. Furthermore, we predict that the membership of these clusters may change over time. While these are novel predictions with respect to the SCN, clustering has been reported before in a number of other models of inhibitorily coupled oscillators. Several studies report clustering in globally coupled phase-only oscillators, e.g. *Golomb et al.* (1992) and *Okuda* (1993). *Golomb and Rinzel* (1994) observe clustering in a model of globally coupled reticular thalamic neurons, and note that adding noise to the neuronal dynamics can cause neurons to hop from cluster to cluster. *Golomb and Hansel* (2000) observe smeared clusters in either heterogeneous or sparse networks of integrate-and-fire neurons. *Terman et al.* (2008) studies dynamic clustering in sparsely connected excitatory-inhibitory networks. In our study we have tried to include many features of the physiology and complexity of the SCN by studying a predominantly inhibitory network with heterogeneity, sparse connectivity, and synaptic noise. Future work could include modeling electrotonic coupling and synaptic delays. To our knowledge this study is the first to suggest clustering in the SCN.

While clustering has appeared in many other neuronal models, there are relatively few studies that report having found clustering in experimental recordings. One example is *Terman et al.* (2008), which hints that dynamic clustering may be present in recordings from neurons within the insect antennal lobe. Without reporting clustering explicitly, there are several other experimental studies that indicate the importance of inhibition in synchronizing neurons in the hippocampus, thalamus, and the locust olfactory system (see discussion in *Tiesinga and Jose* (2000)). In *Traub et al.* (1996), $GABA_A$ receptor-mediated inhibition was shown to be the mechanism behind synchronization in hippocampal slices. *Tiesinga and Jose* (2000) distinguish weak synchronization, where the average neuronal activity of the population is peri-

odic without each neuron firing in each period, from strong synchronization, where each neuron fires within a short interval of each other, and claim that weak synchronization is consistent with the experimental recordings in *Traub et al.* (1996). While such synchronization has not yet been reported in experimental studies of the SCN, we predict that such synchronization may indeed be occurring in the SCN since $GABA_A$ receptor-mediated inhibition leads to clustering (a form of weak synchronization) in our model. Our model also predicts that such clustering will only occur if there is sufficient coupling strength and connectivity to overcome heterogeneity of circadian phase in the network. These conditions may not be met in cultures of dissociated SCN neurons or SCN slices, or admittedly even *in vivo*. If this is the case, then we would not expect clustering to occur in the SCN. However, if clustering is found in the SCN, the SCN would be a viable experimental system to study properties of clustering.

If clustering does occur in the SCN, what might its role be in terms of rhythm generation? One possibility is that many neurons firing in near synchrony could potentially send a stronger signal to other brain areas than individual neurons firing out of neuronal phase with each other. Additionally, if the firing rate of individual SCN neurons communicates time of day information, then the formation of clusters tends to either silence or adjust the firing rate of neurons whose intracellular clocks are out of circadian phase with the population average. Also, in our simulations, we have found that for the same parameters, different 3-cluster solutions are possible depending on initial conditions. *Chandrasekaran et al.* (2009) points out that such behavior allows a single network of neurons to be able to transmit multiple pieces of information in the form of temporal codes. This ability could be extremely useful for the SCN, given that it is a relatively small brain structure but needs to time many diverse rhythms throughout the body. We have focused on GABAergic neural coupling in this chapter since GABA is by far the most prevalent intrinsic neurotransmitter

in the SCN. However, we do note that there have been reports of neuronal synchronization in the SCN in the absence of synaptic transmission (*Bouskila and Dudek*, 1993).

Using our modeling framework, many more details of SCN anatomy and physiology could be incorporated. For example, the SCN is commonly believed to have distinct subdivisions, a ventral "core" and a dorsal "shell", with characteristic neuropeptide expression and projections (*Moore and Silver*, 1998). In our model, we could simulate this by giving a subset of neurons in the network certain properties, e.g. by making them VIPergic or possessing the VIP receptor VPAC2, and then control which other subsets of neurons they are connected to in accordance with the known densities of projections. We also plan to integrate this model with existing detailed models of the intracellular clock to help understand the link between the molecular biology and electrophysiology of circadian timekeeping.

CHAPTER III

Daily electrical silencing in the mammalian circadian clock

3.1 Introduction

SCN neurons are thought to encode the time of day by changing their firing frequency, with high rates during the day and low rates at night (*Gillette et al.*, 1995; *Mrugala et al.*, 2000; *Cutler et al.*, 2003). According to this view, during the day SCN neurons would be expected to fire repetitively, while at night they would be expected to fire irregularly or be quiescent at a hyperpolarized membrane potential. One of the predictions of the model in *Sim and Forger* (2007) was the existence of an additional quiescent state at a depolarized membrane potential. While similar depolarized steady-states exist in other neuronal models, e.g. Morris-Lecar (*Rinzel and Ermentrout*, 1998), the conventional wisdom is that mammalian neurons cannot survive and function at such depolarized states. However, the existence of a depolarized quiescent state in SCN neurons was recently confirmed experimentally by patch-clamp recordings performed by Mino Belle, in the laboratory of Hugh Piggins at the University of Manchester.

Belle et al. (2009) was able to distinguish two classes of SCN neurons, those that expressed a key clock gene *period1* ("*per1* neurons") and those that did not ("non-

per1 neurons"), by recording from mice that expressed an enhanced green fluorescent protein (EGFP) reporter of *per1*. Prior to recording, the mice were housed in a 12:12 hour light:dark schedule, where Zeitgeber Time (ZT) 0 corresponds to lights-on and ZT12 corresponds to lights off. Whole-cell recordings from *per1* and non-*per1* neurons in SCN brain slices were made across the projected day-night cycle, and showed a marked difference in the electrophysiological behavior of these two populations during the day. Non-*per1* neurons had a higher firing rate throughout the day than at night (Fig. 3.1B1-F1), as would be expected of SCN neurons. On the other hand, *per1* neurons did not follow this characteristic pattern and instead during the day sustained an electrically excited state and did not fire action potentials– a depolarized quiescent state as predicted by the Sim-Forger model (Fig. 3.1D GB).

In addition to the depolarized quiescent state, *per1* neurons also exhibited other complex electrical behaviors that were dependent on the time of day. In the late morning, *per1* neurons rapidly transitioned between quiescence and oscillations in membrane potential, indicating bistability of these two states (Fig. 3.1C). In the afternoon, some *per1* neurons exhibited depolarized low amplitude membrane oscillations (DLAMOs) (Fig. 3.1D GA). At night, *per1* neurons had a much more hyperpolarized resting membrane potential (RMP), and behaved more similarly to non-*per1* neurons, than during the day (Fig. 3.1E-G).

These data suggest that SCN neurons do not encode circadian phase solely through changes in firing frequency, but also by traversing from firing to a range of non-firing depolarized states. Understanding this circadian variation in electrical activity is critical to understanding the circadian timekeeping system as a whole. In mammals, neuronal membrane events have been shown to play a major role both in synchronizing the circadian clock to the external environment, and in the output pathway through which the clock's rhythmic signals modulate physiological processes and behavior (*Lundkvist and Block*, 2005). While the generation of the rhythmic signals themselves

is typically believed to be due to molecular feedback loops involving clock genes and their protein products, several studies suggest that neuronal membrane activity may also play a crucial role in the generation of rhythms (*Lundkvist and Block*, 2005; *Nitabach et al.*, 2005). Indeed, in the fruit fly *Drosophila*, electrical silencing stops rhythms in clock gene expression (*Nitabach et al.*, 2002).

In this chapter, we use mathematical modeling to demonstrate that the complex electrical behaviors observed in *per1* neurons (Fig. 3.1B-G) can be explained by existing data on ionic currents measured within SCN neurons.

3.2 Methods

3.2.1 Model of *per1* neurons

We adapted our model of unidentified SCN neurons from Chapter 2 to account for the enhanced electrical excitability of *per1* neurons by increasing the reversal potential for the leak current, E_L (see Appendix A). Also, while the model from Chapter 2 exhibited bistability between firing and quiescent states, the model APs had a higher amplitude than the membrane potential oscillations observed in Fig. 3.1C. With a small change in the fit of the Na^+ current, which still matched the experimentally measured Na^+ currents fit in the original Sim-Forger model (see Fig. 3.2), the model could more accurately reproduce the behavior of Fig. 3.1C. Noise in the applied current (I_{app}) was generated as in Chapter 2 and was rectified to be positive or negative for ESPCs or IPSCs, respectively (see Appendix A). Initial conditions for all simulations were V=-45, m=0.34, h=0.045, n=0.54, r=0.01, and f=0.04 unless indicated otherwise. All simulations shown used *ode15s*, a stiff variable order solver in MATLAB® (R2007a, Natick, MA, USA).

3.2.2 Circadian variation of cellular properties

Day-night differences in certain cellular properties within SCN neurons have been reported by several studies. *Pennartz et al.* (2002) demonstrated that the magnitude of L-type Ca^{2+} current in SCN neurons is significantly higher during the day than at night, while *Pitts et al.* (2006) found that BK-type K^+ current is greater at night than during the day. We modeled the diurnal variations in these currents as changes in g_{Ca} and g_K, respectively.

Ikeda et al. (2003) showed there is also a circadian rhythm in intracellular calcium concentration, $[Ca^{2+}]_i$, within SCN neurons. In Chapter 2, we mentioned that changes in $[Ca^{2+}]_i$ can be related to one of our model parameters, the reversal potential for calcium current (E_{Ca}), through the Nernst equation. However, because there is a several order of magnitude difference in $[Ca^{2+}]_i$ and the extracellular calcium concentration ($[Ca^{2+}]_o$) in mammalian neurons, K^+ ions actually make a significant contribution to the reversal potential of calcium channels (*Hille*, 2001). Therefore, the relationship between $[Ca^{2+}]_i$ and E_{Ca} is more accurately described by the Goldman-Hodgkin-Katz (GHK) voltage equation. The GHK voltage equation for a calcium channel with slight permeability to potassium ions is (*Somjen*, 2004):

$$E_{Ca} = \frac{RT}{F} ln \left(\frac{P_K[K]_o + (P_{Ca}/2)[Ca^{2+}]_o}{P_K[K]_i + (P_{Ca}/2)[Ca^{2+}]_i} \right) \tag{3.1}$$

with $R = 8.315$ J/(°K mol), $T = 295$°K, $F = 96,480$ coloumbs/mol, $[Ca^{2+}]_o$=2.4 mM, $[K]_o$=3 mM, $[K]_i$=143.5 mM, and a permeability ratio of P_{Ca}/P_K of 1000:1.

Using the Nernst equation, the 25% change in $[Ca^{2+}]_i$ reported by *Ikeda et al.* (2003) corresponds to a 10% change in E_{Ca} (*Sim and Forger*, 2007). However, based on the GHK equation the effect of the rhythm in $[Ca^{2+}]_i$ on E_{Ca} is much smaller ($< 1\%$). In this chapter, when we simulate the circadian variation in $[Ca^{2+}]_i$ we use Equation 3.1 to calculate E_{Ca}.

3.2.3 Bifurcation analysis

Our model represents a *per1* neuron as a *dynamical system*, with a set of variables describing the state of the neuron and a set of differential equations governing the time evolution of the state variables. Useful insights into the behavior of a dynamical system can be gained through bifurcation analysis. Bifurcations are sudden, qualitative changes in the behavior of a dynamical system that arise from small, smooth changes in system parameters (*Izhikevich*, 2007). Bifurcation diagrams depict the stability of the steady-state and periodic solutions of a dynamical system as a function of its parameters. A classic example is the bifurcation diagram showing the how the membrane potential V varies as a function of the applied current I in the Morris-Lecar model (*Rinzel and Ermentrout*, 1998). As I is increased, the solution changes from a steady-state to an oscillatory state and then back to a steady-state. These solutions correspond to a hyperpolarized quiescent state, repetitive spiking, and a depolarized quiescent state, respectively.

Due to known circadian variations in calcium and potassium currents within SCN neurons (*Pennartz et al.*, 2002; *Pitts et al.*, 2006), the bifurcation parameter of interest for our *per1* neuron model is not applied current, but the conductances g_{Ca} and g_K. To perform bifurcation analysis on the *per1* neuron model, we used the Oscill8 Dynamical Systems Toolset (*Conrad*, 2006).

3.3 Results

We considered the effect of variation in calcium and potassium currents on the behavior of our *per1* neuron model using simulation and bifurcation analysis. We found that as calcium conductance (g_{Ca}) was increased, the model behavior transitioned from a hyperpolarized quiescent state to repetitive spiking, and then ultimately to a depolarized quiescent state (Fig. 3.3). Conversely, as potassium conductance (g_K)

was increased, the model behavior transitioned from a depolarized quiescent state to repetitive spiking, and then ultimately to a hyperpolarized quiescent state (Fig. 3.4).

We then incorporated into the model circadian variations in g_{Ca} and g_K based on experimentally observed circadian rhythms in calcium and potassium currents in SCN neurons. We modeled g_{Ca} as being higher during the day than at night, in accordance with the rhythm in L-type Ca^{2+} current reported in *Pennartz et al.* (2002), and modeled g_K as being lower during the day than at night, in accordance with the rhythm in BK-type K^+ current reported in *Pitts et al.* (2006). The conductance values chosen to simulate *per1* neurons at various circadian phases are shown in Fig. 3.5. We find that simulations based on these rhythms in ionic conductances are able to reproduce the complex electrical behavior of *per1* neurons observed throughout a day-night cycle (compare Fig. 3.6 to Fig. 3.1B-G). Although a variation in only one ionic current could cause transitions from a hyperpolarized steady state to repetitive firing, and also from repetitive firing to a depolarized steady state, circadian rhythms in both K^+ and Ca^{2+} currents were required to faithfully reproduce the fine details of these transitions.

To study the bifurcations in model behavior as a function of the time of day, we fit sine functions with a period of 24 hours to the rhythms in g_{Ca} and g_K as shown in Fig. 3.5. We then used the phase of these sine functions, q, as a bifurcation parameter representing circadian phase in the bifurcation diagram shown in Fig. 3.7. Our bifurcation analysis revealed that as the day progresses, transitions in the behavior of *per1* neurons occur when a quiescent state gains or loses stability through Hopf bifurcations. This common mathematical structure has been found in many other neural systems and corresponds to Type II excitability (spiking emerging with nonzero frequency) in Hodgkin's original classification system (*Rinzel and Ermentrout*, 1998). The changes in stability of the hyperpolarized rest state we observed at night in *per1* neurons are similar in character to those seen in other neurons (*Paydarfar et al.*,

2006). However, *per1* neurons are different from other neurons in that a second Hopf bifurcation occurs during the day, where an unusually depolarized rest state becomes stable or unstable. The physiological importance of these bifurcations is that minor, molecular clock-driven changes in certain ionic conductances can have a major effect on the bioelectrical output of the neuron. Near bifurcation points, neurons can exhibit the type of behaviors seen in *per1* neurons, such as low-amplitude oscillations in membrane potential or noise-induced transitions between oscillatory and quiescent states (*Rinzel and Ermentrout*, 1998; *Izhikevich*, 2007).

The model behaviors do not depend on the initial state of the neuron and can be achieved with a variety of parameter choices. To illustrate this, we simulated the model with the same parameter settings as Fig. 3.6 but with a different initial membrane voltage, and found the same behaviors (Fig. 3.8). We also incorporated into our model a circadian variation in intracellular calcium concentration, $[Ca^{2+}]_i$, as measured in *Ikeda et al.* (2003). However, the effect of this rhythm in $[Ca^{2+}]_i$ (roughly 100 to 400 nM from trough to peak, Fig. 3.9B) on the model parameter E_{Ca} is minimal based on Equation 3.1. Figure 3.9C-H shows that when the $[Ca^{2+}]_i$ rhythm is taken into account, the same electrical behaviors are predicted as in previous simulations. The bifurcation diagram in Fig. 3.9A indicates that if the amplitude of the rhythm in $[Ca^{2+}]_i$ was in the micromolar rather than millimolar range, then its effect on the electrical behavior could be much stronger.

To demonstrate that the model results can be achieved with a variety of parameter settings, we repeated the simulations assuming a different extracellular calcium concentration, leading to a different setting for E_{Ca} based on Equation 3.1. Using a shifted rhythm in g_{Ca}, we produced the same electrical behaviors and a similar bifurcation diagram as the previous simulations (Fig. 3.10).

As a further verification of our model, we were able to reproduce the firing patterns characteristic of *per1* neurons receiving depolarizing or hyperpolarizing current pulses.

A depolarizing current pulse can drive a *per1* neuron that is firing APs into a DLAMO-like state, or into a depolarized quiescent state. A hyperpolarizing current pulse applied to a *per1* neuron that is either firing APs or in the depolarized quiescent state leads to a high-amplitude rebound spike. Figure 3.11 shows the experimental data, and Fig. 3.12 is the model reproduction of these signature behaviors.

3.4 Discussion

In this chapter, we have shown through mathematical modeling that known rhythms in ionic currents can account for the complex electrical behaviors observed in *per1* neurons. Importantly, not all SCN neurons exhibited these behaviors, but rather just those that appear to contain the intracellular molecular clock machinery. The notion that there are two distinct populations of SCN neurons has been put forth previously by other researchers. *Antle et al.* (2003) proposed that the SCN is composed of a population of nonrhythmic "gate" cells, which serve to synchronize a population of rhythmic "oscillator" cells. Our results suggest the possibility that in terms of electrical activity, *per1* neurons play the role of gate cells and their depolarized quiescent state is the signal which synchronizes the firing rate rhythm of the non-*per1* oscillator cells. This suggestion draws a parallel between the mammalian and fly circadian systems. In *Drosophila*, electrical silencing of clock neurons of a certain type (pigment dispersing factor (PDF) neurons), resets the phase of clock neurons of another type (non-PDF neurons) (*Wu et al.*, 2008).

The *Antle et al.* (2003) gates and oscillators model was based in part on the finding of *Jobst and Allen* (2002) that cells in a particular subregion of the SCN do not express a circadian rhythm in their firing rate. However, *Belle et al.* (2009) recorded from both *per1* and non-*per1* cells throughout the mid-coronal plane of the SCN, suggesting that neither rhythmically nor nonrhythmically firing cells are localized to a particular subregion.

Quintero et al. (2003) reported a linear correlation between firing frequency and the level of EGFP fluorescence in *per1* neurons. The *Belle et al.* (2009) results suggest a more complicated relationship between *per1* expression and membrane events, as the EGFP rhythm peaks in the late day around the time that *Belle et al.* (2009) finds that *per1* neurons are not firing at all. However, studies from both groups show a day-night difference in resting membrane potential (RMP) in *per1* neurons (*Kuhlman and McMahon*, 2004; *Belle et al.*, 2009). Our mathematical modeling indicates an increase in K^+ conductance is responsible for this change in RMP. This prediction is supported by the findings of *Kuhlman and McMahon* (2004) and by data from the mollusk *Bulla gouldiana*, where a circadian variation in K^+ conductance contributes to a rhythm in the RMP of clock (basal retinal) neurons (*Lundkvist and Block*, 2005).

The Sim-Forger model prediction of a depolarized quiescent state in SCN neurons has been verified experimentally by patch-clamp recordings of *per1* neurons. The modeling of *per1* neurons in this chapter demonstrated how these clock-containing neurons transition through a series of complex electrical behaviors throughout the course of a day. In the next chapter, we will continue to explore these complex states through a refined model of *per1* neurons, and make predictions regarding the functional role of these states in several aspects of circadian timekeeping.

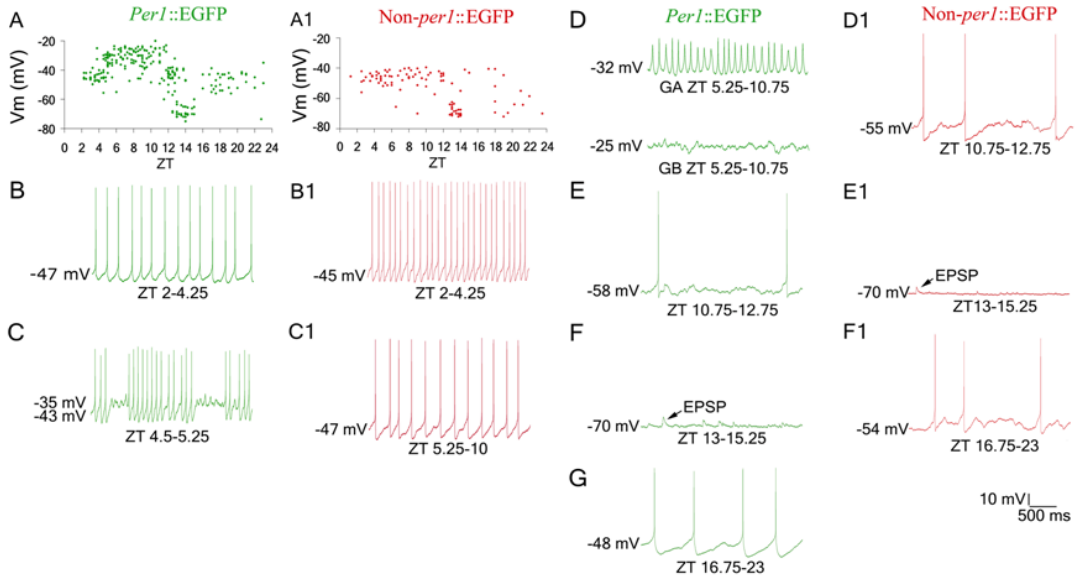

Figure 3.1: Electrical behavior of *per1* neurons (green) and non-*per1* neurons (red) throughout the day:night cycle. (**A** and **A1**) Scatter plot of resting membrane potential (RMP) versus Zeitgeber Time (ZT) for *per1* and non-*per1* cells. (**B** and **B1**) Morning *per1* and non-*per1* cells at moderate RMP firing action potentials (APs). (**C**) Late-morning *per1* cell in transitional phase displaying bistability of quiescence and membrane potential oscillations. (**D**) Afternoon to late-afternoon *per1* cell displaying depolarized low-amplitude oscillations (DLAMOs) [group A (gA)] or in a depolarized quiescent state [group B (GB)]. (**C1**) Non-*per1* neurons do not display bistability or depolarized RMP, but remain at moderate RMP, generating APs. (**E** and **D1**) Dusk *per1* and non-*per1* cells at moderate RMP around the time of lights-off. (**F** and **E1**) Early night *per1* and non-*per1* cells quiescent at hyperpolarized RMP, receiving excitatory postsynaptic potentials (EPSPs). (**G** and **F1**) Late-night *per1* and non-*per1* neurons at moderate RMP. *All experimental data shown was collected by Mino Belle.*

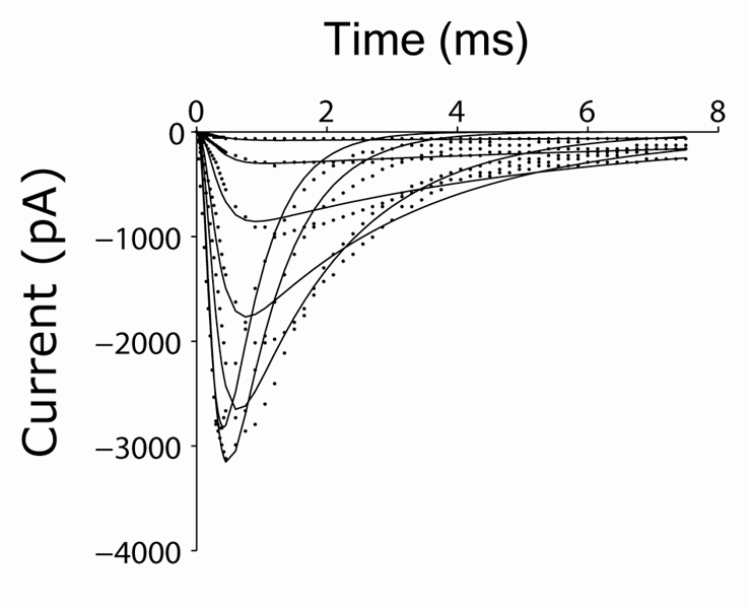

Figure 3.2: Na^+ current recorded in unidentified SCN neurons in response to voltage steps. Model predictions (curves) and experimental data (dots, *Jackson et al.* (2004)). These curves show that our choices of m_∞ and h_∞ match experimental data.

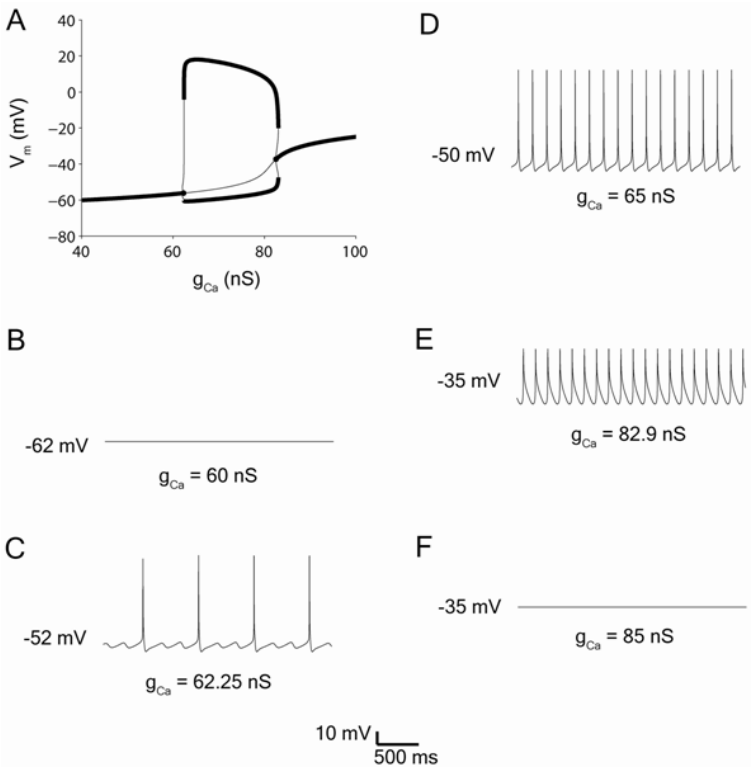

Figure 3.3: Modulating just the calcium conductance can cause transitions between the two rest states (B and F) and spiking (C and D). (**A**) Bifurcation diagram summarizing the behaviors seen as a function of g_{Ca}. (**B-F**) Voltage traces for various settings of g_{Ca}. For these simulations, we fixed $E_{Ca} = 54$ mV and $g_K = 16$ nS and did not include any randomly-generated post-synaptic currents.

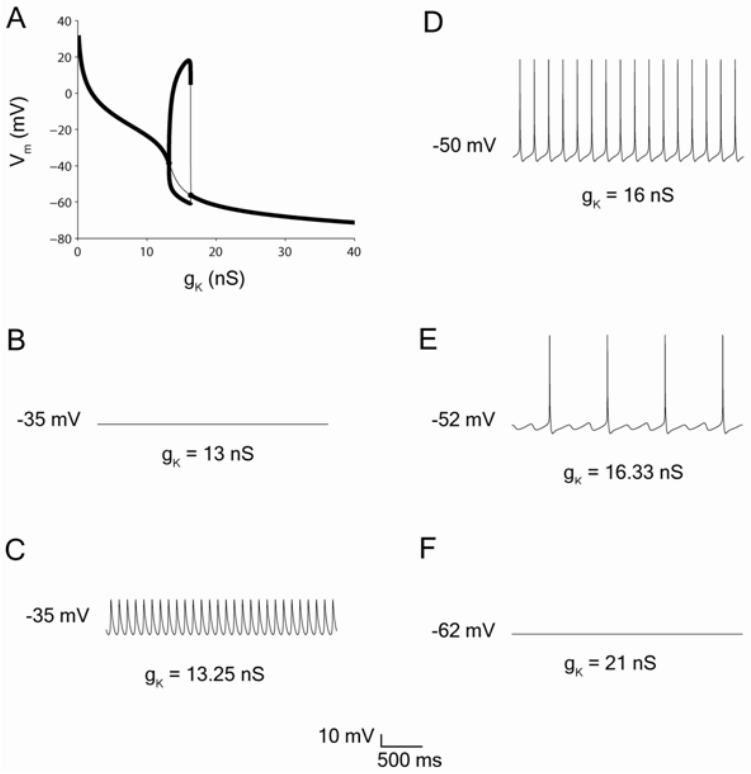

Figure 3.4: Modulating just the potassium conductance can cause transitions between the two rest states (B and F) and spiking (D and E). (**A**) Bifurcation diagram summarizing the behaviors seen as a function of g_K. (**B-F**) Voltage traces for various settings of g_K. For these simulations, we fixed $E_{Ca} = 54$ mV and $g_{Ca} = 65$ nS and did not include any randomly-generated postsynaptic currents.

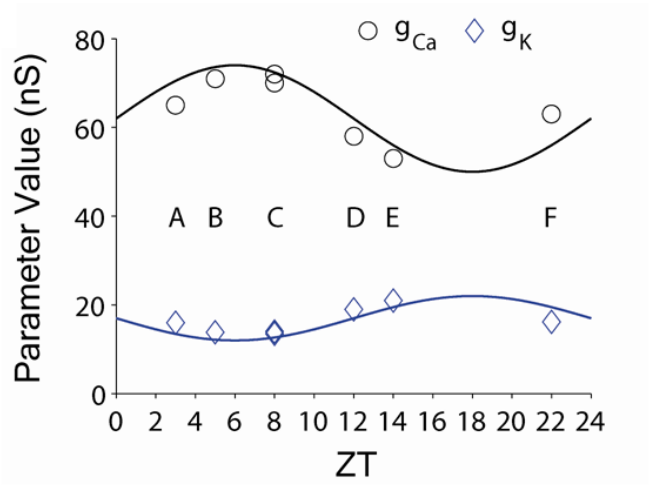

Figure 3.5: Circadian variation of parameters used to simulate a light:dark cycle. Circadian phase is represented by known rhythms in Ca^{2+} and K^{+} ionic conductances. Changes in g_{Ca} and g_K were based on *Pennartz et al.* (2002) and *Pitts et al.* (2006) respectively. The points shown for g_{Ca} and g_K were used to simulate panels A through F in Fig. 3.6. The lines shown are the functions $g_{Ca} = 62 + sin(2\pi q/24)$ and $g_K = 17 - 5sin(2\pi q/24)$, for q from 0 to 24.

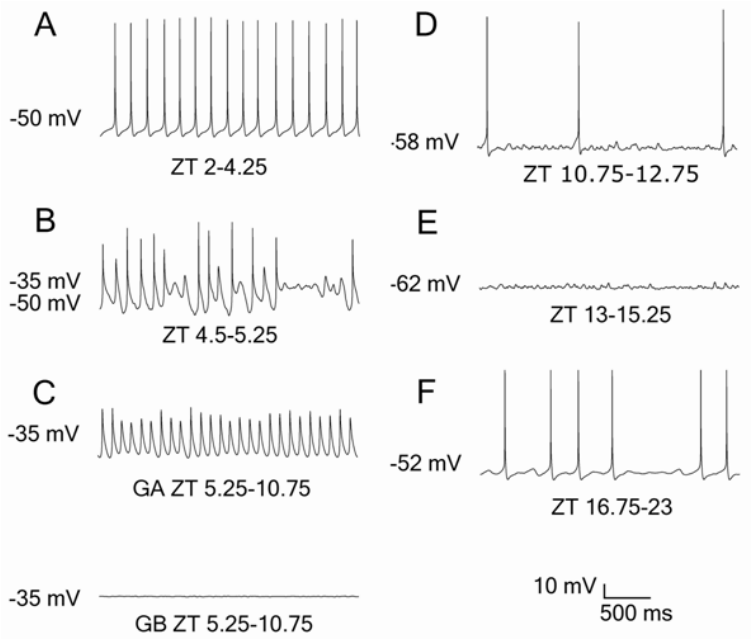

Figure 3.6: Simulations predicting the electrophysiological behavior of SCN clock neurons observed throughout a day-night cycle. These simulations use a revised version of the Sim-Forger model (*Sim and Forger*, 2007) specific for *per1* neurons and incorporate randomly generated post-synaptic potentials. (**A** to **F**) Panels are similar to experimental data in Fig. 3.1B-G, and show that known rhythms in ionic currents (Fig. 3.5) can explain the experimentally observed behaviors.

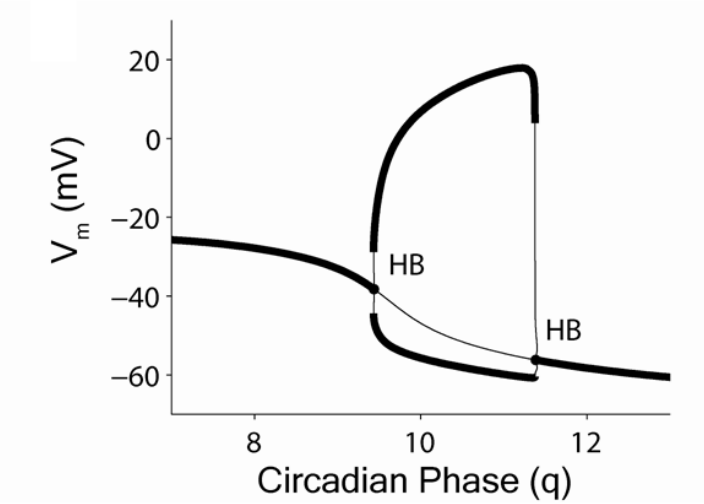

Figure 3.7: Bifurcation diagram summarizing the behaviors seen through a circadian cycle (thick lines indicate stability of the steady-state solution). The phase (q) of the two sine functions shown in Fig. 3.5, $g_{Ca} = 62 + sin(2\pi q/24)$ and $g_K = 17 - 5sin(2\pi q/24)$, was used as a bifurcation parameter representing circadian phase. Oscillations emerge through Hopf bifurcations (HB) when a quiescent state gains or loses stability.

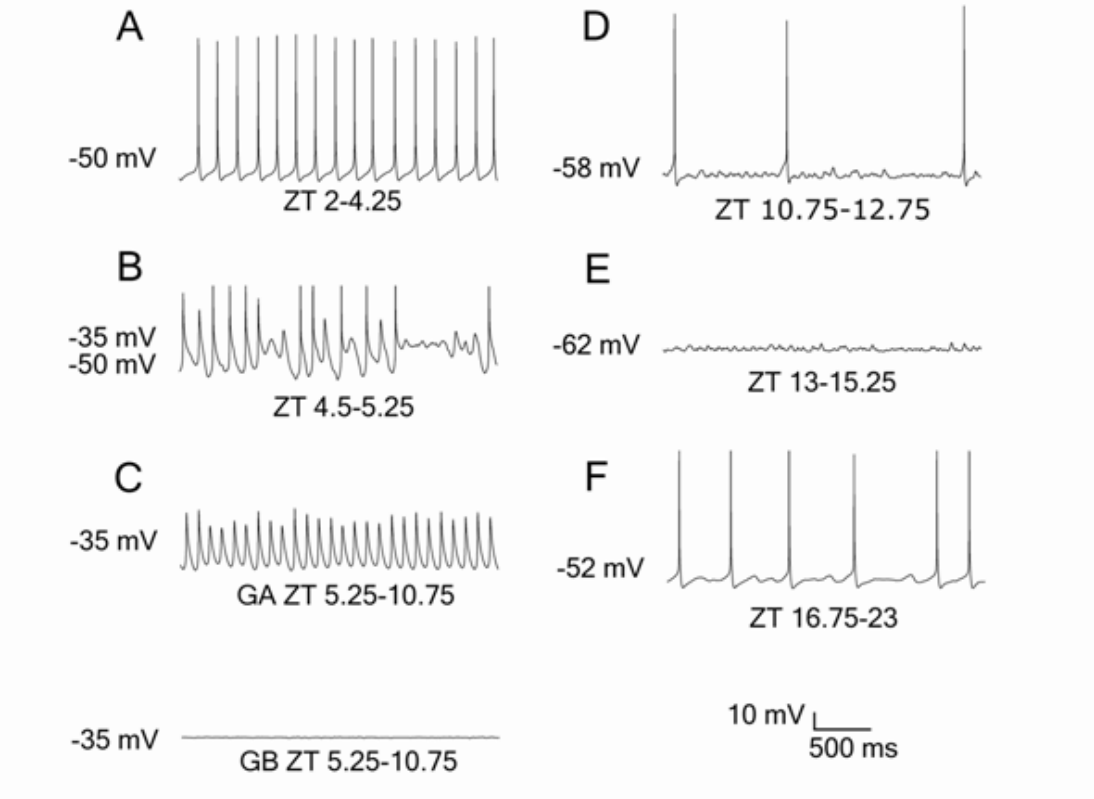

Figure 3.8: Robustness of model predictions to choice of initial membrane voltage. In Fig. 3.6, an initial voltage of V=-45 mV was used for simulation. Here, we show that the same behaviors were predicted when a more hyperpolarized initial voltage (V=-80 mV) was used. In both cases, the traces shown begin after 1 second of simulated time.

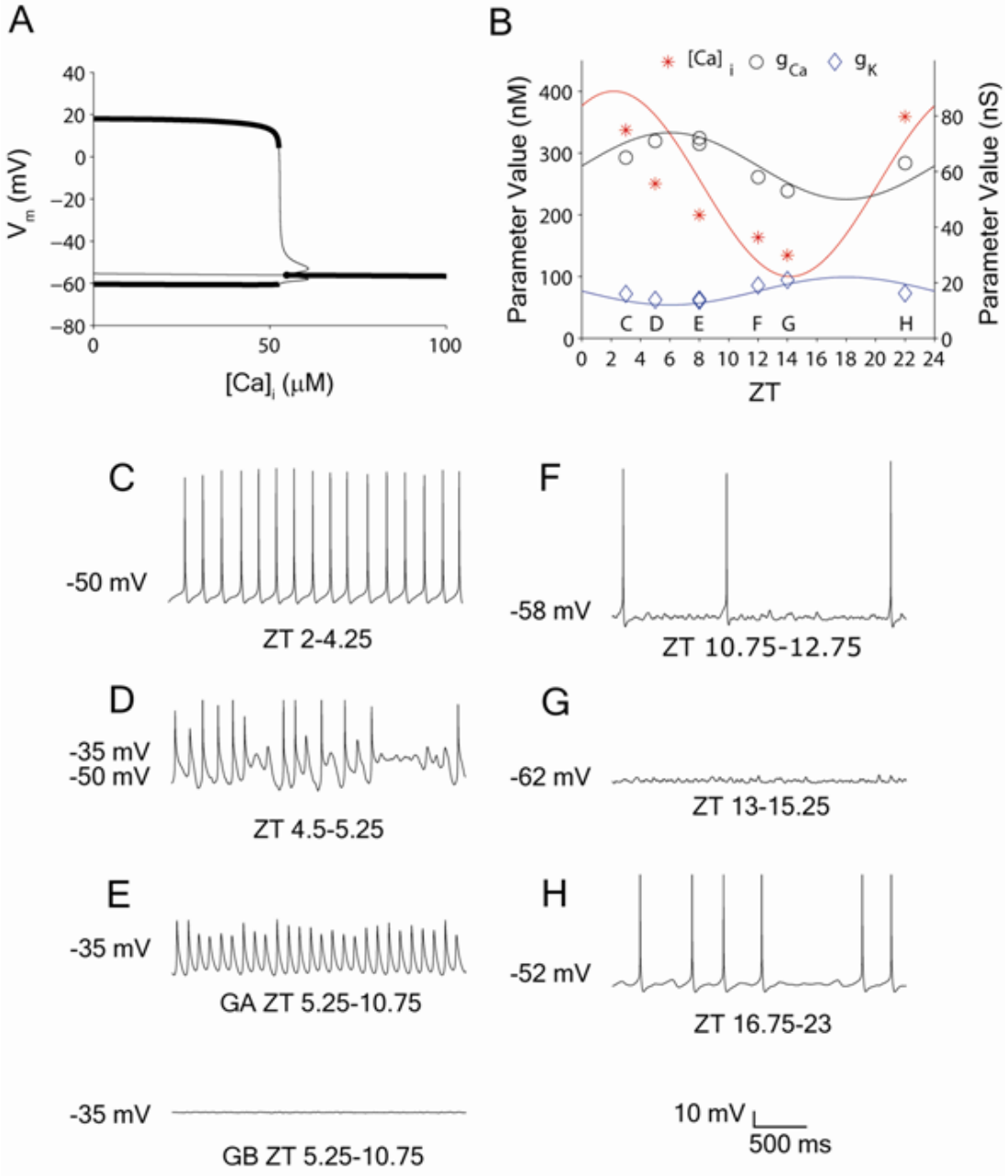

Figure 3.9: Simulations incorporating circadian variation in intracellular calcium concentration. (**A**) Bifurcation diagram summarizing the behaviors seen as a function of $[Ca^{2+}]_i$, using the GHK voltage equation to set E_{Ca}. (**B**) Circadian variation in $[Ca^{2+}]_i$, as measured in *Ikeda et al.* (2003). (**C-H**) Simulations incorporating circadian changes in $[Ca^{2+}]_i$, g_{Ca}, and g_K give the same model predictions as Figs. 3.6 and 3.8.

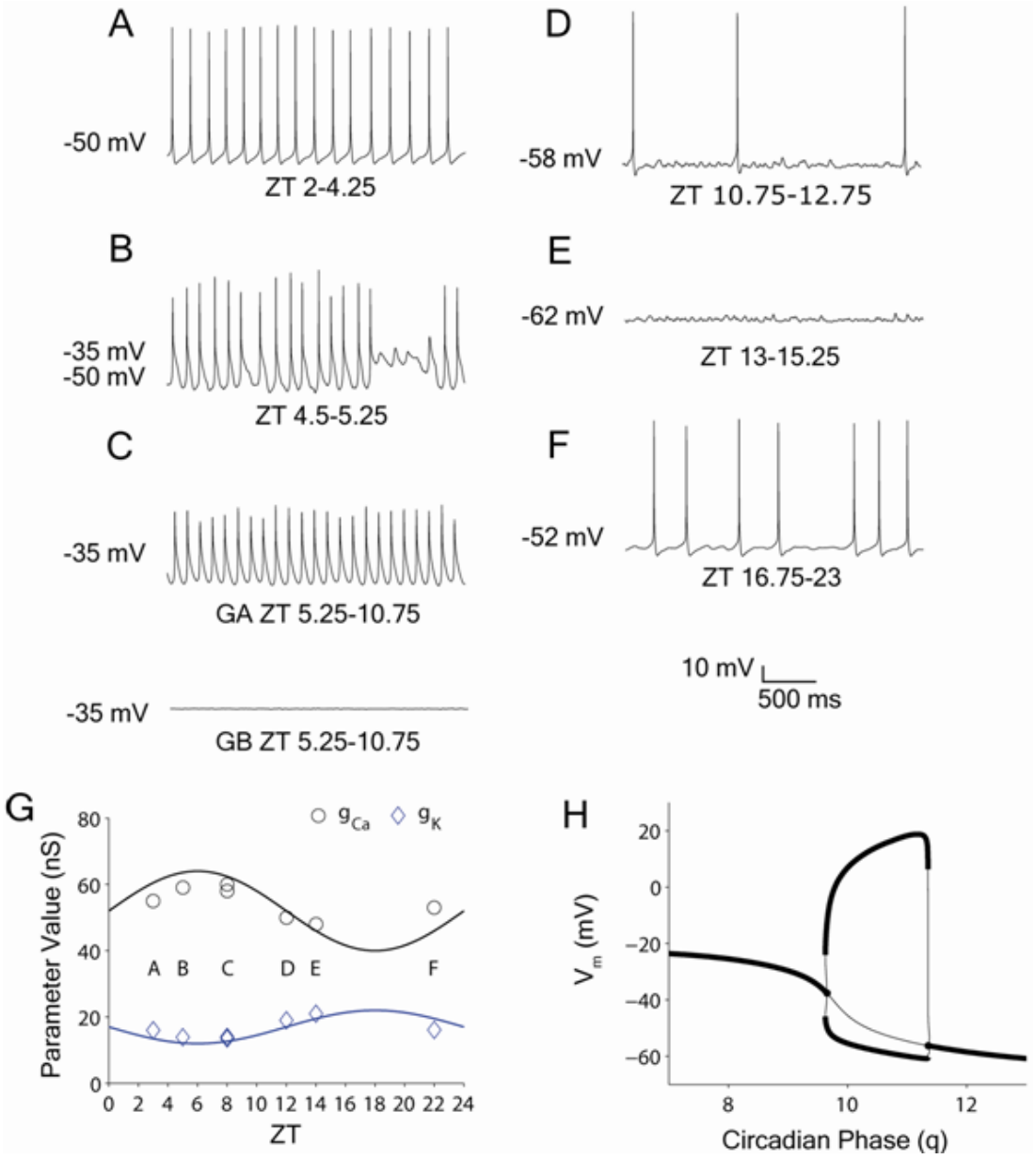

Figure 3.10: Robustness of model predictions to choice of extracellular calcium concentration. (**A-F**) In Figs. 3.6 and 3.8, the reversal potential of the calcium current (E_{Ca}) was set at 54 mV based on the GHK voltage equation with $[Ca^{2+}]_o$=2.4 mM. Here, we instead set E_{Ca} at 73 mV based on GHK with $[Ca^{2+}]_o$=5 mM. (**G**) We found that the same rhythm in K^+ conductance as in Figs. 3.6 and 3.8, combined with a shifted rhythm in Ca^{2+} conductance of $g_{Ca} = 52 + sin(2\pi q/24)$, produced the same electrical behaviors (**A-F**) and a similar bifurcation diagram (**H**) as the previous simulations.

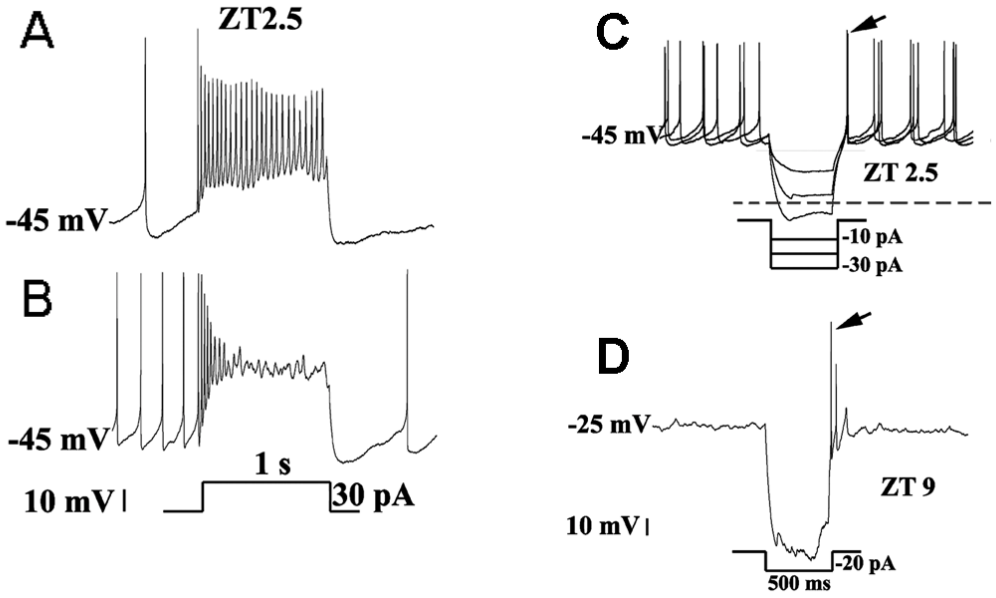

Figure 3.11: Firing patterns characteristic of *per1* cells. (**A-B**) Response to depolarizing pulses (1 s, 30 pA) in the morning. (**C**) Overlay of representative responses to hyperpolarizing pulses (500 ms, -10 to -30 pA) during early morning. (**D**) Response to hyperpolarizing pulse (500 ms, -20 pA) later in the day. Black arrows indicate a rebound spike, where the amplitude of the first AP is higher than other APs in the same trace. *All experimental data shown was collected by Mino Belle.*

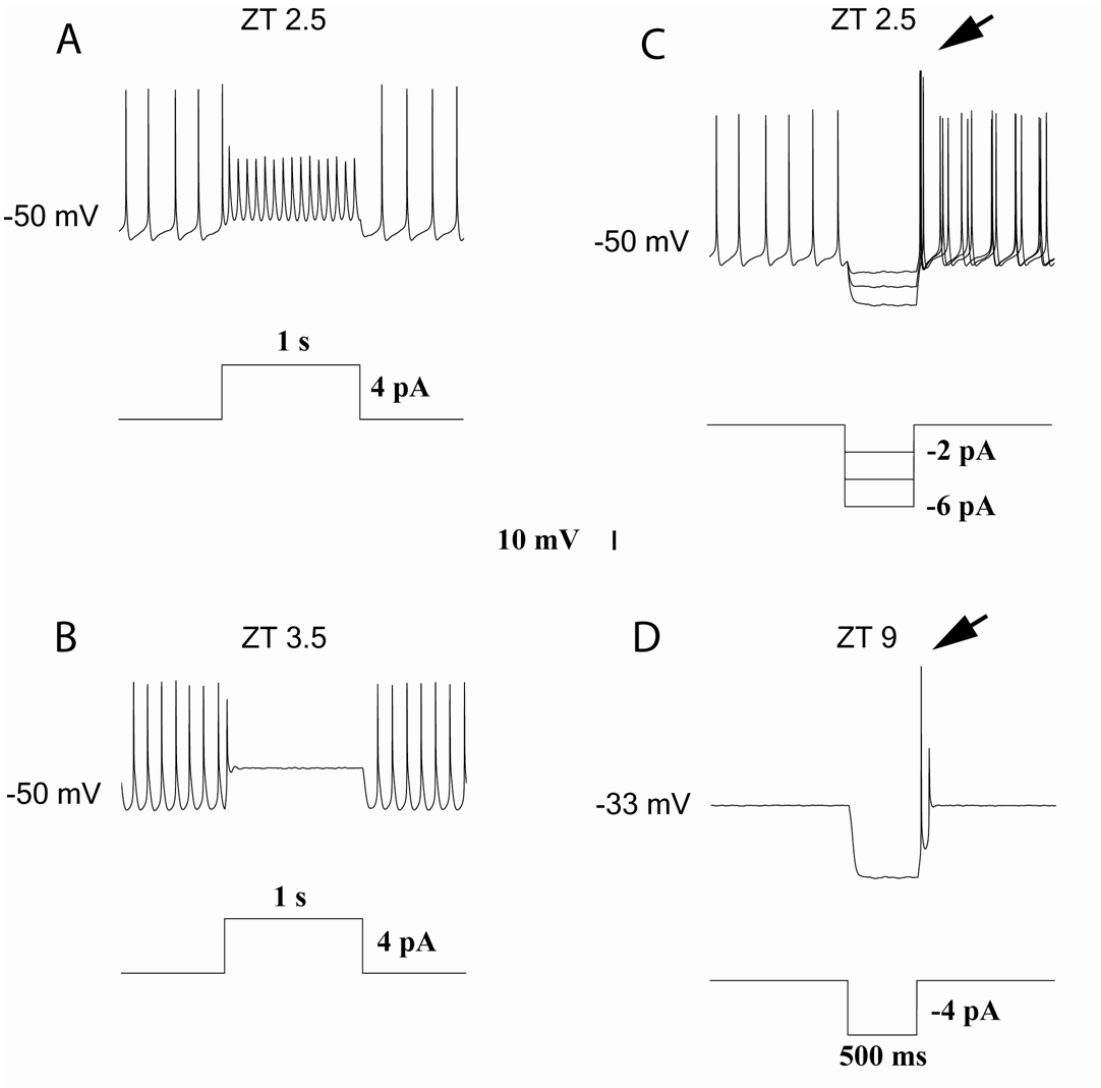

Figure 3.12: Simulations reproducing the firing patterns characteristic of *per1* neurons described in Fig. 3.11. (**A-B**) Model response to depolarizing pulses in the morning. (**C-D**) Model shows a high-amplitude rebound spike (black arrows) in response to a hyperpolarizing pulse. Parameter settings: (**A**) and (**C**) have the same parameters as Fig. 3.6A, (**D**) has the same as Fig. 3.6C, and (**B**) has the same as Fig. 3.6B but with g_K=15 nS.

CHAPTER IV

Refinement and predictions of a *per1* neuron model

4.1 Introduction

In this chapter, we refine our mathematical model of SCN electrophysiology based on experimental data presented in *Belle et al.* (2009). We also test our model by considering and incorporating aspects of other recently published models of SCN electrophysiology (*Kim and Jeong*, 2008; *Clay*, 2009; *Vasalou and Henson*, 2010; *Kononenko and Berezetskaya*, 2010).

In Chapter 3, we demonstrated through mathematical modeling that the depolarization of the membrane potential seen in *per1* neurons in the afternoon could be accounted for by a reduction in potassium conductance. This was confirmed by current-clamp recordings made in *Belle et al.* (2009) which showed that blocking calcium-activated potassium (K_{Ca}) channels could significantly depolarize *per1* neurons. In this chapter we extend our model to incorporate K_{Ca} currents and study their role in depolarized low amplitude membrane oscillations (DLAMOs) and the depolarized quiescent state.

Two of the recently published models involving SCN electrophysiology, *Kim and Jeong* (2008) and *Vasalou and Henson* (2010), do include a K_{Ca} current. *Vasalou and*

Henson (2010) developed a firing rate model for SCN neurons to study how firing correlates with circadian gene expression. The *Vasalou and Henson* (2010) model was focused on behavior at the 24-hour time scale rather than the millisecond time scale, and so did not consider the dynamics of individual ionic currents in detail. Therefore *Vasalou and Henson* (2010) does not provide a mathematical description of the K_{Ca} current in SCN neurons that we can incorporate directly into our model. *Kim and Jeong* (2008) presents a Hodgkin-Huxley-type model of SCN neurons, the same formalism used in *Sim and Forger* (2007) and Chapters 2 and 3. However, the K_{Ca} current in *Kim and Jeong* (2008) was not based on data from SCN neurons in particular, rather its form was taken from the neuronal model repository ModelDB (*Hines et al.*, 2004) and implemented without modification. In this chapter, we fit a model of K_{Ca} current specifically to experimental data from SCN neurons (*Jackson et al.*, 2004).

We then use our refined model to make predictions about several key processes involved in the regulation of circadian rhythms: the accumulation of intracellular calcium ions, intercellular communication within the SCN, and the ability of the clock to be phase-shifted by light (photic gating).

4.2 Methods

4.2.1 Model of K_{Ca} current in SCN neurons

The first mathematical model of the electrophysiology of SCN neurons was introduced in *Sim and Forger* (2007). This Hodgkin-Huxley-type model was fit to published data on ionic currents in SCN neurons and included an inward sodium current (I_{Na}), an inward calcium current (I_{Ca}), an outward potassium current (I_K), and a leak current (I_L). The Sim-Forger model was adapted to account for the enhanced electrical excitability of *per1* neurons in Chapter 3, and in this chapter we

will refine the model further by incorporating a K_{Ca} current. Since K_{Ca} currents are primarily calcium-dependent, we will also need to incorporate intracellular calcium dynamics into the model. Calcium dynamics are extremely complex and involve many different mechanisms, such as buffering, uptake into intracellular stores, and extrusion through membrane pumps. Another recent model of SCN neurons (*Vasalou and Henson*, 2010) does include several of these mechanisms. However, because many of the details of the action of these mechanisms in SCN neurons have not been measured experimentally, we will instead use a very simple model of calcium dynamics. Our model represents all of these calcium handling mechanisms with a single term for the removal of free calcium ions from the cytoplasm, as in *Booth et al.* (1997). In our model, calcium enters the cytoplasm through voltage-gated calcium channels only; we do not consider release from intracellular stores. Thus, the concentration of free intracellular calcium ions ($[Ca^{2+}]_i$) is determined by the equation:

$$\frac{dCa}{dt} = -kI_{Ca} - bCa \tag{4.1}$$

where Ca represents $[Ca^{2+}]_i$, k converts Ca^{2+} current (pA) to Ca^{2+} concentration (mM), and b is the Ca^{2+} removal rate. Following *Yamada et al.* (1998), we calculate k as $\frac{1}{zFV_s}$, where z=2 is the charge of a calcium ion, F=96,485 C/mol is Faraday's constant, and V_s is the volume of a thin spherical shell just below the membrane where the binding of intracellular calcium ions to K_{Ca} channels occurs. A shell depth of 0.1 μM is a common choice for models where $[Ca^{2+}]_i$ is relevant for K_{Ca} channel activation (*Yamada et al.*, 1998; *McCormick and Huguenard*, 1992). We set k=1.65$\times$ 10^{-4} mM/ms, which corresponds to a SCN cell radius around 5 μM (*Klein et al.*, 1991) and a shell depth of 0.1 μM. With k fixed, the only free parameter in Equation 4.1 is the removal rate b, which we set based on $[Ca^{2+}]_i$ measurements in SCN neurons from *Irwin and Allen* (2009). When *Irwin and Allen* (2009) applied a constant hyperpolarizing current to a SCN neuron to inhibit AP firing and hold the membrane

potential at around -60 to -70 mV, $[Ca^{2+}]_i$ maintained a steady state of around 50 nM. When we applied a constant hyperpolarizing current in our model to inhibit AP firing, we found that setting b=10 ms^{-1} resulted in a steady state value of Ca (50 nM) consistent with the *Irwin and Allen* (2009) data.

The K_{Ca} current in our model is activated by Ca. To determine the parameters for $I_{K_{Ca}}$ in our model, we relied heavily on K_{Ca} current measurements in SCN neurons obtained by *Jackson et al.* (2004) using action potential clamp. In this protocol, a spontaneous action potential is recorded and then played back to the cell as the command voltage. Figure 12 of *Jackson et al.* (2004) shows the total calcium current and the total K_{Ca} current evoked during an action potential. Initially, the inward calcium current outweighs the outward K_{Ca} current, but during the AP this relationship reverses and the net current becomes outward. We simulated this type of action potential clamp experiment in our model, and with the aid of the *fminsearch* routine in MATLAB® chose parameters for $I_{K_{Ca}}$ that could reproduce this relationship. Figure 4.1 shows that during a simulated AP, I_{Ca} is initially greater than $I_{K_{Ca}}$, but quickly $I_{K_{Ca}}$ becomes greater and the net current ($I_{Ca} + I_{K_{Ca}}$) becomes outward, as in the *Jackson et al.* (2004) data. The deflection in the voltage trajectory, or "hump", visible during the falling phase of the model AP in Fig. 4.1A is not seen in the experimental data. For simplicity, we have modeled the K_{Ca} current as calcium-dependent and voltage-independent, whereas K_{Ca} currents in SCN neurons likely have both calcium-dependent and voltage-dependent components (*Teshima et al.*, 2003; *Cloues and Sather*, 2003). The lack of voltage-dependence in our model of K_{Ca} current may contribute to the imperfection in the shape of the model APs.

The model equations follow *Yamada et al.* (1998):

$$I_{K_{Ca}} = g_{K_{Ca}} c^2 (V - E_K) \tag{4.2}$$

where V is the membrane potential, E_K is the equilibrium potential for K^+ ions, $g_{K_{Ca}}$

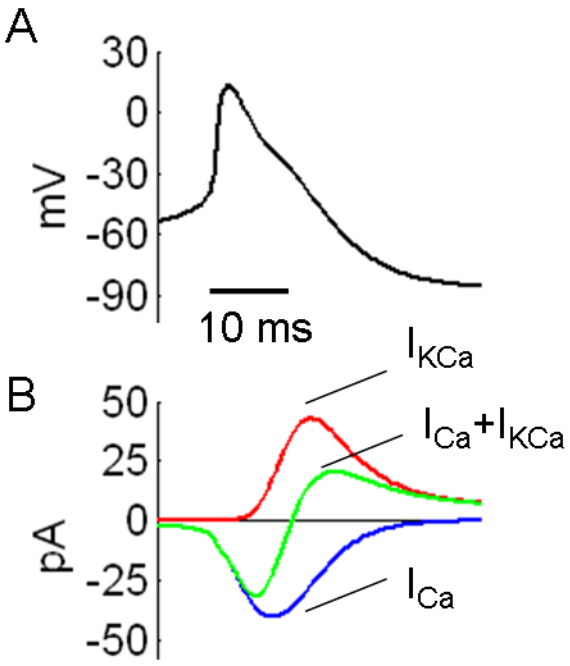

Figure 4.1: Simulated action potential clamp experiment used to fit $I_{K_{Ca}}$ parameters. (**A**) Membrane potential during a model *per1* neuron action potential. (**B**) I_{Ca} and $I_{K_{Ca}}$ during the action potential. The net current, $I_{Ca}+I_{K_{Ca}}$, is initially inward but then quickly reverses and becomes outward as in Figure 12 of *Jackson et al.* (2004).

is the maximal K_{Ca} conductance, and c is a calcium-dependent gating variable with the dynamics:

$$\frac{dc}{dt} = \frac{c_\infty - c}{\tau_c} \tag{4.3}$$

$$c_\infty = \frac{\alpha(Ca)}{\alpha(Ca) + \beta} \tag{4.4}$$

$$\tau_c = \frac{500}{\alpha(Ca) + \beta} \tag{4.5}$$

where c_∞ is the steady-state fraction of open K_{Ca} channels, τ_c is the time constant

for opening and closing of K_{Ca} channels, and $\alpha(Ca) = 10^7 Ca^2$ and $\beta = 5.6$ are the opening and closing rates, respectively.

Our full model for the electrophysiology of *per1* neurons is now as follows:

$$\frac{dV}{dt} = -\frac{1}{C}(I_{Na} + I_{Ca} + I_K + I_{K_{Ca}} + I_L + I_{syn}) \tag{4.6}$$

where C is the membrane capacitance, and I_{syn} are noisy synaptic currents as described in Sec. 4.2.2.

4.2.2 Noise mechanisms

The two primary sources of stochasticity in neuronal firing are randomness in the gating of ion channels ("channel noise"), and variability in synaptic processes ("synaptic noise") (*White et al.*, 2000). Synaptic noise arises from multiple sources, including the fundamentally probabilistic nature of neurotransmitter release and randomness in the firing patterns of presynaptic neurons. Here, we model synaptic noise by incorporating randomly generated post-synaptic currents, both inhibitory (IPSCs) and excitatory (EPSCs), through the I_{syn} term in our model. The IPSCs and EPSCs were generated independently with the same Poisson rate, and had exponential rise and decay as in Chapter 3.

Channel noise is incorporated into our simulations in Sec. 4.3.7 by including stochastic subthreshold voltage-dependent cation (SVC) channels as described in *Kononenko and Berezetskaya* (2010). *Kononenko and Berezetskaya* (2010) modeled a single SVC channel as having 2 closed states, slow-closed (b_{sc}) and fast-closed (b_{fc}), and one open state (b_o). The transitions between these 3 states are shown in Fig. 4.2. The transition rates are governed by the time constants τ_o=0.2 ms, τ_{fc}=1 ms, and the voltage-dependent slow-component:

$$\tau_{sc} = \frac{256}{exp(\frac{V+90}{5}) + exp(-\frac{V+90}{125})} + 4 \tag{4.7}$$

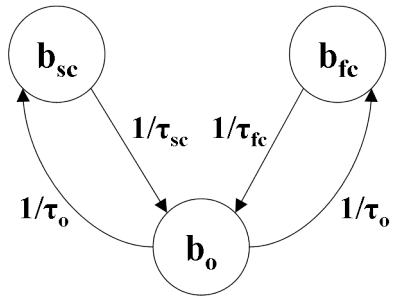

Figure 4.2: SVC single channel state transition diagram

A neuron is modeled as having N single SVC channels that open and close randomly and independently. The total SVC current, I_{SVC}, is given by:

$$I_{SVC} = N_o(t) g_{SVC}(V - E_{SVC}) \tag{4.8}$$

where g_{SVC}=0.04 nS is the single channel conductance, E_{SVC}=0 mV is the reversal potential, and $N_o(t)$ is number of open channels at time t. To determine $N_o(t)$ we follow the probabilistic procedure described in *Kononenko and Berezetskaya* (2010). To verify our implementation of this procedure, we repeated the simulations shown in Figure 1C of their paper, which confirmed that the voltage-dependence of the single-channel current in our simulations agrees qualitatively with their results (Fig. 4.3).

4.2.3 Numerical techniques

The simulations were performed using *ode15s*, a stiff variable order solver in MATLAB® (R2007a, Natick, MA, USA). Oscill8 Dynamical Systems Toolset (*Conrad*, 2006) was used for bifurcation analysis of the model.

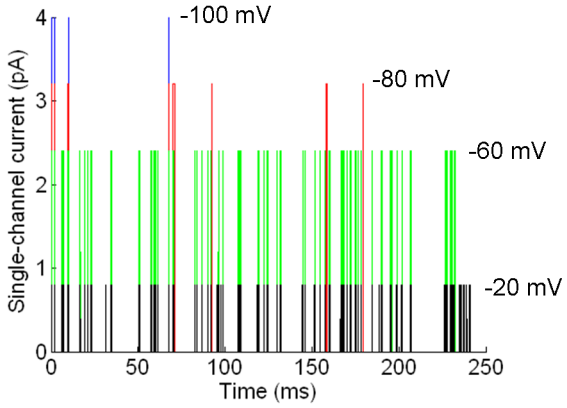

Figure 4.3: Simulations of I_{SVC} for a single channel (N=1) at different holding potentials to illustrate the voltage dependence of the channel open probability. Simulation results agree qualitatively with Figure 1C in *Kononenko and Berezetskaya* (2010).

4.3 Results

4.3.1 Membrane depolarization

In *Belle et al.* (2009), concomitant application of the K_{Ca} channel blockers iberiotoxin and apamin significantly and irreversibly depolarized *per1* neurons. When the blockers were applied in the early morning to *per1* neurons that were firing APs, upon depolarization they began to exhibit DLAMOs. When the blockers were applied to *per1* neurons in the late morning, upon depolarization they first exhibited DLAMOs and then entered the depolarized quiescent state. To simulate the effect of these blockers, we put the model in an AP producing state and then steadily reduced $g_{K_{Ca}}$. Figure 4.4 shows that as $g_{K_{Ca}}$ is reduced, the model behavior transitions from firing APs to DLAMOs and ultimately to the depolarized quiescent state.

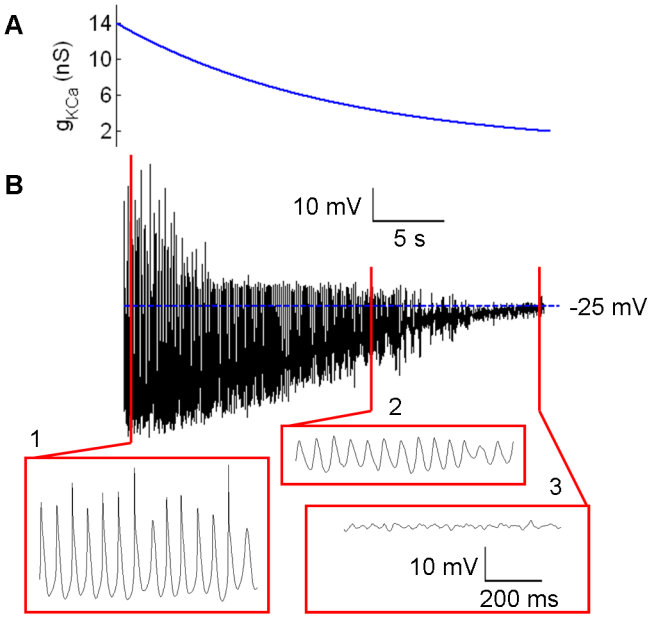

Figure 4.4: Simulated block of K_{Ca} current. (**A**) Exponential decay of $g_{K_{Ca}}$ used to simulate the effect of K_{Ca} blockers iberiotoxin and apamin. (**B**) Model *per1* neuron starts out producing APs (inset 1), but as $g_{K_{Ca}}$ is reduced model behavior transitions first to DLAMOs (inset 2) and then the depolarized quiescent state (inset 3). The scale bars shown in inset 3 apply to all insets.

4.3.2 Ionic currents underlying DLAMOs

To determine the ionic mechanisms responsible for producing DLAMOs, we bath-applied various channel blockers to a *per1* neuron producing spontaneous DLAMOs in the afternoon (Fig. 4.5A, *experimental data collected by Mino Belle*). DLAMOs persisted in the presence of the sodium channel blocker tetrodotoxin (TTX), with only minor effects on the shape of the oscillations observed. Application of the L-type calcium channel blocker nimodipine reversibly abolished DLAMOs. We then repeated these experiments with our model by simulating the effect of the channel blockers (Fig. 4.5B). We started with the model in the DLAMO state, with g_{Na}=229 nS and g_{Ca}=26 nS. We then simulated the application of TTX by setting g_{Na} to 0, and in agreement with the experimental data found that the DLAMOs were not

abolished. To simulate the effect of nimodipine, we reduced g_{Ca}. We did not set g_{Ca} to 0 because nimodipine specifically blocks L-type calcium current, while in our model g_{Ca} represents the total calcium current (not just L-type). We chose a value for g_{Ca} of 20 nS (a 23% reduction) to simulate nimodipine because *Jackson et al.* (2004) estimated that 20-40% of total voltage-gated calcium current in SCN neurons is through L-type channels. Again in agreement with the experimental recordings, we found that DLAMOs were abolished in simulated nimodipine. (The simulations in Fig. 4.5B included synaptic noise, see Fig. 4.13A for simulations without noise.)

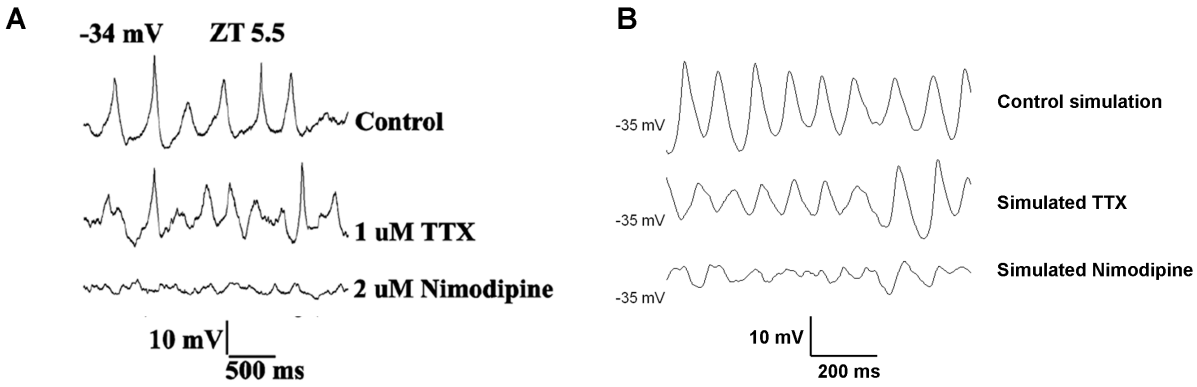

Figure 4.5: Role of L-type Ca^{2+} and TTX-sensitive Na^{+} channels in mediating DLAMOs. (**A**) Current-clamp recordings. Afternoon *per1* neuron displaying DLAMOs (*top trace*). Application of TTX (1 μM) does not abolish DLAMOs (*middle trace*). Application of nimodipine (2 μM) abolishes DLAMOs (*bottom trace*). *All experimental data shown was collected by Mino Belle.* (**B**) Model simulations. Model *per1* neuron (g_{Na}=229 nS, g_{Ca}=26 nS) displaying DLAMOs (*top trace*). Simulated application of TTX (g_{Na}=0) does not abolish DLAMOs (*middle trace*). Simulated application of nimodipine (g_{Ca}=20 nS) abolishes DLAMOs (*bottom trace*).

These results indicate that Ca^{2+} current is more important than Na^{+} current for producing spontaneous DLAMOs in SCN neurons. To explore the mechanisms behind these oscillations, we look at the time course of the currents that are active in the model during DLAMOs (Fig. 4.6). During the rising phase of the oscillation, both I_{Ca} and I_K are activated and oppose each other. Closer to the peak of the oscillation,

$I_{K_{Ca}}$ activates and contributes to the repolarization of the membrane in the falling phase. Thus, it appears that the interplay between inward Ca^{2+} current and outward K_{Ca} current is the key mechanism underlying the oscillations.

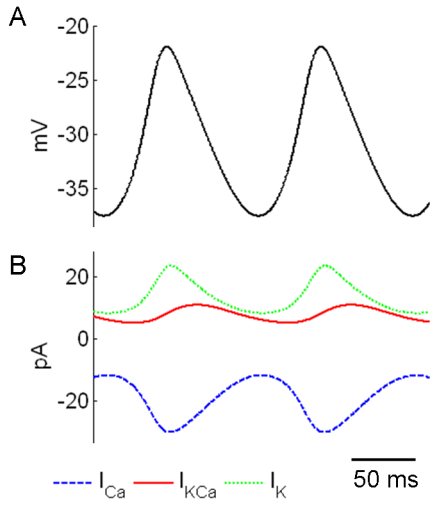

Figure 4.6: Ionic currents active during DLAMOs. (**A**) Membrane potential of a model *per1* neuron displaying DLAMOs. (**B**) I_{Ca}, $I_{K_{Ca}}$, and I_K during DLAMOs. The interplay between I_{Ca} and $I_{K_{Ca}}$ is critical in producing the oscillations.

In *Belle et al.* (2009), it was reported that application of nimodipine on *per1* cells in the morning caused a significant and reversible depolarization of the resting membrane potential (RMP). At first glance this result may seem counterintuitive, as one might expect that inhibiting an inward current like L-type calcium would cause a hyperpolarization. Nevertheless, our model reproduces this behavior as shown by the bifurcation diagram in Figure 4.7. When the model is in an oscillatory state, the RMP (depicted by the thin black line) increases as g_{Ca} is reduced. The model indicates that the depolarization is due to the effect inhibiting inward Ca^{2+} current has on the outward K_{Ca} current. For example, reducing g_{Ca} from 23 to 22 nS (which depolarizes the model RMP by 0.2%) causes a 4% decrease in I_{Ca} but a 13% decrease in $I_{K_{Ca}}$.

Analysis of the model also reveals that DLAMOs can be understood mathemati-

cally as a small amplitude limit cycle arising from a Hopf bifurcation. The bifurcation diagram in Figure 4.7 shows that if g_{Ca} is reduced far enough, the steady state solution of the dynamical system will transition from a limit cycle to a stable node (depicted by the thick black line), which corresponds to the depolarized quiescent state.

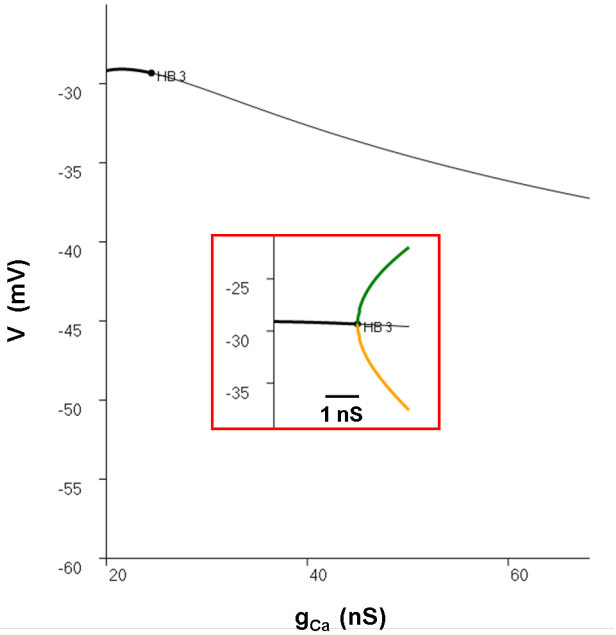

Figure 4.7: Bifurcation diagram illustrating that inhibiting I_{Ca} can depolarize the membrane. As g_{Ca} is reduced, the model steady state solution for the resting membrane potential (thin black line) increases. The system undergoes a Hopf bifurcation around g_{Ca}=24 nS (point labeled HB 3 in main panel and inset). To the left of the bifurcation point, there exists a stable node (thick black line in main panel and inset) corresponding to the depolarized quiescent state. To the right of the bifurcation point, there exists a stable limit cycle corresponding to DLAMOs. The amplitude of the oscillations are indicated by the green and yellow lines in the inset.

4.3.3 Ca^{2+} response

The calcium concentration inside a cell not only controls the activation of K_{Ca} currents, but also plays a critical role in many other cellular processes such as muscle contraction and synaptic plasticity (*Koch*, 1999). Due to the importance of Ca^{2+} as

a signal transduction element, $[Ca^{2+}]_i$ is tightly regulated, and an excess of calcium ions can lead to cell death (*Verkhratsky and Toescu*, 1998). Calcium ions have also been shown to induce *per1* expression (*Tischkau et al.*, 2003). Since the magnitude of Ca^{2+} influx through voltage-gated calcium channels follows a circadian rhythm in SCN neurons (*Pennartz et al.*, 2002), calcium is a potential link between membrane potential and the clock gene expression cycle. Indeed, a circadian rhythm in $[Ca^{2+}]_i$ in SCN neurons has been observed *Ikeda et al.* (2003). For these reasons, we are interested in using our model to predict the accumulation of $[Ca^{2+}]_i$ that occurs during DLAMOs.

First, we consider the $[Ca^{2+}]_i$ response in a thin shell just below the membrane where $[Ca^{2+}]_i$ is relevant for K_{Ca} channel activation. As discussed in Sec. 4.2.1, $[Ca^{2+}]_i$ in this shell is represented in our model by the variable Ca. We simulated the model in a state that produced spontaneous action potentials, and tracked the level of $[Ca^{2+}]_i$ (Fig. 4.8A). We then simulated the model in a state that produced spontaneous DLAMOs, and again tracked $[Ca^{2+}]_i$ (Fig. 4.8B). We find that during an AP, $[Ca^{2+}]_i$ reaches a higher level (670 nM) than it does during a DLAMO (500 nM). However, in between APs $[Ca^{2+}]_i$ decays to around 1 nM, while during the trough of a DLAMO $[Ca^{2+}]_i$ is still near 200 nM.

Many of the other cellular processes governed by Ca^{2+} do not take place in a thin shell near the membrane, but occur throughout the cytosol or in the nucleus. Measurements of cytosolic $[Ca^{2+}]$ in SCN neurons has been obtained using fluorescent probes (*Ikeda et al.*, 2003; *Irwin and Allen*, 2009). We will denote the concentration of Ca^{2+} in the cytosol as $[Ca^{2+}]_c$, and will use the same approach to model $[Ca^{2+}]_c$ as we used to model the concentration of Ca^{2+} in the shell near the membrane:

$$\frac{dCa_c}{dt} = p(-k_c I_{Ca} - b_c Ca_c) \tag{4.9}$$

Equation 4.9 is the same as Eq. 4.1, except here we have an additional factor $p = 0.001$

which represents the fraction of Ca^{2+} ions in the cytosol which are not bound. We calculate k_c as $\frac{1}{zFV_c}$=5.73× 10^{-6} mM/ms, where the volume of the cytosol, V_c, is taken to be the volume of a spherical cell with radius 5 μM. We determine b_c based on $[Ca^{2+}]_c$ imaging data in SCN neurons from *Irwin and Allen* (2009). In *Irwin and Allen* (2009), when $[Ca^{2+}]_c$ was measured in response to a 10-20 Hz train of action potentials, $[Ca^{2+}]_c$ was found to rise from around 50 nM and then saturate between 150 nM and 200 nM. In our model, when we set b_c=0.1 and simulate action potentials at around 7 Hz, we find that Ca_c rises from less than 50 nM and then saturates at 200 nM (Fig. 4.9A and C). We then simulated DLAMOs, and found that Ca_c rose to a value of around 1200 nM before saturating (Fig. 4.9B and C). The model predicts that a SCN neuron exhibiting DLAMOs would have a 6-fold higher level of $[Ca^{2+}]_c$ than a SCN neuron producing APs. Sustaining such a high level of $[Ca^{2+}]_c$ might be expected to be toxic to the cell, however the data discussed in Chapter 3 showed that *per1* neurons do indeed sustain DLAMOs for an extended period of time. Thus, our modeling suggests that *per1* neurons must have special calcium-handling mechanisms which allow them to survive in depolarized states.

4.3.4 Intercellular communication

As discussed in Chapter 2, the SCN is a network of neurons and it is the electrical activity of this network that communicates the time of day signal to other brain areas. Therefore, it is interesting to consider what effect, if any, a neuron exhibiting DLAMOs would have on other neurons in the SCN. Since GABA is the most prevalent neurotransmitter in the SCN and is typically responsible for fast inhibition, we simulated networks of two neurons coupled by an inhibitory $GABA_A$ synapse in order to predict the effect of DLAMOs on intercellular communication. We modeled the $GABA_A$ synapse using the formalism of *Destexhe and Sejnowski* (2001):

$$I_{GABA} = g_{GABA} s(V - E_{GABA}) \tag{4.10}$$

where $s(t)$ denotes the fraction of open channels with the dynamics:

$$\frac{ds}{dt} = \alpha_r[T](1 - s) - a_d s \tag{4.11}$$

with a_r=5 $\text{mM}^{-1}\text{ms}^{-1}$, a_d=0.18, E_{GABA}=-75 mV, and g_{GABA}=0.45 nS. $[T]$ denotes the concentration of neurotransmitter released into the synaptic cleft by a presynaptic spike, and is dependent on the voltage of the presynaptic neuron:

$$[T] = \frac{T_{max}}{1 + exp(-\frac{V_{pre} - V_T}{K_p})} \tag{4.12}$$

with T_{max}=1 mM, V_T=2 mV, and K_p=5 mV.

For our two-neuron networks, we took the pre-synaptic neuron to be a *per1* neuron, and the post-synaptic neuron to be a non-*per1* neuron modeled using the parameters from *Sim and Forger* (2007). When a non-*per1* neuron is not receiving any input, it fires APs at 4.7 Hz (Fig. 4.10C). We simulated a pre-synaptic *per1* neuron exhibiting either spontaneous APs (Fig. 4.10A) or spontaneous DLAMOs (Fig. 4.10B). When the pre-synaptic neuron is firing APs, the post-synaptic non-*per1* neuron fires APs at about 3.3 Hz (Fig. 4.10D). When the pre-synaptic neuron is exhibiting DLAMOs, the post-synaptic neuron fires APs at about 2.3 Hz (Fig. 4.10E). Thus, we predict that a *per1* neuron exhibiting DLAMOs can actually have a stronger inhibitory effect on the firing of its post-synaptic targets than a *per1* neuron firing APs.

Although GABA is typically an inhibitory neurotransmitter, there is evidence that GABA can also play an excitatory role within the SCN. *Wagner et al.* (1997) reported that GABA functions as an excitatory neurotransmitter in the SCN during the day. However, more recent data suggests that while GABA inhibits most SCN neurons, some level of GABA-mediated excitation was present regardless of the time

of day (*Choi et al.*, 2008). *Choi et al.* (2008) find that in a subset of SCN neurons, the reversal potential for GABA is above the threshold for firing action potentials, leading to excitatory responses to GABA signaling in these neurons. We can simulate this by raising E_{GABA} for the synapse in our model. We repeated the simulations shown in Fig. 4.10, but with E_{GABA} set to -30 mV rather than -75 mV, and g_{GABA} lowered to 0.05 nS. In this case, we found that the effect of the pre-synaptic neuron on the post-synaptic neuron was the same whether the pre-synaptic neuron was firing APs or exhibiting DLAMOs. For these simulations, when a non-*per1* neuron is not receiving any input, it fires APs at 2.7 Hz. When the pre-synaptic neuron was either firing APs or exhibiting DLAMOs, the post-synaptic neuron fired APs at an elevated rate of 3.3 Hz (simulations not shown).

4.3.5 Photic gating

Light pulses can phase shift circadian rhythms during the night but not during the day, a phenomenon known as photic gating. The mechanisms underlying photic gating in the circadian clock are not clear (*Lundkvist and Block*, 2005). The SCN receives photic information through the retinohypothalamic tract. This pathway involves glutamatergic input to SCN neurons via NMDA receptors. *Pennartz et al.* (2001) proposed that reduced NMDA receptor activity during the day prevents light signals from reaching the SCN, leading to the "dead zone" for photic phase shifts during the day. Here, we hypothesize that the inability of light to cause phase shifts during the day is due to *per1* neurons being in the depolarized quiescent state and thereby unresponsive to glutamatergic input.

To test this hypothesis in the model, we simulated two coupled neurons. The pre-synaptic neuron was firing regular action potentials, which induced a NMDA current in the post-synaptic neuron. The NMDA synapse was modeled as in *Destexhe and Sejnowski* (2001):

$$I_{NMDA} = g_{NMDA} s B(V)(V - E_{NMDA}) \tag{4.13}$$

where E_{NMDA}=0 mV, g_{NMDA}=0.6 nS, and $s(t)$ has the same form as Equation 4.11 but with a_r=0.072 $\text{mM}^{-1}\text{ms}^{-1}$ and a_d=0.0066.

Under normal physiological conditions, the NMDA receptor is blocked by magnesium ions, which can be removed if the post-synaptic neuron is depolarized. $B(V)$ represents the magnesium block:

$$B(V) = \frac{1}{1 + exp(-\frac{V - V_H}{16.13})} \tag{4.14}$$

where V_H is the half activation and is given by:

$$V_H = 16.13\ ln\frac{[Mg^{2+}]}{3.57} \tag{4.15}$$

where V_H ≈10 mV for a physiological [Mg^{2+}] of 2 mM.

We find that when the *per1* neuron is in the depolarized quiescent state (Fig. 4.11A), the excitatory input it receives has very little effect on its electrical behavior (Fig. 4.11B). The model indicates that the lack of an effect can be explained due to the sodium channels already being inactivated in the depolarized quiescent state, thus preventing any further depolarization despite the excitatory input. We hypothesize that this phenomenon, known as depolarization block, could be playing a role in preventing light from phase shifting the clock during the afternoon dead zone.

Unlike photic input, non-photic input (e.g. food access or other arousal-inducing stimuli) can phase shift the clock during the day (*Piggins and Cutler*, 2003). Furthermore, photic input *can* phase shift the clock during the day in the presence of non-photic stimuli (Mino Belle, personal communication). Microinjection of neuropeptide Y (NPY) into the SCN region phase advances rhythms during the day, emulating the effect of non-photic stimuli (*Piggins and Cutler*, 2003). NPY and GABA both relay

non-photic information from the intergeniculate leaflet to the SCN via the geniculo-hypothalamic tract (*Piggins and Cutler*, 2003). Since NPY and GABA both convey non-photic information, and GABA is known to have a predominantly inhibitory effect on SCN neurons, we modeled NPY as having an inhibitory effect on SCN neurons by adding a constant hyperpolarizing current of -0.5 pA to simulate injection of NPY. This current brought the neuron out of depolarization block and caused it to start firing (Fig. 4.11C), perhaps explaining why non-photic input is able to phase shift the clock in the afternoon. We then induced synaptic NMDA currents as before, but now found that the excitatory input caused an increase in the firing rate of the *per1* neuron (Fig. 4.11D). We hypothesize that this phenomenon could explain the observation that light can phase shift the clock during the afternoon dead zone when non-photic input is also present.

4.3.6 TTX-induced oscillations

Belle et al. (2009) was the first report of spontaneous depolarized membrane potential oscillations in SCN neurons. However, both *Pennartz et al.* (2002) and *Jackson et al.* (2004) previously reported depolarized membrane potential oscillations in unidentified SCN neurons in the presence of TTX. Subsequent application of nimodipine silenced these TTX-induced oscillations, similar to the effect nimodipine has on DLAMOs. In Fig. 4.12 we demonstrate that our model can also produce TTX-induced oscillations. We first simulated a *per1* neuron firing APs as our control. This simulation had all the same parameter values that we used to simulate DLAMO (Fig. 4.5B top trace), except for an increased $g_{K_{Ca}}$. We then simulated TTX by setting g_{Na} to 0, and the model behavior went from APs to depolarized oscillations. Keeping g_{Na}=0, we then simulated nimodipine in the presence of TTX by setting g_{Ca} to 20, and found that the oscillations were silenced.

4.3.7 Channel noise

The depolarized oscillations seen in *per1* neurons are quite noisy (Fig. 4.5A). It is difficult to determine how much of the observed noisiness is due to randomness in ion channel dynamics versus synaptic events. We have shown that incorporating synaptic noise into our simulations is capable of producing noisy oscillations similar to those recorded experimentally (Fig. 4.5B). Of course, this does not rule out the possibility that the stochastic nature of the opening and closing of ion channels is also playing a role. If the number of channels of a particular type in a cell is large enough, the randomness of individual channel responses average out and deterministic equations for channel gating should give a reasonable approximation of the whole-cell current. On the other hand, if the number of channels of a particular type in a cell is not large, then the randomness of individual channel responses may not average out and a stochastic gating model would be more appropriate for that channel type. *Kononenko and Dudek* (2004) identified a subthreshold voltage-dependent cation (SVC) channel present in SCN neurons with high single-channel conductance but low channel density (possibly as few as 75 SVC channels per cell). *Kononenko and Berezetskaya* (2010) formulated a stochastic model of these SVC channels and added a SVC current to the *Sim and Forger* (2007) model.

Here we study the effect of SVC channels on a model *per1* cell in DLAMO. The voltage-dependence of SVC channels is such that their open probability is significantly greater in the DLAMO voltage range than it is for more hyperpolarized potentials. We find that in the absence of synaptic noise, as few as $N = 5$ SVC channels are enough to produce noisy oscillations similar to our DLAMO recordings (Fig. 4.13B).

Kononenko and Berezetskaya (2010) also added a persistent or "slowly inactivating" sodium current, $I_{Na,S}$, to the Sim-Forger model. We did not study this current here because $I_{Na,S}$ is TTX-sensitive, and our data indicates that TTX has very little effect on DLAMOs (Fig. 4.5A). Thus, we reasoned that $I_{Na,S}$ does not play a critical

role in DLAMOs.

4.3.8 K^+ channel activation

The I_K current in our model is based on an outward voltage-dependent fast rectifying K^+ current recorded in SCN neurons by *Bouskila and Dudek* (1995). *Bouskila and Dudek* (1995) obtained an activation curve for this current based on the assumption that I_K is linearly proportional to the driving force (V-E_K), which they justified by noting that the instantaneous current-voltage relations were linear between -70 and 10 mV. *Clay* (2009) reviewed the determination of K^+ channel activation curves from K^+ channel currents, and on the basis of several studies in squid giant axon and other preparations argues that I_K has a non-linear dependence on (V-E_K) for physiological conditions which is well described by the Goldman-Hodgkin-Katz (GHK) current equation. *Clay* (2009) then revisited the *Bouskila and Dudek* (1995) data and fit an activation curve for their I_K based on normalization using GHK rather than (V-E_K). The revised activation curve is steeper and shifted leftward on the voltage axis relative to the original curve. The *Clay* (2009) curve is given by $(\alpha_n/(\alpha_n + \beta_n))^4$ with:

$$\alpha_n = \frac{-0.01(V + 30)}{exp(-0.08(V + 30)) - 1} \tag{4.16}$$

$$\beta_n = 0.125exp(-\frac{V + 40}{30}) \tag{4.17}$$

For all the simulations described in this chapter up to this point, we used the original *Bouskila and Dudek* (1995) activation curve rather than the *Clay* (2009) curve. However, all of our simulation results can be obtained using either activation curve as demonstrated by Figs. 4.14 and 4.15.

4.4 Discussion

In this chapter, we refined our model of *per1* neurons to include calcium-activated potassium currents. Our refined model can reproduce the TTX-induced oscillations reported in unidentified SCN neurons in *Pennartz et al.* (2002) and *Jackson et al.* (2004), while the original model from *Sim and Forger* (2007) cannot (data not shown). Based on our modeling results, we predict that TTX-induced oscillations occur only in *per1* neurons, and do not occur in non-*per1* neurons. This prediction can be tested experimentally by making patch-clamp recordings from the SCN of mice expressing the green fluorescent protein reporter for *per1* as described in Chapter 3.

We also used our refined model to make predictions about intercellular communication in the SCN. Based on simulations with two coupled cells, we predicted that a pre-synaptic neuron exhibiting DLAMOs can have a stronger inhibitory effect on a post-synaptic neuron than a pre-synpatic neuron firing APs. This prediction can be tested experimentally using the dual-patch technique, where two cells are recorded from simultaneously. Also, this finding based on two coupled cells indicates it would be very interesting to revisit network simulations with thousands of SCN neurons as performed in Chapter 2, but with distinct populations of *per1* and non-*per1* neurons in the network.

Our predictions in this chapter regarding photic gating of the circadian clock centered on the concept of depolarization block. Outside of *Belle et al.* (2009), depolarization block has not been reported in SCN neurons and the idea is somewhat controversial. Nevertheless, depolarization block is an established phenomenon in neurons in other brain areas. For example, *Wong et al.* (2005) shows depolarization block in mammalian intrinsically photosensitive retinal ganglion cells (ipRGCs), which are actually upstream of SCN neurons in the non-image forming visual pathway. Furthermore, depolarization block can be seen in a variety of neuronal models, including the classical Hodgkin-Huxley model (*Borisyuk and Rinzel*, 2005).

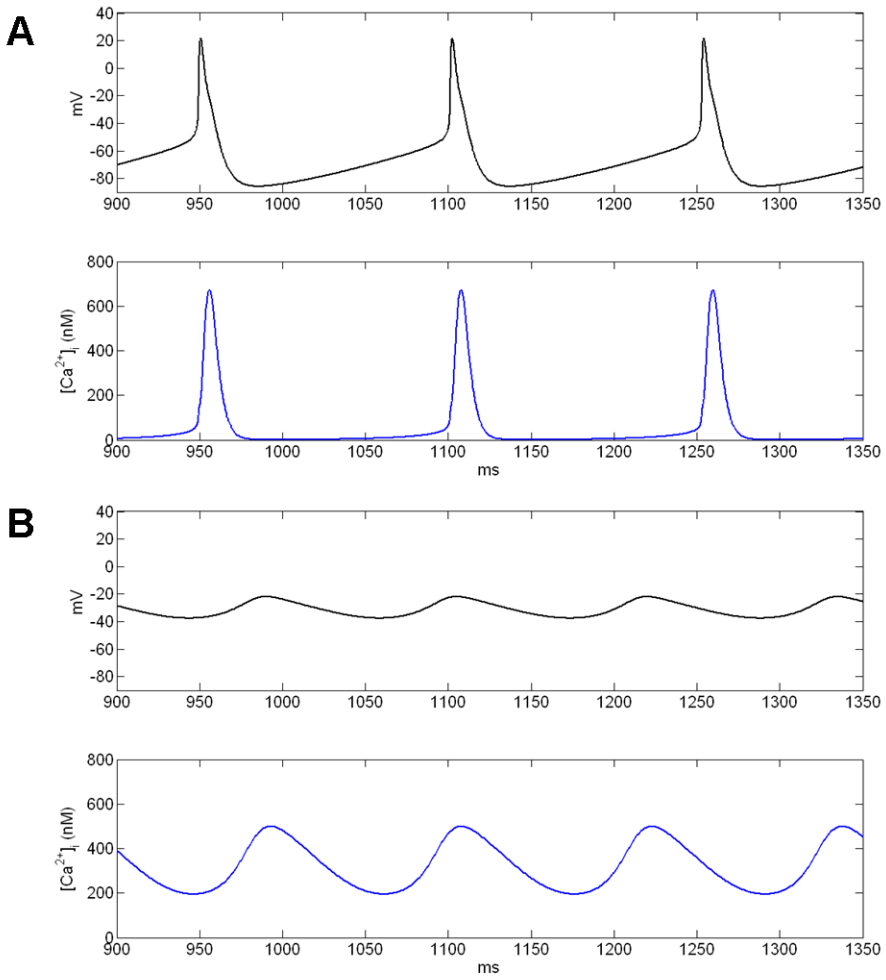

Figure 4.8: Ca^{2+} dynamics during APs and DLAMOs. (**A**) Model producing spontaneous APs with g_{Ca}=26 nS, g_K=3 nS, and g_{KCa}=200 nS. $[Ca^{2+}]_i$ peaks at 670 nM during an AP, and decays to near zero (1 nM) in betwen APs. (**B**) Model producing spontaneous DLAMOs with g_{Ca}=26 nS, g_K=3 nS, and g_{KCa}=4 nS. $[Ca^{2+}]_i$ is around 500 nM at the peak of the oscillation, and around 200 nM at the trough.

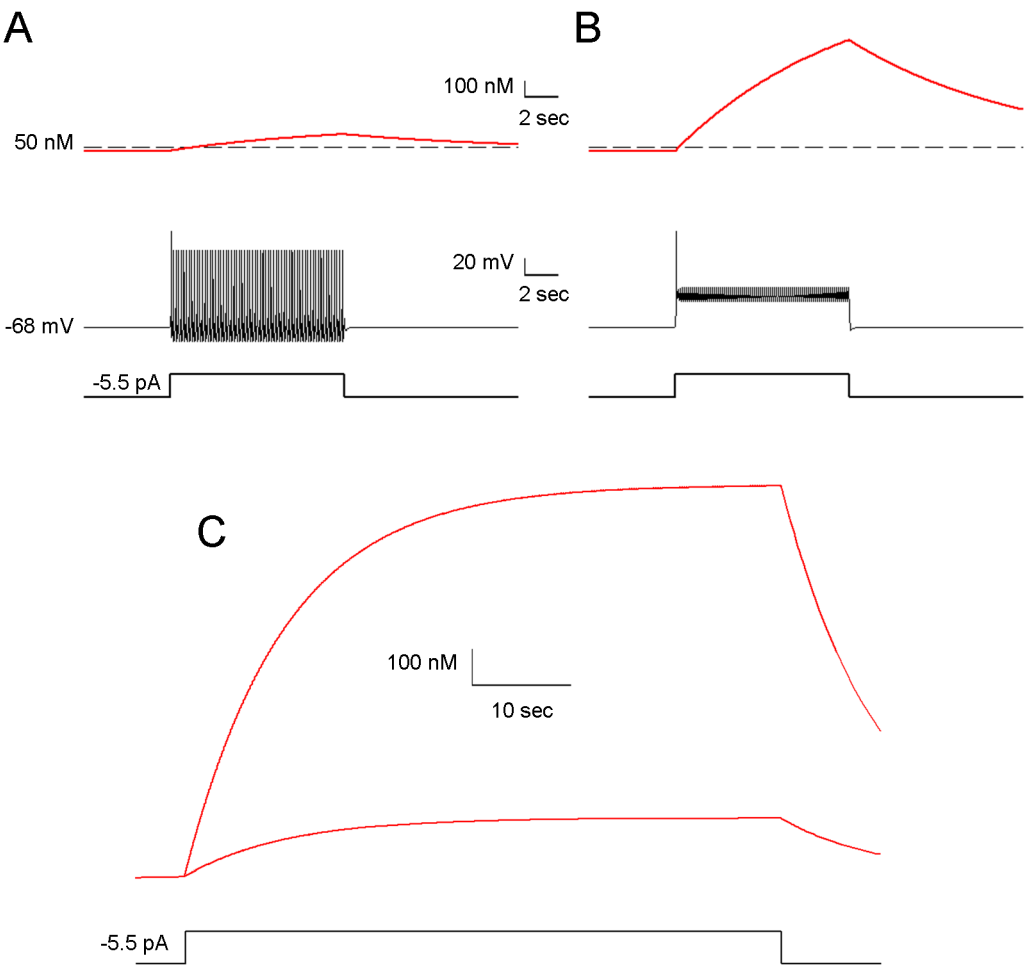

Figure 4.9: Ca^{2+} in a cell displaying DLAMOs. Release of hyperpolarizing current (-5.5 pA) allows model *per1* neuron to spontaneously fire APs (A) or display DLAMOs (B). (**A**) Model *per1* neuron firing APs with a frequency around 7 Hz. Each AP leads to a $[Ca^{2+}]_c$ increase of about 5 nM, consistent with *Irwin and Allen* (2009). (**B**) Model *per1* neuron displaying DLAMOs with a frequency around 8 Hz and $[Ca^{2+}]_c$ response. (**C**) $[Ca^{2+}]_c$ saturates at around 200 nM during APs (*bottom trace*), and at around 1200 nM during DLAMOs (*top trace*).

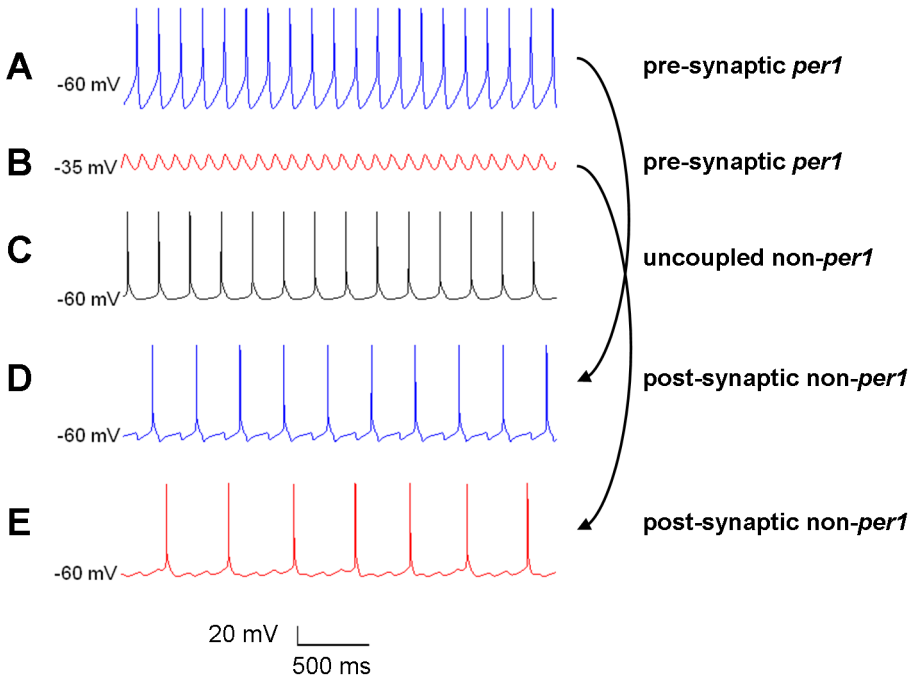

Figure 4.10: Role of DLAMOs in intercellular communication. Simulations of pre-synaptic *per1* neurons connected to post-synaptic non-*per1* neurons via an inhibitory $GABA_A$synapse. The neuron shown as (**A**) is firing APs and is connected to neuron (**D**), the neuron shown as (**B**) is exhibiting DLAMOs and is connected to neuron (**E**), and neuron (**C**) is not connected to any other neurons and so serves as a control for the firing rates of the post-synaptic neurons. The pre-synaptic APs from **(A)** caused **(D)** to fire more slowly than the uncoupled neuron **(C)**, but the pre-synaptic DLAMOs from **(B)** caused **(E)** to fire even more slowly than **(D)**. Non-*per1* neurons were modeled using the parameters from *Sim and Forger* (2007).

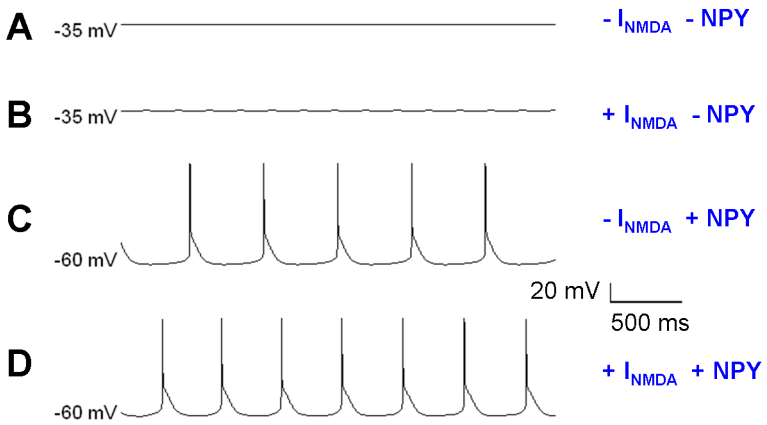

Figure 4.11: Role of depolarized quiescent state in photic gating. (**A**) Simulation of a *per1* neuron in the depolarized quiescent state, not receiving NMDA or NPY input. (**B**) The *per1* neuron from (A) receiving NMDA but not NPY input. The excitatory input has very little effect on the electrical behavior of the neuron, due to sodium channel inactivation (depolarization block). (**C**) The *per1* neuron from (A) receiving NPY but not NMDA input. The NPY input brings the neuron out of depolarization block and it fires APs. (**D**) The *per1* neuron from (A) receiving both NMDA and NPY input. The NMDA input causes the neuron to fire at a faster rate than in (C). Taken together, these simulations indicate that depolarization block can explain why photic stimuli (NMDA input) cannot phase shift the clock during the afternoon, while non-photic stimuli (NPY input) can.

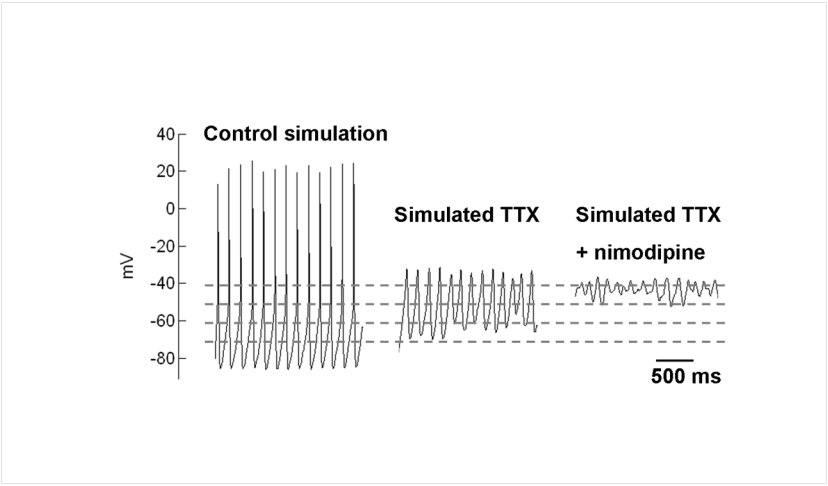

Figure 4.12: Membrane potential oscillations in SCN neurons in the presence of TTX. Model *per1* neuron generating APs (control simulation, g_{Na}=229 nS, g_{Ca}=26 nS, $g_{K_{Ca}}$=200 nS). Simulated application of TTX (g_{Na}=0) induces depolarized oscillations, and simulated application of TTX plus nimodipine (g_{Na}=0, g_{Ca}=20 nS) silences the oscillations. These simulations reproduce the behavior of Figure 3B from *Jackson et al.* (2004), which shows the effect of cumulative application of 300 nM TTX and 2 μM nimodipine to a SCN neuron firing spontaneously.

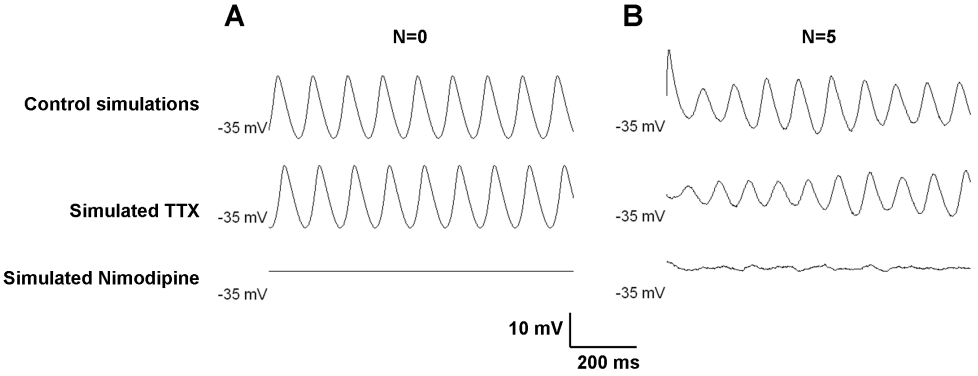

Figure 4.13: Role of I_{SVC}, L-type Ca^{2+}, and TTX-sensitive Na^{+} channels in mediating DLAMOs. Simulations use all the same parameters as Figure 2B, except here there is no synaptic noise I_{syn}. (**A**) Model *per1* neuron with no noise (N=0 SVC channels). (**B**) Model *per1* neuron with N=5 SVC channels.

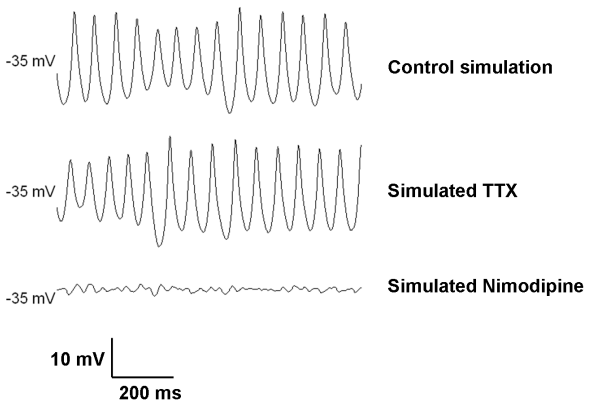

Figure 4.14: Role of I_K activation, L-type Ca^{2+}, and TTX-sensitive Na^+ channels in mediating DLAMOs. Simulations use all the same parameters as Fig. 4.5B, except here we use the *Clay* (2009) activation curve for I_K and increased values of g_{Ca}. Model *per1* neuron (g_{Na}=229 nS, g_{Ca}=43.7 nS) displaying DLAMOs (*top trace*). Simulated application of TTX (g_{Na}=0) does not abolish DLAMOs (*middle trace*). Simulated application of nimodipine (g_{Ca}=30 nS) abolishes DLAMOs (*bottom trace*).

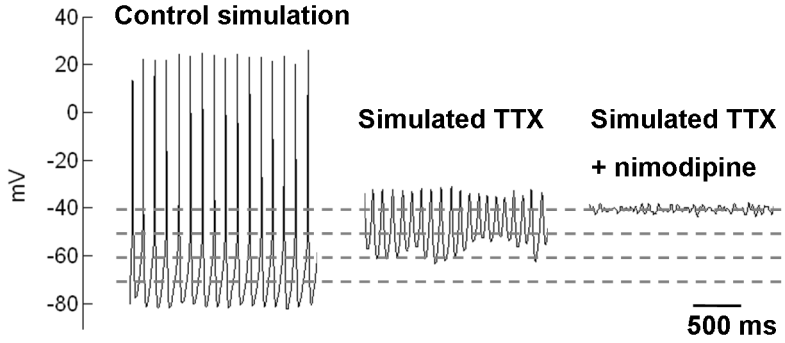

Figure 4.15: I_K activation and membrane potential oscillations in SCN neurons in the presence of TTX. Simulations use all the same parameters as Fig. 4.12, except here we use the *Clay* (2009) activation curve for I_K. Model *per1* neuron generating APs (control simulation, g_{Na}=229 nS, g_{Ca}=26 nS). Simulated application of TTX (g_{Na}=0) induces depolarized oscillations, and simulated application of TTX plus nimodipine (g_{Na}=0, g_{Ca}=20 nS) silences the oscillations.

CHAPTER V

Statistical significance of sequential firing patterns in multi-neuronal spike trains

5.1 Introduction

Sequential firings with fixed time delays are frequently observed in simultaneous recordings from multiple neurons. Such temporal patterns are potentially indicative of underlying microcircuits and it is important to know when a repeatedly occurring pattern is statistically significant. These sequences are typically identified through correlation counts. In this chapter we present a method for assessing the significance of such correlations. We specify the null hypothesis in terms of a bound on the conditional probabilities that characterize the influence of one neuron on another. This method of testing significance is more general than the currently available methods since under our null hypothesis we do not assume that the spiking processes of different neurons are independent. The structure of our null hypothesis also allows us to rank order the detected patterns. We demonstrate our method on simulated spike trains.

Detection of temporal firing patterns among groups of neurons is an important task as these patterns are potentially indicative of functional cell assemblies or microcircuits present in the underlying neural tissue (*Hebb*, 1949; *Brown et al.*, 2004). Com-

putational methods (e.g., the two-tape algorithm (*Abeles and Gerstein*, 1988)) which discover repeating occurrences of precise firing sequences in simultaneous recordings from multiple neurons have been used to assess activity patterns in cortical structures *in vivo* (*Nadasdy et al.*, 1999), in slice preparations (*Ikegaya et al.*, 2004), and in cultures of dissociated cortical neurons (*Rolston et al.*, 2007). Methods such as the two-tape algorithm count the occurrences of a precisely timed pattern (e.g., the 3-neuron pattern $A[T_1]$-$B[T_2]$-C where a spike from neuron A is followed by a spike from neuron B after a delay of T_1 time units and a spike from neuron C after a further delay of T_2 time units) by finding correlations among time shifted spike trains. Several methods have been developed to determine the statistical significance of such patterns based on how many times they occur (*Prut et al.*, 1998; *Tetko and Villa*, 2001; *Abeles and Gat*, 2001). To assess significance, often one employs a null hypothesis that assumes that all neurons spike as (possibly nonhomogeneous) Poisson processes and that different neurons are independent. In a class of empirical methods (*Hatsopoulos et al.*, 2003; *Amarasingham*, 2004; *Gerstein*, 2004), one generates many surrogate data streams by systematically perturbing the spikes in the original data. The significance of a pattern is then determined by noting the difference in correlation counts (or in any other statistic derived from the counts) for these patterns in the original data and in the surrogate streams. These "jitter" methods allow for a lot of flexibility regarding the assumed statistical model for a spike train because the perturbations can be designed to preserve any assumed distribution for inter-spike intervals. However, the implicit null hypothesis here amounts to assuming independence because spike trains of different neurons are independently perturbed to obtain the surrogate spike trains.

In this chapter, we present a method for analyzing the statistical significance of sequential firing patterns that goes beyond the currently available techniques by allowing the null hypothesis to include "weak dependence" among neurons, and by rank

ordering significant patterns according to the "strength of influence" among participating neurons. The ability to discriminate significant patterns representing strong influences from those representing weak influences is a useful feature considering that the cortical network has been described as a skeleton of strong connections in a sea of weaker ones (*Song et al.*, 2005).

5.2 Methods

5.2.1 Correlation Count

For simplicity of exposition, we first explain the method for a pattern of only two neurons, $A[T]$-B. Suppose we find the number of repetitions of this pattern in the data using simple correlation as follows. Let $t_1, t_2, \ldots, t_n$ denote all time instants at which there is a spike from any neuron in the data. Let:

$$f_{AB} = \sum_{i=1}^{n} I_A(t_i) I_B(t_i + T) \tag{5.1}$$

where for any neuron x, $I_x(t)$=1 if there is a spike from x at time t and zero otherwise. Note that f_{AB} is simply a correlation integral which counts the number of spikes from A that are followed by a spike from B with a delay of exactly T time units, and hence counts the number of repetitions of our pattern. If we want to allow for some small random variations in the delay we can define the indicator variable $I_x(t)$ to take value 1 if there is a spike in a time interval of length Δ centered around t. (For example, we can take Δ to be the time resolution in our measurements. From now on we assume that Δ is small enough so that the probability of getting more than one spike from the same neuron in Δ is negligible). Most current methods for detecting sequential firing patterns rely on correlation counts as described above. Since the focus of this chapter is on statistical significance (and not on computational efficiency), we simply assume that one can calculate such counts for pairs of neurons and for various delays

T of interest. The question of interest is "how large should the count be to conclude that the pattern represents a significant positive influence of A on B?" (By a positive influence of A on B, we mean that A and B are correlated in the sense of having a high value for the count given by Eq. 5.1. We do not mean to imply that A causes B to fire, since any method that relies only on correlations can not distinguish between true causation and accidental correlation).

Since we want to address this question in a classical hypothesis testing framework without assuming independence, we need to choose a null hypothesis that includes as many models as possible of interdependent neurons without any "strong" positive influences between pairs of neurons. In addition, we want the null hypothesis to contain a parameter to denote the strength of influence so that we can rank order all significant patterns.

5.2.2 Significance test

Here we characterize the strength of influence between any pair of neurons in terms of a conditional probability as proposed in *Sastry and Unnikrishnan* (2010). Let $e(B|A,T,t)$ denote the conditional probability that B will fire at time $t+T$ (or more precisely, in a time interval around $t+T$ given that A has fired at time t). We assume that $e(B|A,T,t)$ is the same for all t and hence denote it by $e(B|A,T)$. (The implications of this and other assumptions are discussed in Sec. 5.2.3.) We employ the following composite null hypothesis: Any model of interacting neurons is in our null hypothesis if it satisfies $e(Y|X,T) \leq e_0$ for all neurons X, Y and a set of specified delays T, where e_0 is a user-chosen constant. The parameter e_0 is essentially a threshold on the conditional probability below which positive influences are deemed "weak". For example, if all neurons are independent homogeneous Poisson with rate 5 Hz and Δ=1 ms, the conditional probability for any pair is about 0.005. Hence, if we choose e_0=0.05, it means that when we reject the null hypothesis we can say that

the influences represented by the pattern are at least 10 times stronger than those in the case of independence.

To get a test for statistical significance we need to calculate a bound on the probability that, under this null hypothesis, the count f_{AB} is above a given threshold. For this, we proceed as follows. Suppose L is the total time duration of the data and let the random variable $N_A(L)$ denote the total number of spikes by neuron A during this time. Define:

$$S_{AB} = \sum_{i=1}^{N_A(L)} X_i \tag{5.2}$$

where X_i are independently and identically distributed 0-1 random variables with $\Pr[X_i{=}1]{=}(1\text{-}\Pr[X_i{=}0]){=}p$. If we take $p = e(B|A,T)$, it is easy to see that S_{AB} is equivalent to f_{AB} since every time there is a spike from A, with probability p a spike from B would follow with the appropriate delay. Now we assume that the spiking of A is Poisson. This implies that, since the X_i's are 0-1 random variables, S_{AB} is also a Poisson random variable (*Ross*, 1996). The mean and variance of S_{AB} are given by *Ross* (1996):

$$E[S_{AB}] = E[N_A(L)]E[X_i] \tag{5.3}$$

$$Var[S_{AB}] = E[N_A(L)]E[X_i^2] \tag{5.4}$$

Since under the null hypothesis, $e(B|A,T) \leq e_0$, taking $p = e_0$ will allow us to get a bound on the probability of S_{AB} exceeding a threshold.

The test of statistical significance is as follows. Let e_0 be the bound on conditional probability that we choose for our null hypothesis and α be the allowed Type I error. Let λ_A be the rate of firing for the first neuron in the pattern and L be the total time duration of the data. Set $\lambda_Z{=}e_0 L \lambda_A$. Using the cumulative distribution of a

Poisson random variable with parameter λ_Z, we calculate the M needed to satisfy $\Pr[Z > M] \leq \alpha$. This M is the threshold on the count of the pattern for us to be able to reject the null hypothesis and declare the pattern to be significant. To calculate M, we need λ_A. This can be estimated from the data as the average rate of firing for neuron A. Figure 5.1D shows the threshold M as a function of e_0. The method is easily generalized to longer patterns. Consider pattern $A[T_1]$-$B[T_2]$-C. We get counts f_{ABC} by 3-point correlations. We define S_{ABC} as before but with $p{=}e(B|A,T_1)e(C|B,T_2)$. S_{ABC} would be same as f_{ABC} if all influence of A on C comes through B. Even otherwise, S_{ABC} would be a lower bound on the correlation count and hence it is enough to bound the probability of S_{ABC} exceeding a threshold. Since all conditional probabilities are bounded above by e_0 under our null hypothesis, we can calculate the needed threshold by taking $\lambda_Z{=}e_0^2 L\lambda_A$. For a pattern involving n neurons, we calculate the threshold M needed to satisfy $\Pr[Z > M] \leq \alpha$ where $\lambda_Z{=}e_0^{n-1} L\lambda_A$.

5.2.3 Discussion of methodology

We assume that the conditional probability $e(B|A,T,t)$ is independent of t. This conditional probability is well defined whether or not A is connected to B. If most of the contribution to this conditional probability comes from the A to B synapse then this assumption amounts to saying that the synaptic strength does not change much during the time interval of data recording. On the other hand, if A is not connected to B, then the assumption is essentially an assumption on the stationarity of some relevant network-level statistics of joint probabilities of relevant groups of neurons. Under such a stationarity assumption, even patterns that are due to network activity rather than microcircuits can be handled using our method.

Our null hypothesis does not assume that the spiking processes of different neurons are independent. When we reject the null, we can assert with a high confidence that

the count for this pattern can not be this high unless the strengths of influences among these neurons (measured in terms of conditional probabilities) are above the threshold e_0. One value for e_0 corresponds to independence of neurons which is what is assumed in the null in existing methods. Our method of user-chosen e_0 allows the user another dimension of flexibility to discover patterns significant at different levels of strength of influence. This we feel is the main novelty of the method proposed here.

To derive our test of significance we assumed that the first neuron in the pattern is Poisson. This allowed us to show that the count of a pattern is Poisson even if the neurons are not independent. For our method, the essential thing is that the pattern count is Poisson. Other researchers have also assumed that the count is Poisson, as long as the occurrences of patterns are stochastically independent as one would expect them to be under most physiological conditions (*Abeles and Gat*, 2001). In this sense we do not feel that our assumption is too restrictive. In practice, we found that the analytically derived threshold of our method works well even when the Poisson assumption is not strictly satisfied.

5.3 Results

5.3.1 Network simulations

We simulated a network of 25 neurons, labeled A through Y, with three embedded patterns (*G-M-R*, *I-S-C*, *W-O-L*). A schematic of the network and details of the patterns are given in Fig. 5.1A. The synaptic strengths of these patterns (expressed as a conditional probability) ranged from 0.05 to 0.15 in accordance with the range of strengths found in typical recordings from the cortex (*Abeles*, 1991). The nominal firing rate of each neuron (5 Hz) was modulated at time intervals of Δ=1 ms based on all inputs the neuron received (details of the neuronal network simulator used for this

chapter are given in *Patnaik et al.* (2008)). All neurons had an absolute refractory period of 1 ms, and all synapses had delays between 1 and 10 ms. In addition to the embedded patterns, each neuron was randomly connected to 25% of the other neurons in the network with strengths chosen uniformly from the interval [0.0025, 0.01]. With an average firing rate of 5 Hz, the unconditional probability of a neuron firing in an interval of length Δ is about 0.005, which is also the conditional probability if the neurons are independent. Hence the interval from which the strengths of the random connections were chosen spanned a factor of 2 on either side of the independent case and modulated the firing rate of the neurons from 2.5 Hz to 10 Hz based on the input received.

Our method of assessing significance assumes that the number of times a pattern occurs is Poisson distributed. Due to the absolute refractory period and the modulation of firing rates based on spiking of other neurons, the spiking processes of individual neurons are not approximately Poisson as shown in Fig. 5.2A. However, the count for one of the embedded patterns, G-M-R, was approximately Poisson (Fig. 5.1C and 5.2B). Indeed, in simulations with L=300 s, the count of G-M-R was still approximately Poisson distributed when random connections spanned a factor of 5 on either side of independence (Fano factor for count of G-M-R was 0.97 $\pm$ 0.04 (mean $\pm$ s.e.m) based on 20 trials of 50 simulations).

5.3.2 Assessing and rank ordering significance of patterns

We simulated our network for 1,000 replications and compared the distribution of actual pattern counts in the simulated data to our analytically calculated thresholds for the patterns to be significant at different values of e_0. Figure 5.3A demonstrates our method was effective in assessing the varying strengths of the embedded patterns via the user-chosen parameter e_0.

We then ran the two-tape algorithm (*Abeles and Gerstein*, 1988) on a simulated

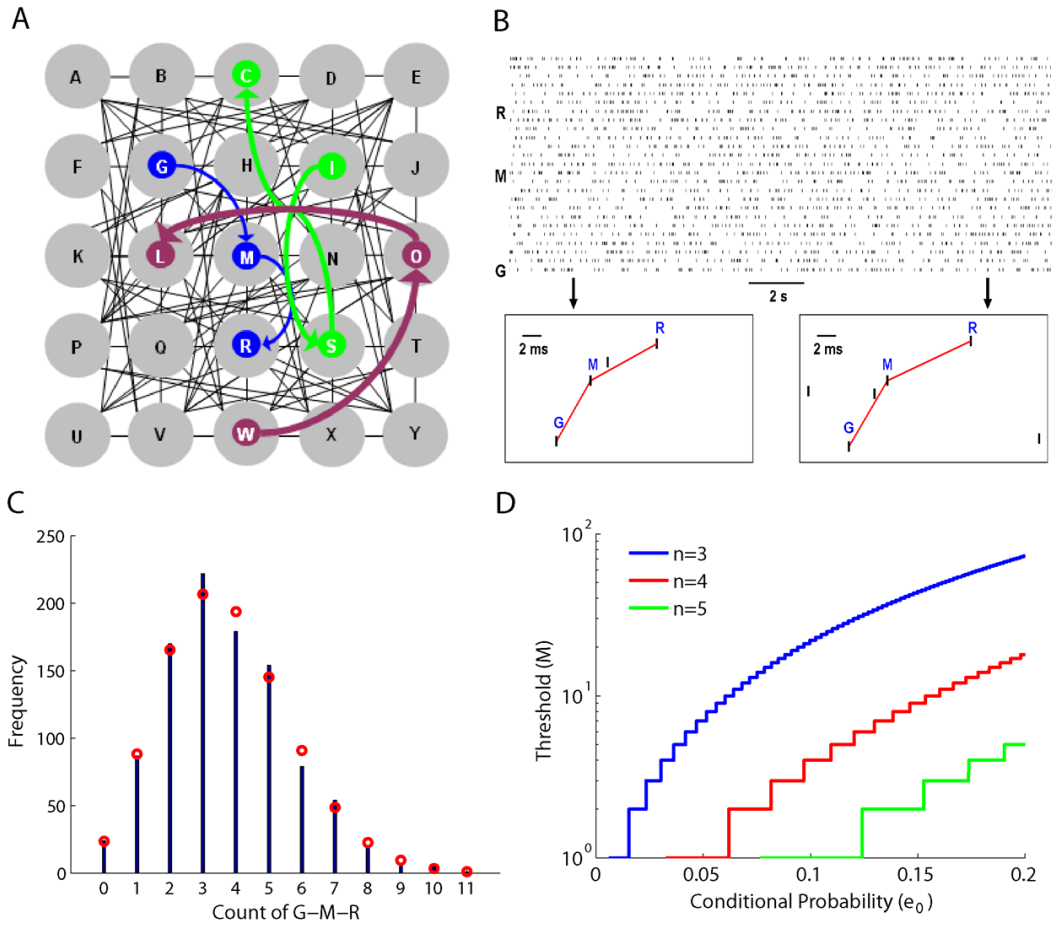

Figure 5.1: Network simulation, pattern count, and count threshold characteristics. (**A**) Schematic of a 25-neuron network with three 3-neuron chains of strong excitatory connections. The delays (in ms) and strengths (as conditional probabilities) in the chains are (denoted as Neuron 1 [delay,strength]-Neuron 2,...): G[3,0.05]-M[7,0.05]-R; I[8,0.1]-S[4,0.1]-C; and W[5,0.15]-O[6,0.15]-L. Simulation settings: L=300s, λ=5 Hz, refractory period 1 ms, random connections as described in text, firing rates updated every 1 ms. (**B**) Raster plot of 20 s worth of data from the simulation. There are two occurrences of the pattern G-M-R in the data shown here, but one cannot easily identify the patterns using visual inspection. (**C**) Count histogram of the pattern G-M-R over 1,000 simulations demonstrating that the count of a pattern is approximately Poisson distributed. Red circles are the Poisson distribution with $\lambda=(0.05^2)(300)(5)=3.75$. (**D**) Threshold calculated for n=3-,4-, and 5-neuron patterns with Type I error α=0.05 as a function of pattern strength for λ_A=5 Hz and L=300 s.

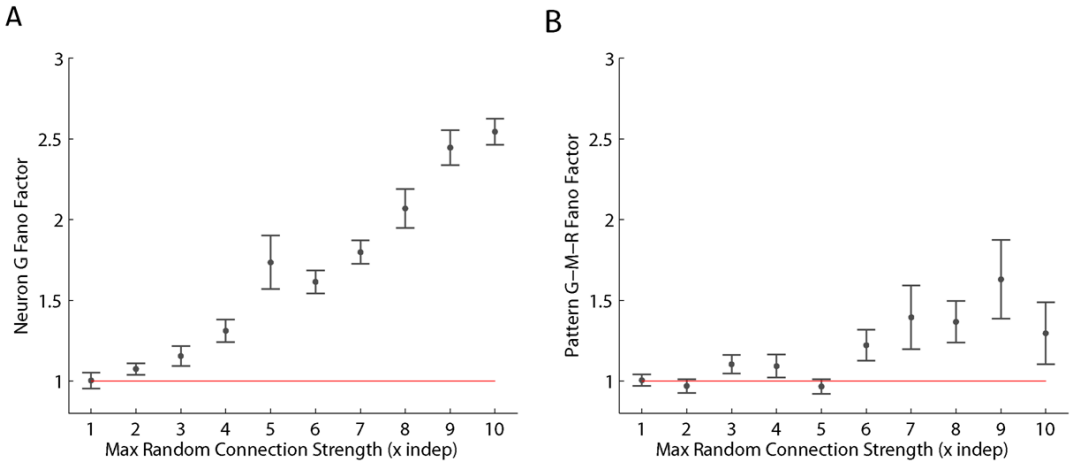

Figure 5.2: Simulation results showing that even when the counts of the first neuron in the pattern are not approximately Poisson, the count of the pattern is still approximately Poisson as long as the random connections strengths are not too high. Simulation settings: L=300 s, λ=5 Hz, refractory period 1 ms, random connections with 25% connectivity, firing rates updated every 1 ms. For each simulation, random connection strengths were uniformly drawn from a range of values. The x-axis indicates the maximum possible random connection strength (in terms of how many times stronger than independence) for each simulation. (**A**) Fano factor of neuron G over 1,000 simulations (50 trials of 20 simulations) demonstrating that the count of neuron G is not approximately Poisson distributed unless there are no random connections. (**B**) Fano factor of pattern G-M-R over 1,000 simulations (50 trials of 20 simulations) demonstrating that the count of pattern G-M-R is approximately Poisson distributed with weak random connections.

dataset to count the occurrences of all 3-neuron patterns that occurred at least twice (with a maximal delay of 200 ms between the first and last spikes in any pattern). We found 3,340 3-neuron patterns that occurred at least twice (Fig. 5.3B). Since so many patterns exceed the threshold, we need some additional criteria to select which of these individual patterns are the best candidates for further analysis. *Abeles and Gerstein* (1988) remarked that this selection process is very important, and called for future research to be conducted in this area. Using our framework, by having different values for e_0 in the null hypothesis, we can ask what patterns are significant at what value of e_0 and thus rank order patterns. This is easily seen from Fig. 5.3B, where we show count thresholds corresponding to different values of e_0. For example, if we chose e_0=0.05 (i.e., conditional probability is ten times that in the case of independence), then the number of candidates came down to 4. Thus, our compound null hypothesis with the user-chosen parameter e_0 helps one distinguish the most interesting patterns for further investigation, e.g. to correlate to behavioral events, from weaker patterns that may only be marginally significant. The commonly used "jitter" methods of determining significance of patterns are not useful in this regard. Of the 3,340 3-neuron patterns that occurred more than twice, creating 100 surrogate data streams using spike jitter as in *Date et al.* (1998) tells you that 808 patterns have a p-value less than 0.05, but gives little information about which of these patterns are the best candidates to select for further analysis. Another example demonstrating how the parameter e_0 in our null hypothesis provides a convenient handle for further analysis of the significant patterns is given in Table 5.1.

The patterns discovered as significant as shown in Fig. 5.3B are "rare", in the sense that only a very small fraction of the spikes of the neurons (less than 1%) contribute to the occurrence of patterns. The raster scan of part of the data on a typical simulation run of our network is shown in Fig. 5.1B, where we also highlight a few occurrences of one of the patterns. The embedded patterns are not obvious

No. of 3-node patterns that occurred more than once	6,115
No. of these patterns deemed significant... using basic spike jitter	1,640
using threshold e_0 = independence	6,115
using threshold $e_0 = 2 \times$ independence	6,115
$3 \times$	2,167
$4 \times$	1,024
$5 \times$	375
$6 \times$	131
$7 \times$	43
$8 \times$	28
$9 \times$	20
$10 \times$	18
$11 \times$	9
$12 \times$	6
$13 \times$	4
$14 \times$	3
$15 \times$	1
$16 \times$	1
$17 \times$	0

Table 5.1: Simulation results showing that using our method e_0 gives an extra handle to control false positives. Simulation settings: L=300 s, λ=5 Hz, refractory period 1 ms, random connections with strengths uniformly distributed between 0.00025 and 0.1 with 25% connectivity, firing rates updated every 1 ms. No strong patterns embedded. To determine pattern significance using basic spike jitter, 100 surrogate data streams were created by jittering all spikes with a jitter window of 2 ms.

upon visual inspection. In the full data for Fig. 5.3B (which is of 300 s duration), the patterns W-O-L and I-S-C occur 32 and 14 times respectively. The total number of spikes from neurons W, O, L, I, S, and C are, respectively, 1486, 1733, 1753, 1579, 1692, and 1646.

In Sec. 5.2.3, we mentioned that the conditional probability, $e(B|A,T)$, is well defined even when A is not connected to B. We show, in Fig. 5.3C, how our method can be useful in analyzing certain patterns that result due to network activity rather than two neurons directly influencing each other. We used a network of 50 neurons where each neuron was randomly connected to 25% of other neurons with strengths

between 0.0025 and 0.01. Neurons 1 to 48 were each connected to both 49 and 50 through weak connections (strength 0.01). All connections into 49 had delays of 100 ms, all connections into 50 had delays of 200 ms, and the random connections had delays between 1 and 200 ms. The connection strengths were such that input from a subset of the 48 neurons was enough to make both 49 and 50 likely to fire. Synchronous firing of a random subset of the 48 neurons (7.2 of them on average) was induced via an external input that fired with a rate of 5 Hz. Thus the pattern 49[100 ms]-50 was expected to occur often even though there is no connection between 49 and 50. The pattern 49[100 ms]-50 had the highest count and was significant, by our analytical method, at e_0=0.13 (Fig. 5.3C), while no other 2-neuron patterns were significant at this e_0. Note that this pattern has a long delay, which is typical of the precisely timed patterns that have been found to repeat in experimental recordings (*Abeles*, 1991). An example showing the use of our method to detect patterns arising from network activity in the form of "synfire chains" (*Abeles*, 1982, 1991) is given in Figs. 5.4 and 5.5.

5.3.3 Comparison with other methods

The parameter e_0 in our compound null hypothesis helps in rank ordering significant patterns as shown in Fig. 5.3A. Initially this may appear unnecessary because in any significance analysis, a given value of count (or any other statistic) provides a p-value for rejecting the null and it might be possible to rank order significant patterns using their p-values. However, this is often not feasible because the p-values do not actually give proper indication of relative strengths of different patterns. To demonstrate this, we simulated our network with random connections and two embedded patterns of different strengths (I-S-C with strength 0.1, and W-O-L with strength 0.15). We then computed p-values for the significance of these two patterns using a variety of methods in the literature (see Fig. 5.6). The first method we considered

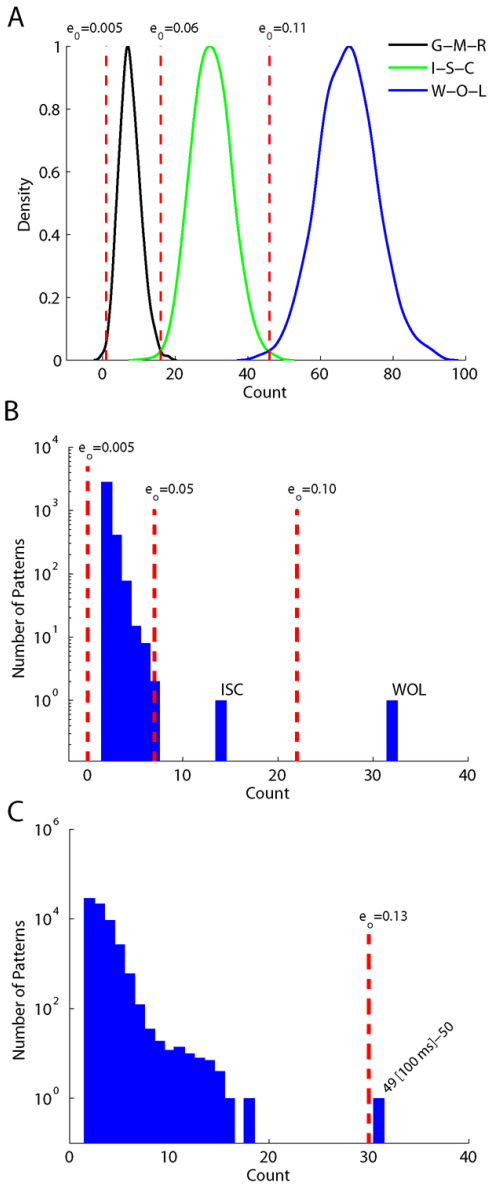

Figure 5.3: Rank ordering of patterns discovered in network simulations by connection strength. (**A**) Count densities of embedded patterns over 1,000 replications of a 600 second simulation of the 25-neuron network with random connections and strong connections as shown in Fig. 5.1A. Thresholds corresponding to e_0=0.005 (independence), 0.06, and 0.11. (**B**) Two-tape algorithm counts of all patterns that occur more than twice in 300 seconds of simulation. Simulation settings as in Fig. 5.1A, with only two strong patterns embedded (*I-S-C* with strength 0.1, and *W-O-L* with strength 0.15). Thresholds corresponding to e_0=0.005, 0.05, and 0.10 demonstrate the ability to discriminate strong significant patterns from weaker ones. (**C**) Two-tape algorithm counts of all patterns that occur more than twice in 20 seconds of the "network activity" simulation as described in Sec. 5.3.2, demonstrating the usefulness of our method for patterns generated by mechanisms other than microcircuits.

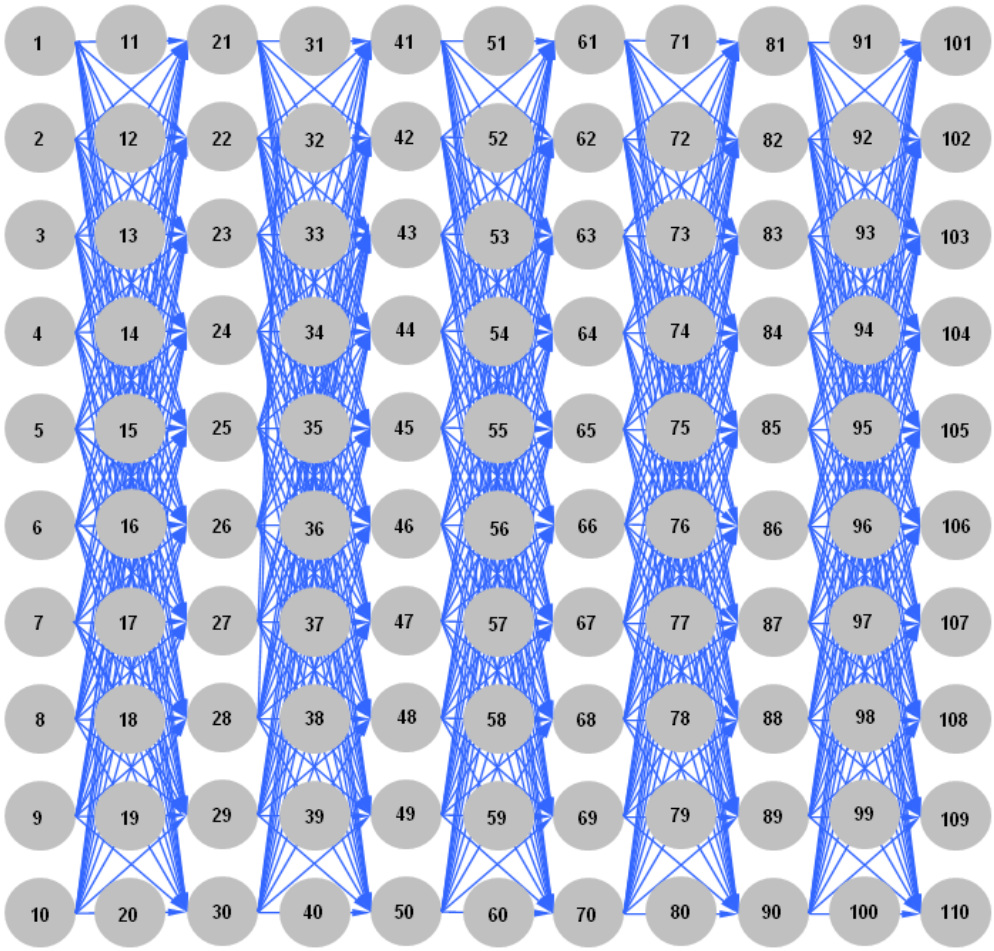

Figure 5.4: Simulation schematic of a synfire chain. Neurons 1 through 10 were triggered to fire synchronously with a rate of 5 Hz. Each of neurons 1 through 10 synapses onto neurons 21 through 30, with a connection strength of 0.01 and a delay of 10 ms. Likewise, neurons 21 through 30 then synapse onto 41 through 50, neurons 41 through 50 onto 61 through 70, neurons 61 through 70 onto 81 through 90, and neurons 81 through 90 onto 101 through 110. Simulation settings: L=20 s, λ=5 Hz, refractory period 1 ms, firing rates updated every 1 ms, random connections with 25% connectivity, strengths 0.0025 to 0.01, and delays 1 to 10 ms.

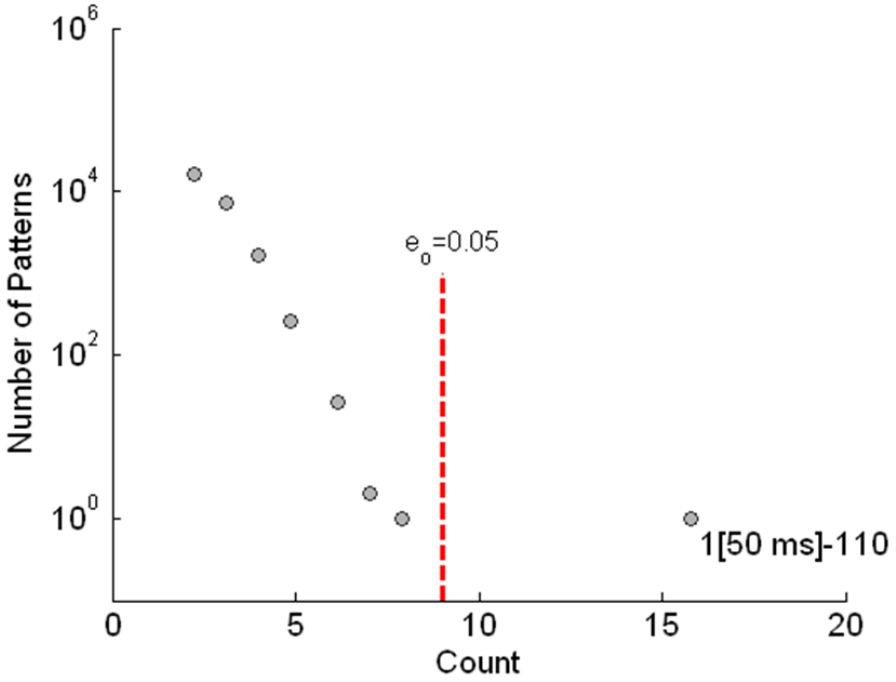

Figure 5.5: Patterns detected resulting from synfire chain. Out of the network shown in Fig. 5.4, imagine we have recorded from 52 of the neurons: neurons 11 through 20, 31 through 40, 51 through 60, 71 through 80, 91 through 100, and neurons 1 and 110. If we mine this data using the two-tape algorithm with a window size of 100 ms, we find that 1[50 ms]-110 is the strongest pattern even though there is not a direct connection between these two neurons. This demonstrates our method can detect precisely timed patterns resulting from network activity in addition to microcircuits.

(*Abeles and Gat*, 2001) is also based on the assumption that pattern counts are Poisson distributed, and significant 3-neuron patterns were detected as deviations from a smoothed version of a count matrix containing the triplet pattern counts for all delay combinations between 1 and 20 ms. We also considered three jitter-based methods: basic spike jitter (*Date et al.*, 1998), pattern jitter (*Harrison and Geman*, 2009), and NeuroXidence (*Pipa et al.*, 2008). With the parameters chosen, all four methods identified both *I-S-C* and *W-O-L* as significant (details on how each of these methods was implemented is given in Appendix B). The *Abeles and Gat* (2001) calculation, as well as spike jitter and pattern jitter, reported p-values of 0.000 for both patterns. NeuroXidence reported a p-value of 0.004 for *I-S-C* and 0.000 for *W-O-L*. Since the p-values are all close to zero for the two patterns with strong connections, these methods can not be used for comparing relative strengths of significant patterns. Using our method, if we choose e_0 corresponding to independence as the null hypothesis, then the p-values are 0.000 for both patterns as well. However, using our analytically derived expression for count threshold, we can determine the maximum value of e_0 for which the observed count will make the pattern significant. This e_0 value is 0.07 for *I-S-C* and 0.12 for *W-O-L*, giving a relative strength ratio for the two patterns of 1.7, which is close to 1.5, the ratio of the true conditional probabilities.

While we have demonstrated that the p-values for the significant patterns can not be used for rank ordering the strength of patterns, it may appear that the actual counts of the patterns themselves can be used for rank-ordering. This would not be proper if the firing rates of the first neurons in the patterns are different. In a simulation with the same pattern strengths as before but where neuron I fired nominally at 5 Hz and neuron W fired nominally at 1 Hz, the count of *I-S-C* was 19 and the count of *W-O-L* was 9, even though *W-O-L* has stronger synapses. In this situation, our method of ranking patterns based on the highest value of the parameter e_0 at which the observed count is significant still correctly ranks *W-O-L* (e_0=0.12)

ahead of I-S-C (e_0=0.09).

5.4 Discussion

In this chapter we presented a method for assessing significance of sequential firing patterns using correlation counts as the statistic. We represent the "strength of influence" of A on B by the conditional probability that B fires after a prescribed delay following A. We state our composite null hypothesis in terms of a parameter e_0 which is an upper bound on all such pair-wise conditional probabilities. There are two attractive features of this method. Firstly, we can rank order significant patterns in terms the highest value of e_0 at which the pattern (which repeats a certain number of times in the data) is still significant. The second interesting feature of the method is that we can now include many models of interdependent neurons in our null hypothesis (based on the value chosen for e_0). When we declare a pattern such as $A[T_1]$-$B[T_2]$-C to be significant, we can conclude that a spike by A has a "strong" chance of eliciting a spike from B with delay T_1 and a spike from C after a further delay of T_2. Here "strong" would denote that the relevant conditional probabilities can not be less than e_0. Thus, our idea of casting the null hypothesis in terms of a bound on conditional probabilities allows for a richer level of significance analysis compared to other methods, as we demonstrated through simulation experiments.

The method presented can assess significance of sequential firing patterns only when the underlying influences are excitatory. Using a similar null hypothesis with a lower bound on a conditional probability which is much smaller than the case under independence, it may be possible to find how low the correlation count should be for us to conclude that there are significant inhibitory influences.

We have given a simple test of significance based on the counts calculated through multi-point correlations. As mentioned earlier, the motivation is that such correlations are what are presently used for detecting such patterns. However, using correla-

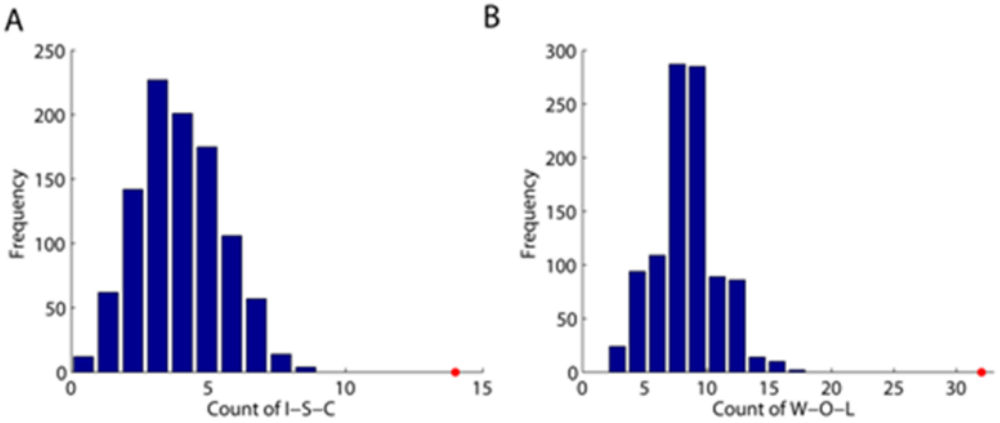

C

Method	P-value for excess of pattern I-S-C	W-O-L
Spike Jitter (Date et al, 1998)	0.000	0.000
Pattern Jitter (Harrison and Geman, 2008)	0.000	0.000
NeuroXidence (Pipa et al, 2008)	0.004	0.000
Smoothed Count Matrix (Abeles and Gat, 2001)	0.000	0.000
Null of Independence (e_0=0.005)	0.000	0.000
Max e_0 for which null is rejected (Type I error 0.05)	0.07	0.12

Figure 5.6: Comparison to other methods. Calculation of P-value for significance of patterns I-S-C (**A**) and W-O-L (**B**) using basic spike jitter. (**C**) P-values for the excess of patterns I[8]-S[4]-C and W-[6]-O[5]-L were calculated using various methods from the literature. Since the p-values are close to zero for both patterns, they cannot be used to assess the relative strength of the two patterns. Our method can rank order the strength of the patterns based on the maximum e_0 at which the pattern is still significant.

tion counts to detect interactions among a large group of neurons is computationally intensive. Since our test will directly give the threshold needed for the count, given any pattern, we do not need to actually obtain the true correlation count which would be required if we wanted to estimate the conditional probability. We only need to ascertain whether a pattern occurs more than some number of times, which leads to better computational efficiency. Further computational efficiency can be obtained by employing data mining algorithms for discovering patterns that count the non-overlapped occurrences of a pattern (*Patnaik et al.*, 2008; *Sastry and Unnikrishnan*, 2010), rather than all occurrences as the method presented in this chapter requires. We will develop statistical inference methods for counts based on these data mining algorithms in the next chapter.

CHAPTER VI

Inferring functional connectivity in neuronal networks using frequent episodes

6.1 Introduction

In the previous chapter, we developed a test of significance for sequential firing patterns in multi-neuronal spike trains based on counting all the occurrences of a pattern. Recently, an alternative method for detecting such patterns was introduced that counts a certain well-defined subset of the occurrences of a pattern, rather than all occurrences, in order to gain computational efficiency (*Patnaik et al.*, 2008; *Sastry and Unnikrishnan*, 2010). In this chapter, we develop a test of significance for patterns based on this type of count. We also introduce a heuristic method for determining from these patterns a graph representing the functional connectivity among the neurons. We demonstrate our methods on simulated neuronal networks as well as data from cultures of cortical neurons.

6.1.1 Frequent episode discovery of sequential firing patterns

In *Patnaik et al.* (2008) and *Sastry and Unnikrishnan* (2010), sequential firing patterns in multi-neuronal spike data are detected using frequent episode discovery, a popular framework in the field of temporal data mining (*Mannila et al.*, 1997). The

input data for frequent episode discovery is a sequence of events $\langle (E_1, t_1), (E_2, t_2), \ldots \rangle$, where E_i represents the event type and t_i is the time of the i^{th} event. The sequence is ordered so that $t_i \leq t_{i+1}$ for all i. In the context of multi-neuronal spike trains, the events are spikes, the event type is the label of the neuron that spiked (or the label of the electrode that recorded the spike), and the time stamps are the time of the spike. The following is an example event sequence consisting of 12 events with 5 different event types:

$$\begin{aligned} &\langle (A,1), (B,3), (A,5), (D,5), (C,6), (E,9), (A,10), \\ &(E,14), (B,15), (B,17), (C,18), (C,20) \rangle \end{aligned} \tag{6.1}$$

Temporal patterns in the event sequence are called *episodes*. A *serial episode* is an ordered tuple of event types, for example (A-B-C) is a serial episode with 3 event types (referred to as a 3-*node* serial episode). In the event sequence 6.1, the events $\langle (A,1), (B,3), (C,6) \rangle$ are an occurrence of the episode (A-B-C). The objective in frequent episode discovery is to detect all episodes whose *frequency* exceeds a user-specified threshold. The frequency of an episode can be defined in many different ways. Perhaps the most natural frequency measure for an episode would be the total number of occurrences, of which there are 15 in event sequence 6.1. Another possible frequency measure is the maximum number of *distinct* occurrences, where distinct occurrences are defined as occurrences which do not share any events. In event sequence 6.1, we have at most 3 distinct occurrences (for example, $\langle (A,1), (B,3), (C,6) \rangle$, $\langle (A,5), (B,15), (C,18) \rangle$, and $\langle (A,10), (B,17), (C,20) \rangle$). A third possibility, introduced in *Laxman et al.* (2005), is the maximum number of *non-overlapped* occurrences. Two occurrences are said to be non-overlapped if no event associated with one occurrence occurs in between the events associated with

the other. In event sequence 6.1, we have at most two non-overlapped occurrences (for example, $\langle (A,1),(B,3),(C,6)\rangle$, and $\langle (A,10),(B,15),(C,20)\rangle$). Regardless of the frequency measure chosen, the occurrences of serial episodes are typically detected using finite state automata (*Laxman et al.*, 2007). *Laxman et al.* (2007) shows that the non-overlapped frequency measure enables the use of more computationally efficient counting procedures than the other measures, and proposes an algorithm that can obtain the maximum number of non-overlapped occurrences using only 1 automaton per episode. In contrast, the number of automata needed per episode to obtain the total number of occurrences or the maximum number of distinct occurrences is in principle unbounded (*Laxman et al.*, 2007).

Patnaik et al. (2008) employed the non-overlapped frequency measure to detect patterns in spike data. An additional temporal constraint, motivated by the nature of neuronal communication, was also placed on the type of patterns detected (*Patnaik et al.*, 2008). When considering the frequency of an episode, only occurrences which satisfied a user-specified *inter-event interval constraint* were counted. This constraint requires that the difference between the times of every pair of successive events in an occurrence of serial episode be within an interval of the form $[T_{low}, T_{high}]$. For example, suppose the interval of interest is [4,6] and we are counting non-overlapped occurrences of the 3-node serial episode (A[4,6]-B[4,6]-C). In event sequence 6.1, we have just 1 occurrence: $\langle (A,10),(B,15),(C,20)\rangle$. The inter-event constraint can be generalized so that different time intervals are applied for different pairs of events within a serial episode. *Patnaik et al.* (2008) presents an efficient algorithm for discovering all serial episodes with inter-event interval constraints, which we refer to as sequential patterns.

Sequential firing patterns are useful for unearthing the functional connectivity between neurons because they can account for the delays inherent in synaptic communication. For example, suppose there is a single synapse mediating communication from neuron A to neuron B. In such a scenario, spikes from A will have an effect

on the probability of B spiking, but only after some time delay due to the chemical processes involved in synaptic transmission. The delay can vary depending on the type of neurotransmitter acting at the synapse. For example, AMPA synapses are typically fast-acting with delays of 5 ms or less, while the action of $GABA_B$ synapses can be as slow as 250 ms (*Destexhe and Sejnowski*, 2001).

6.1.2 Statistical significance of sequential patterns

While *Patnaik et al.* (2008) detailed an algorithm for detecting sequential patterns that repeat frequently (i.e. above a user-specified threshold), it did not present any statistical theory for determining when these patterns are repeating more often than one would expect by chance. This issue was taken up in *Sastry and Unnikrishnan* (2010) by constructing a probabilistic model to represent the counting algorithm. Recurrence relations were then derived to solve for the first two moments of the non-overlapped count for an episode, and a bound on the probability of the non-overlapped count for that episode exceeding some value was obtained using the Chebyshev inequality. This bound was then used to test for the statistical significance of the episode. In this chapter, we improve on the *Sastry and Unnikrishnan* (2010) results by developing a model which allows us to obtain closed-form expressions for the first two moments of the non-overlapped count. We also explore methods of obtaining tighter bounds than those given in *Sastry and Unnikrishnan* (2010).

6.2 Methodology

6.2.1 Distribution of the total number of occurrences of a serial episode

In the previous chapter, we worked with a model where the total number of occurrences of a serial episode were Poisson-distributed. That model was based on the assumption that the firing of the first neuron in an episode was *stationary*, and

followed a homogeneous Poisson process with rate λ. In this chapter, for convenience we will instead work with the discrete-time counterpart of a Poisson process, the Bernoulli process. We discretize time into bins of fixed size Δ, where Δ is small enough so that there is at most one spike per neuron in an interval. We observe the firing of a group of J neurons over a time period consisting of L intervals, and assume for now that the neurons are firing independently. For each neuron we have a Bernoulli process $X_j(t)$, $t = 1, \ldots, L$, $j = 1, \ldots, J$ representing whether or not neuron j fires in interval t. Let P_j be the probability of firing in an interval $(= 1 - exp(-\lambda_j \Delta))$ and denote the number of firings during L intervals as N_j for neurons $j = 1, \ldots, J$. Then the N_j's are independent binomial(L, P_j) random variables.

We will now consider the case when we have dependence among neurons. Suppose we have two neurons A and B with one-directional dependence: A influences B, but B does not influence A (written as $A \to B$), and that there is a delay of T time units between the time A fires and when it affects the probability of B firing ($A \xrightarrow{T} B$). Since the firing of A is unaffected by B, its firings are *iid* Bernoulli random variables with success probability P_A. The firing of neuron B is due to a mixture of two processes; it can fire on its own or due to excitation by A. Since each of these processes are independent over time, the firing of B across different intervals remains independent. The mixture probability of B firing in any interval t is:

$$
\begin{aligned}
P(X_B(t) = 1) = & \\
& P(X_B(t) = 1 | X_A(t - T) = 1) P(X_A(t - T) = 1) \\
& + P(X_B(t) = 1 | X_A(t - T) = 0) P(X_A(t - T) = 0) \\
& = P_A P_{B|A} + (1 - P_A) P_{B|\bar{A}} \qquad (6.2) \\
P(X_B(t) = 0) = 1 - P(X_B(t) = 1) & \qquad (6.3)
\end{aligned}
$$

Thus, B is marginally a Bernoulli process with $P_B^c = P_A\ P_{B|A} + (1-P_A)\ P_{B|\bar{A}}$, where the superscript c stands for combined. This result extends to chains of multiple neurons (e.g. B and C are both still marginally Bernoulli processes if we have a structure like $A \rightarrow B \rightarrow C$), or other feed-forward structures (e.g. B and C are both still marginally Bernoulli if we have a structure like $A \rightarrow B$ and $A \rightarrow C$), as long as there are no loops or cycles. In other words, our approach is valid if the network structure is a directed acyclic graph.

We will have an occurrence of the serial episode (A-B) with inter-event time constraint T, written as $A[T] - B$, if a firing of A is followed by a firing of B after T time units. Consider the binary process $I_E(t)$ that equals 1 if $X_A(t) = 1 \cap X_B(t+T) = 1$, for $t = 1, \ldots, L-T$. This is an iid Bernoulli process with success probability $P_E = P_A P_{B|A}$. Thus the total number of occurrences of the episode $A[T] - B$ during L intervals, denoted N, has a binomial distribution with parameters $(L-T)$ and P_E. The expected value and variance of N are:

$$E[N] = (L-T)P_E \tag{6.4}$$

$$Var[N] = (L-T)P_E(1-P_E) \tag{6.5}$$

6.2.2 Distribution of the number of non-overlapped occurrences of a serial episode

We have that the total number of occurrences N (of a serial episode E with a time delay of T in data of length L) is distributed binomial$(L-T,\ P_E)$. We are interested in the distribution of the number of non-overlapped occurrences of the episode, which we denote M. We note that $M \leq N$, and partition N as follows: consider the j^{th} non-overlapped occurrence of E, and let R_j be the total number of occurrences of E that occur between the $(j-1)^{th}$ and j^{th} non-overlapped occurrence.

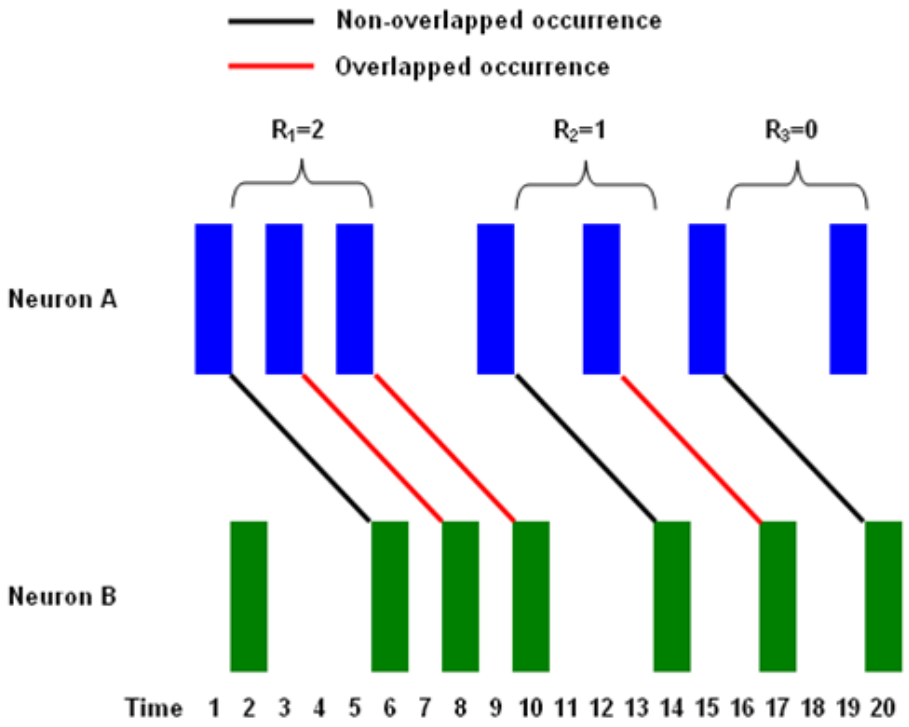

Figure 6.1: Illustration of occurrences for example episode $A[5]-B$. The total number of occurrences in $L = 20$ bins is $N = 6$, consisting of $M = 3$ non-overlapped occurrences and $R_1 + R_2 + R_3 = 3$ overlapped occurrences.

Proposition: N has the same distribution as

$$N = M + \sum_{j=1}^{M} R_j. \tag{6.6}$$

where the R_js are iid binomial(k, P_E) random variables and are independent of M. Figure 6.1 illustrates the partitioning of N into M and R.

We can readily compute the expected value and variance of M. Taking expectations of both sides of Equation 6.6, we have:

$$\begin{aligned} E[N] &= E[M] + E[\sum_{j=1}^{M} R_j] \\ &= E[M] + E[M]E[R_1] \quad \text{(by independence of M and R)} \end{aligned}$$

and rearranging terms gives:

$$E[M] = \frac{E[N]}{1 + E[R_1} = \frac{L - T}{1/P_E + k} \tag{6.7}$$

Taking the variance of both sides of Equation 6.6, we have:

$$Var[N] = Var[M] + Var[\sum_{j=1}^{M} R_j] + 2Cov[M, \sum_{j=1}^{M} R_j] \tag{6.8}$$

using the Law of Total Variance, we can write the $Var[\sum_{j=1}^{M} R_j]$ term from the RHS of Equation 6.8 as:

$$\begin{aligned} Var[\sum_{j=1}^{M} R_j] &= E[Var[\sum_{j=1}^{M} R_j|M]] + Var[E[\sum_{j=1}^{M} R_j|M]] \\ &= E[MVar[R_1]] + Var[ME[R_1]] \\ &= Var[R_1]E[M] + E[R_1]^2 Var[M] \end{aligned}$$

and writing the $2Cov[M, \sum_{j=1}^{M} R_j]$ term from the RHS of Equation 6.8 as:

$$\begin{aligned} 2Cov[M, \sum_{j=1}^{M} R_j] &= 2(E[M \sum_{j=1}^{M} R_j] - E[M]E[\sum_{j=1}^{M} R_j] \\ &= 2(E[M^2]E[R_1] - E[M]^2 E[R_1] \\ &= 2E[R_1]Var[M] \end{aligned}$$

gives:

$$\begin{aligned} Var[N] &= Var[M] + Var[R_1]E[M] + E[R_1]^2 Var[M] + 2E[R_1]Var[M] \\ &= Var[M](1 + 2E[R_1] + E[R_1]^2) + Var[R_1]E[M] \end{aligned}$$

We can now solve for Var[M] by rearranging terms:

$$\begin{aligned} Var[M] &= \frac{Var[N] - Var[R_1]E[M]}{1 + 2E[R_1] + E[R_1]^2} \\ &= \frac{(L-T)P_E(1-P_E)}{(1+TP_E)(1+2TP_E+T^2P_E^2)} \\ &= \frac{Var[N]}{(1+TP_E)^3} \end{aligned} \tag{6.9}$$

The closed-form expressions for the mean and variance of M derived here agree with the mean and variance of M based on the recurrence relations derived in *Sastry and Unnikrishnan* (2010). In both approaches, the moments depend on the three parameters L, T, and P_E. Table 6.1 shows a comparison of the values obtained by the two approaches for several parameter settings.

In *Sastry and Unnikrishnan* (2010), the mean and variance of M are then used to get a bound on the probability that M will exceed some value based on the Chebyhshev inequality. The Chebyshev inequality guarantees that for any arbitrary distribution, no more than $1/k^2$ of the distribution's values are more than k standard deviations away from the mean:

$$Pr(|X - \mu| \geq k\sigma) \leq \frac{1}{k^2} \tag{6.10}$$

where X is a random variable with expected value μ and finite variance σ^2. For example, suppose we have L=300000, T=500, and P_E=0.001 as in the last row of

L	T	P_E	Closed-form expressions E[M]	Var[M]	Recurrence relations E[M]	Var[M]
20000	5	0.000025	0.5	0.5	0.5	0.5
		0.0005	10.0	9.9	10.0	9.9
		0.001	19.9	19.7	19.9	19.7
20000	50	0.000025	0.5	0.5	0.5	0.5
		0.0005	9.7	9.3	9.7	9.3
		0.001	19.0	17.2	19.0	17.3
20000	500	0.000025	0.5	0.5	0.5	0.5
		0.0005	7.8	5.0	7.8	5.0
		0.001	13.0	5.8	13.0	5.9
60000	5	0.000025	1.5	1.5	1.5	1.5
		0.0005	29.9	29.8	29.9	29.8
		0.001	59.7	59.0	59.8	59.2
60000	50	0.000025	1.5	1.5	1.5	1.5
		0.0005	29.2	27.8	29.3	27.9
		0.001	57.1	51.7	57.2	51.9
60000	500	0.000025	1.5	1.4	1.5	1.4
		0.0005	23.8	15.2	23.8	15.3
		0.001	39.7	17.6	39.7	17.7
300000	5	0.000025	7.5	7.5	7.5	7.5
		0.0005	149.6	148.8	149.7	149
		0.001	298.5	295.2	298.8	296.1
300000	50	0.000025	7.5	7.5	7.5	7.5
		0.0005	146.3	139.2	146.4	139.4
		0.001	285.7	258.5	285.9	259.6
300000	500	0.000025	7.4	7.2	7.4	7.2
		0.0005	119.8	76.6	119.9	76.7
		0.001	199.7	88.7	199.9	88.9

Table 6.1: Mean and variance of the number of non-overlapped occurrences of an episode based on the closed-form expressions derived here and the recurrence relations derived in *Sastry and Unnikrishnan* (2010)

Table 6.1. Then M is a random variable with μ=200 and σ=9.4. If we observe M many times, the Chebyshev inequality with k=4.47 gives that 95% of the time M will be between 158.0 and 242.0. However, because this bound is distribution-independent it can be very conservative. To see how conservative the bound is in this case, we used simulation to generate many observations of M with these parameter settings. The simulation procedure was as follows:

```
initialize t = 1, M = 0
while t ≤ L − T do
  Draw random number r between 0 and 1
  if r < P_E then
    M = M + 1
    t = t + T
  else
    t = t + 1
  end if
end while
```

Using the above algorithm, we simulated 10,000 replications of M for L=300000, T=500, and P_E=0.001. We found that M was between the Chebyshev bounds in 100% of the simulations. Based on the simulation results, we can use an interval of 181 to 218 to bound 95% of the values. This bound is 56% tighter than the corresponding Chebyshev bound, as shown in Figure 6.2.

6.2.3 Inferring connection strengths

The usefulness of having a model for the number of non-overlapping occurrences of an episode is that it allows us to go from the count of that episode to an estimate of the strength of the connection between the neurons involved in the episode. Given a count M for an episode with span T in data of length L, we can invert Equation 6.7 to solve for the probability of that episode occurring at any instant:

$$\hat{P}_E = \left(\frac{L-T}{M} - T \right)^{-1} \tag{6.11}$$

Suppose the episode of interest is A[T]-B, then the probability of occurrence is $P_E = P(B|A) \times P_A$. We can use $\hat{P}_E$ and an estimate of P_A from the data ($\hat{P}_A = N_A/L$) to get $\hat{P}_{B|A}$. This conditional probability, denoted $e(B|A,T)$ in the previous chapter and $e_s(A,B,T)$ in *Sastry and Unnikrishnan* (2010), is a useful measure of the strength of the interaction between A and B. For example, say we have obtained the non-overlapped count of two episodes, $M_{A[500]-B} = 200$ and $M_{C[500]-B} = 250$, in data of

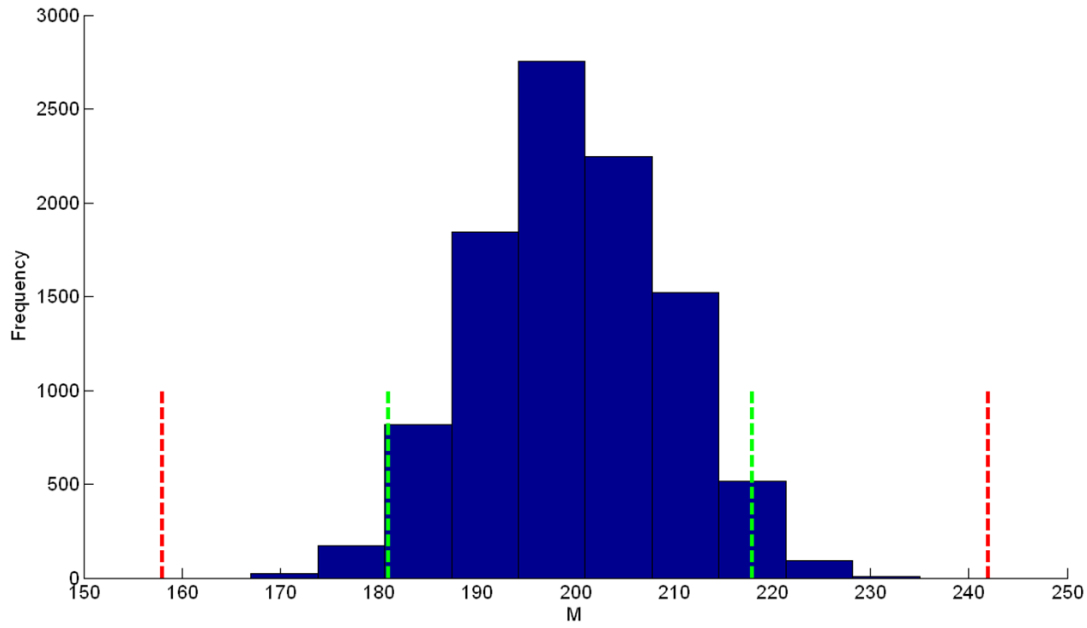

Figure 6.2: Histogram of M for 10,000 simulation replications with L=300000, T=500, and P_E=0.001. The 95% bounds based on simulation (green lines, M=[181, 218]) are much tighter than the 95% Chebyshev bounds (red lines, M=[158, 242]).

length L=300000. Our estimate of P_E for these two episodes would be 0.001 and 0.0014 respectively. Assuming that both A and C spike at a rate of 5 Hz, then we have $\hat{P}_{B|A} = 0.20$ and $\hat{P}_{B|C} = 0.28$, which indicates that the connection from C to B is stronger than the connection from A to B. However, because the firing rate of B does not enter into these calculations there can be situations where the conditional probability does not tell the whole story. For example, suppose in the same spike train we also counted another episode, $M_{C[500]-D} = 150$. This would give $\hat{P}_E = 0.00067$ and $\hat{P}_{D|C} = 0.13$, leading to the conclusion that the connection from C to B is stronger than the connection from C to D. This conclusion may be incorrect though if the firing rate of B is much higher than that of D. Suppose the firing rate of B on its own is 20 Hz, then P_B=0.02. The $\hat{P}_{B|C}$ we obtained earlier is 14 times greater than P_B. If the firing rate of D on its own is 5 Hz, then P_D=0.005. The $\hat{P}_{D|C}$ we obtained earlier is 26 times greater than P_D, indicating that the C to D

connection is actually stronger than the C to B connection. This illustrates that the firing rate of both neurons involved in the episode should be taken into account when drawing conclusions about the strength of the connection between them. We define the strength ratio $s = P_{Y|X}/P(Y)$. If X and Y are independent, then $s = 1$. We can use s in a data-mining context to find strong connections the same way that e_0 was used in the previous chapter. Let s_0 be a user-defined threshold that is bigger than one. We say that the excitatory influence of X on Y is "strong" if $s > s_0$.

In the same way that we use Equation 6.11 to obtain $\hat{P}_E$ from the count M, if we have a confidence interval for M we can invert it to get a confidence interval (CI) for $\hat{P}_E$. A straightforward way of getting a CI for M is through simulation. Continuing with our previous example, say we have an episode $A[500] - B$ with a count of 200 and $\hat{P}_E$=0.001. Using Algorithm 6.2.2, we simulate 10,000 replications of M with $L = 300000$, $T = 500$, and $P_E = 0.001$ and find a 95% CI for M of [181, 218] as shown in Figure 6.2. Inverting this interval using Equation 6.11 gives a 95% CI for $\hat{P}_E$ of [0.00087, 0.0011]. This leads to a 95% CI for $\hat{s}$ of [34.8, 44]. Since the lower confidence limit for $\hat{s}$ is greater than 1, we conclude there is a statistically significant excitatory connection $A \overset{500}{\rightarrow} B$. Unfortunately, obtaining a CI for M through simulation is too slow to be a practical approach in a typical data analysis situation. On a dual-core Pentium machine with a 1.66 GHz processor and 2 GB RAM, simulating 1,000 replications of M with Algorithm 6.2.2 coded in MATLAB® for parameter settings corresponding to Figure 6.2 takes approximately 10 seconds. Since multi-electrode arrays can have 500 or more recording electrodes, determining the statistical significance of each episode needs to be extremely fast as the number of different episodes to be evaluated is likely to be in the thousands. Thus, we examined the appropriateness of using a normal approximation to M for episode $A[500] - B$. We generated 10,000 normal random variables with mean of 199.7 and standard deviation of 9.4, based on the mean and variance expressions for our $\hat{P}_E$. We then

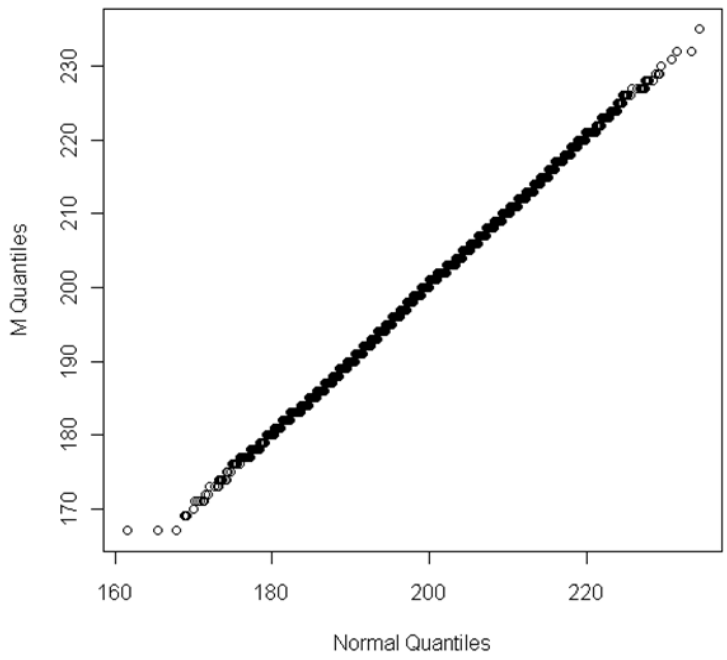

Figure 6.3: QQ plot comparing the distribution of M obtained from simulation to a normal distribution. On the y-axis are the quantiles of 10,000 simulation replications of M with $L = 300000$, $T = 500$, and $P_E = 0.001$. On the x-axis are 10,000 normal random variables with mean and standard deviation corresponding to these parameter settings. The plot is linear except at the extreme tails, indicating that the distribution of M is approximately normal for these parameter settings.

constructed a quantile-quantile (QQ) plot to compare these normal random variables to our simulation replications for M. The QQ plot in Figure 6.3 is linear, indicating that a normal distribution is a good approximation for the distribution of M in this case.

A 95% CI for M based on the normal approximation can be obtained easily as $[\mu - 1.96\sigma, \mu + 1.96\sigma]$, which gives [181.3, 218.1] in this case. This is very close to the 95% CI obtained through simulation, and indeed Table 6.2 shows that the normal-based CI is close to the simulation-based CI for most of the parameter settings we considered in Table 6.1. The exception is when the expected counts are very low, such as in the first row of Table 6.1. Here the normal-based lower confidence limit is a negative value, which is inappropriate since the distribution of M, being a count, is

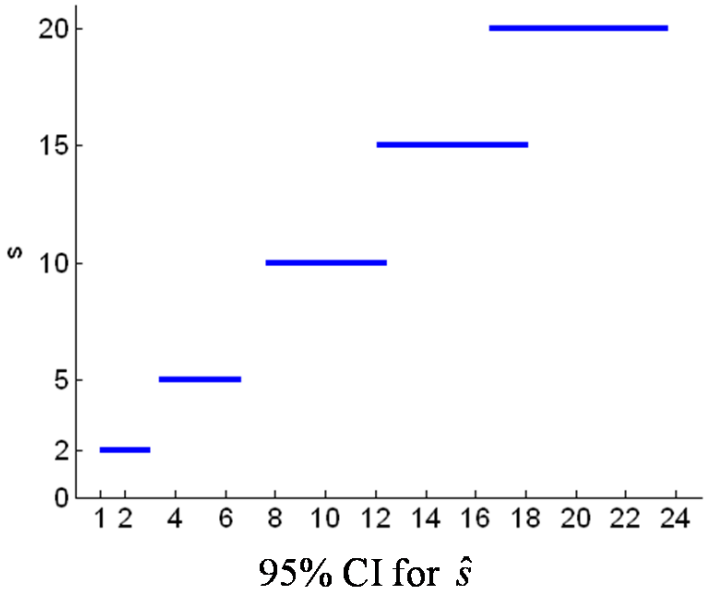

Figure 6.4: 95% CI for $\hat{s}$ based on normal approximation for several strengths s. When $s = 2$, the CI for $\hat{s}$ does not include 1. This is the weakest connection strength for which the connection strength is statistically significant (compared to independence) with these parameter settings. The CI for $\hat{s}$ with $s = 5$ does not overlap with the CI for $s = 2$, so we can resolve these two connection strengths. As the strength increases, more separation between s values is required to resolve the strengths.

non-negative. However the normal-based upper confidence limits do appear to match the simulation upper confidence limits even when the expected counts are low. Thus, for statistical inference in this chapter we will use normal-based CIs, and set the lower confidence limit to 0 if it happens to be negative.[1] In Figure 6.4, we show examples of using our normal-based approximation to infer connection strengths.

[1] Although a normal approximation for M appears to be valid for wide range of parameter settings, in some situations it may be desirable to perform statistical inference using a better approximation for the distribution of M. In other work, we have accomplished this by first obtaining the moment generating function (MGF) of M based on Equation 6.6 (*Diekman et al.*, In Preparation). We can then use the MGF to obtain the first 4 moments of the distribution of M, and then approximate this distribution very closely using a polynomial function of a normal random variable that matches these first 4 moments (*Diekman et al.*, In Preparation).

L	T	P_E	Simulation Quantiles 0.025	0.975	Normal Quantiles 0.025	0.975
20000	5	0.000025	0	2	-0.9	1.9
		0.0005	4	17	3.8	16.1
		0.001	12	29	11.2	28.6
20000	50	0.000025	0	2	-0.9	1.9
		0.0005	4	16	3.8	15.7
		0.001	11	28	10.9	27.1
20000	500	0.000025	0	2	-0.9	1.8
		0.0005	4	12	3.4	12.2
		0.001	8	18	8.3	17.7
60000	5	0.000025	0	4	-0.9	3.9
		0.0005	20	41	19.2	40.6
		0.001	45	75	44.6	74.8
60000	50	0.000025	0	4	-0.9	3.9
		0.0005	20	40	18.9	39.6
		0.001	43	72	43.0	71.2
60000	500	0.000025	0	4	-0.9	3.8
		0.0005	16	32	16.2	31.4
		0.001	32	48	31.4	47.9
300000	5	0.000025	3	13	2.1	12.9
		0.0005	127	174	125.7	173.5
		0.001	266	334	264.8	332.2
300000	50	0.000025	3	13	2.1	12.8
		0.0005	124	170	123.2	169.4
		0.001	255	318	254.1	317.2
300000	500	0.000025	3	13	2.1	12.7
		0.0005	103	137	102.6	137.0
		0.001	181	218	181.2	218.1

Table 6.2: Comparison of 95% confidence intervals for M based on simulation and the corresponding normal approximation for a variety of parameter settings. As long as the CI does not include 0, the normal approximation seems to be reasonable.

6.3 Results

6.3.1 Simulated neuronal networks

To test the ability of our methods to detect functional connections between neurons, we applied them to spike data generated by a simulated neuronal network. We

simulated a network of 25 neurons, with each neuron i ($i = 1, \ldots, 25$) firing independently as a Bernoulli process with a success probability of $P_i(t)$=0.005 in each discrete time bin t ($t = 1, \ldots, L$). We chose a bin size of $\Delta = 1$ ms, giving each neuron a baseline firing rate of 5 Hz. We then embedded a certain number of strong connections among the neurons. For the first set of simulations, for each neuron i we randomly chose one other neuron j ($i \neq j$) as the post-synaptic target. This connection was then randomly assigned a delay k between 1 and 10 ms. If neuron i spikes at time t, then the spiking probability of its post-synaptic target j is elevated in the $(t+k)^{th}$ time bin, so that $P_j(t+k) > 0.005$ (for the first simulation we set $P_j(t+k) = 0.2$). Different neurons may have the same post-synaptic target, so it is possible for a neuron j to be receiving an excitatory signal from multiple pre-synaptic neurons in a single time bin, elevating $P_j(t+k)$ above 0.2.

We generated 300 seconds of spike data from this type of network, and then counted the number of non-overlapped occurrences for all possible 2-node episodes (625 different neuron pairs), with delays T ranging from 1 to 500 ms. For each episode counted (312,500 in all), we obtained a 95% CI for $\hat{s}$. We then classified any episode which had a lower confidence limit for $\hat{s}$ greater than 1 as representing a connection between those neurons with delay T. For the simulated network we know the ground truth, that there are 25 true connections. Our procedure identified 224 connections, including all 25 true connections so the sensitivity of the test (also known as recall) was 1.[2] Despite 199 false positives, the specificity of the test was nearly 1 because the number of true negatives is far greater than the number of true positives. Therefore, instead of specificity, we calculated the precision of the test, which comes out to just 0.11. Precision and recall can be combined into a single measure of the performance

[2]Sensitivity is the proportion of actual positives which are correctly identified as such, or *true positives/(true positives + false negatives)*. Specificity is the proportion of actual negatives which are correctly identified as such, or *true negatives/(true negatives + false positives)*. Precision is the proportion of returned positives that are true positives, or *true positives/(true positives + false positives)*.

of the test, called the F-measure (*van Rijsbergen*, 1979):

$$F = 2 \times \frac{\text{precision} \times \text{recall}}{\text{precision} + \text{recall}} \tag{6.12}$$

For this test we get $F = 0.20$. Instead of classifying episodes with a lower confidence limit for $\hat{s}$ greater than 1 as connections (i.e. $s_0 = 1$), we can make the criteria more strict so that only episodes with a lower confidence limit for $\hat{s}$ greater than 2 are classified as connections (i.e. $s_0 = 2$). This test still has perfect recall, and higher precision (0.63) so a higher F (0.77). With $s_0 = 3$, the test again has perfect recall and higher precision (0.93), so a higher F (0.96). With $s_0 = 4$, the test has perfect recall and precision, so F=1. Figure 6.5 compares the true connectivity graph and the inferred graphs at the different s_0 thresholds.

We can continue to increase s_0 up to 10 and maintain perfect performance of the test (F=1), but beyond $s_0 = 10$ we start to have some false negatives and so no longer have perfect recall as shown in Figure 6.6.

6.3.1.1 False edge elimination

For Simulation #1, with $s_0 = 3$ we had two false positives: connections $4[13] - 20$ and $5[276] - 11$. In Table 6.3, which lists the true connections for this simulation, we see that $4 \rightarrow 6$ with a delay of 6 and $6 \rightarrow 20$ with a delay of 7 are both true connections. This could explain why $4[13] - 20$ shows up as significant– not because of a direct connection $4 \rightarrow 20$, but because of two indirect connections $4 \stackrel{6}{\rightarrow} 6 \stackrel{7}{\rightarrow} 20$ whose delays add up to 13. In fact, there are other possible relationships among 3 neurons, besides a chain such as $A \rightarrow B \rightarrow C$, that could also lead to false positives when only 2-node episodes are considered. For example, suppose we had the following connections: $A \stackrel{T_1}{\rightarrow} B$ and $A \stackrel{T_2}{\rightarrow} C$, where $T_2 > T_1$. Not only would this likely lead to the 2-node episodes $A[T_1] - B$ and $A[T_2] - C$ being frequent, but potentially $B[T_3] - C$ (where $T_3 = T_2 - T_1$) as well. In this case $A[T_1] - B$ and $A[T_2] - C$ would be true

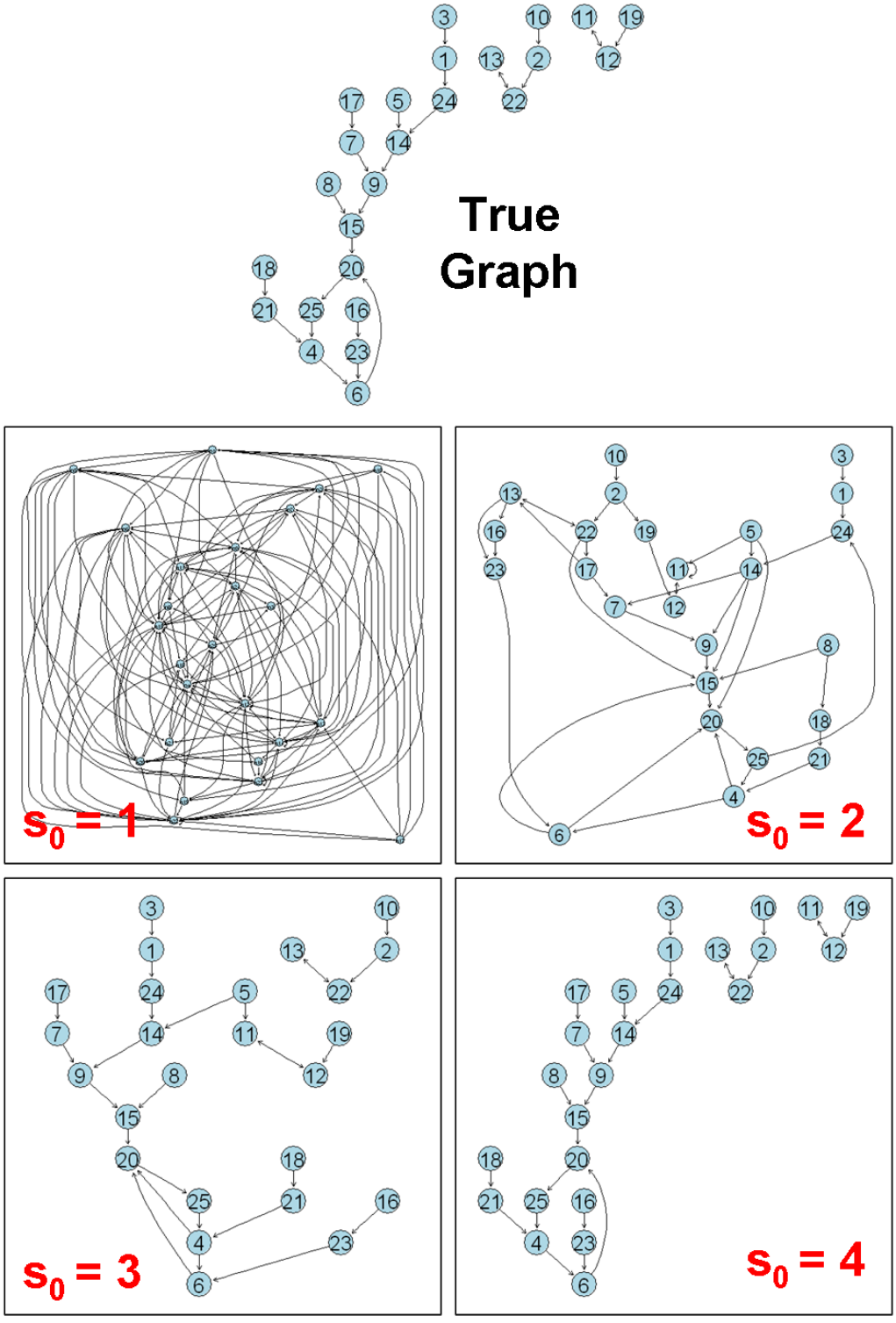

Figure 6.5: For Simulation #1, the inferred connectivity graph with $s_0 = 4$ is identical to the true graph.

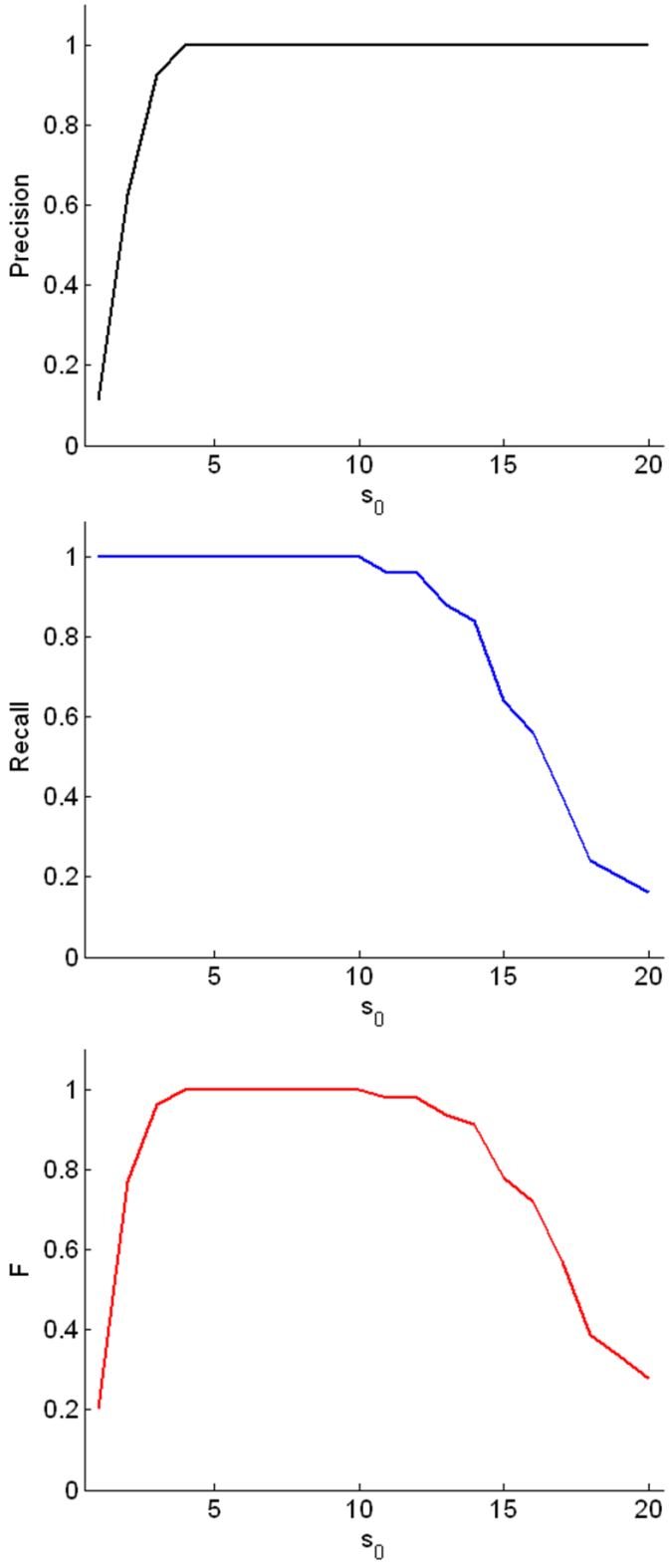

Figure 6.6: For Simulation #1, the test has perfect precision and recall for $s_0 = 4$ through $s_0 = 10$.

positives, but $B[T_3] - C$ would be a false positive.

$i \to j$	k
$1 \to 24$	10
$2 \to 22$	9
$3 \to 1$	9
$4 \to 6$	6
$5 \to 14$	1
$6 \to 20$	7
$7 \to 9$	5
$8 \to 15$	4
$9 \to 15$	6
$10 \to 2$	2
$11 \to 12$	6
$12 \to 11$	3
$13 \to 22$	10
$14 \to 9$	8
$15 \to 20$	3
$16 \to 23$	3
$17 \to 7$	6
$18 \to 21$	7
$19 \to 12$	1
$20 \to 25$	5
$21 \to 4$	1
$22 \to 13$	2
$23 \to 6$	6
$24 \to 14$	9
$25 \to 4$	3

Table 6.3: True connections for Simulation #1.

In general, there are 4 possible feed-feedforward structures involving 3 neurons as shown in Figure 6.7. A chain of 3 neurons, which we refer to as an α-type structure, is likely to produce the false positive $A[T_1 + T_2] - C$. A β-type structure is likely to produce the false positive $B[T_2] - C$. The γ-type structure is not likely to produce any false positives, as $A[T_1] - B$, $B[T_2] - C$, and $A[T_1 + T_2] - C$ would all be true positives if returned. The δ-type structure is also not likely to produce any false positives, as there is no reason to expect that $A[T_1] - B$ would be returned as a positive.

Suppose we analyze a dataset at the 2-node level and find that $A[T_1] - B$, $B[T_2] - C$, and $A[T_1 + T_2] - C$ are all significant. How can we determine which of the 3-

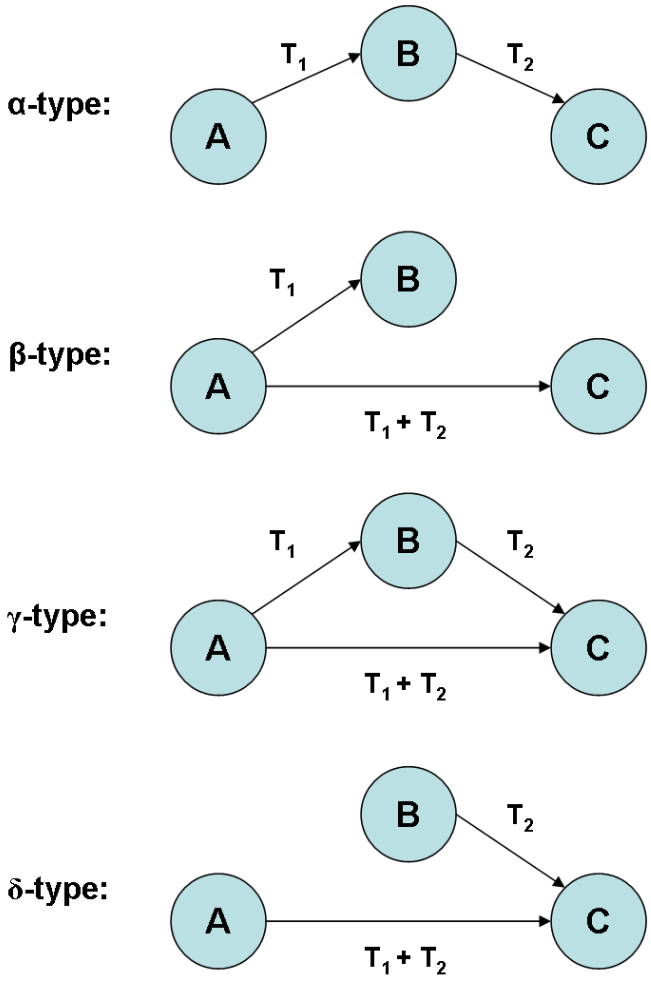

Figure 6.7: The 4 possible feed-forward structures involving 3 neurons. α-type, β-type, and γ-type structures are all likely to lead to the same set of frequent 2-node episodes: $A[T_1] - B$, $B[T_2] - C$, and $A[T_1 + T_2] - C$. The δ-type structure is likely to lead to $A[T_1 + T_2] - C$ and $B[T_2] - C$ being frequent but not $A[T_1] - B$.

neuron structures is most likely to have produced the data? We propose the following heuristic method. First, we count the occurrences of the 3-node episode $A[T_1]-B[T_2]-C$, which we denote as M_{ABC}. (Likewise, we denoted the counts of $B[T_2]-C$ and $A[T_1+T_2]-C$ as M_{BC} and M_{AC} respectively). We then obtain adjusted 2-node counts $M_{BC'}$ and $M_{AC'}$ by subtracting the 3-node count from the original 2-node counts: $M_{BC'} = M_{BC} - M_{ABC}$ and $M_{AC'} = M_{AC} - M_{ABC}$. $M_{BC'}$ represents the number of occurrences of $B[T_2]-C$ where an A did *not* occur T_1 time units before the B, and $M_{AC'}$ represents occurrences of $A[T_1+T_2]-C$ where a B did *not* occur T_1 (T_2) time units after (before) the A (C). We map each of the adjusted 2-node counts to a $P_{E'}$, and compute the following adjusted ratios:

$$s_{BC'} = \frac{P_{E:BC'}}{(1-P_A)P_BP_C} \tag{6.13}$$

$$s_{AC'} = \frac{P_{E:AC'}}{P_A(1-P_B)P_C} \tag{6.14}$$

We then compare the lower confidence limit of s' to s_0 to determine if the connection is significant. For example, the count of $4[13]-20$ in our first simulation, $M_{4[13]-20}$, was 9. This maps to $\hat{P}_{E:4[13]-20} = 0.000453$, and ultimately a 95% CI for $\hat{s}_{4[13]-20}$ of [3.2, 15.3], which is significant for $s_0 = 3$. The count of the 3-node episode $4[6]-6[7]-20$ is 6, so the adjusted 2-node count $M_{4[13]-20'} = 3$. This maps to $\hat{P}_{E:4[13]-20'} = 0.000150$, and the lower 95% confidence limit for $\hat{s}_{4[13]-20'}$ is less than 3, so the connection is no longer significant for $s_0 = 3$. Thus, information about a 3-node episode has led us to determine that a connection which appeared significant at the 2-node level is not actually a true connection. We refer to this procedure as pruning or false edge elimination.

Since information about 3-node episodes can be useful in eliminating false edges, we would like to obtain all the relevant 3-node episode counts. However the com-

binatorial explosion of the number of episodes begins to be a consideration, as even with just 25 neurons there are 15,000 different 3-neuron combinations, and so for $T = 1, \ldots, 500$ there are over 7 million episodes to be counted. Instead of counting all possible 3-node episodes, we will count a subset of them using a level-wise candidate generation scheme. In level-wise procedures, such as the *Apriori* algorithm of *Agrawal et al.* (1993), candidate generation for the $(n+1)^{th}$ level takes the set of frequent episodes of size n and combines them in different ways to obtain a set of candidate episodes of size $n+1$. We will generate the 3-node candidates to be counted based on the 2-node episodes that were found to be significant using the following scheme described in *Patnaik et al.* (2008) for candidate generation with intervent time constraints. Let α and β be two 2-node significant episodes, where the second node of α is the same as the first node of β. A candidate 3-node episode γ is created by appending to α the inter-event delay and last node of β. For example, in our first simulation we had a set of 40 significant 2-node episodes with $s_0 = 2$, which results in a set of 310 candidate 3-node episodes. After counting the occurrences of these 3-node episodes, we now want to use these counts to eliminate false edges at the 2-node level. If we have counted the 3-node episode $A[T_1] - B[T_2] - C$, it is possible that the true network structure is α-type (see Figure 6.7) and therefore at the 2-node level $A[T_1 + T_2] - C$ was a false edge. It is also possible that the true network structure is β-type and that $B[T_2] - C$ was a false edge, or that the true network structure is γ-type and that neither $A[T_1 + T_2] - C$ nor $B[T_2] - C$ were false edges.[3] Thus we go to our set of significant 2-node episodes, and if any of them match $A[T_1 + T_2] - C$ or $B[T_2] - C$, we subtract M_{ABC} from their counts and determine if M'_{AC} or M'_{BC} are significant with $s_0 = 2$. If not, we conclude that $A[T_1 + T_2] - C$ or $B[T_2] - C$ was a false edge and remove it from our list of significant 2-node episodes.

[3]If we have counted the 3-node episode $A[T_1] - B[T_2] - C$, it is not likely that the true network structure is δ-type, as there is no reason to expect that $A[T_1] - B$ would be found significant if that were the case.

In our first simulation, we would not necessarily expect any false $B[T_2]-C$ edges, because we limited each neuron to just 1 post-synaptic target making a true *beta*-type structure impossible. However, with $s_0 = 2$ we do find 3 false $A[T_1+T_2]-C$ edges. In addition to $4[13]-20$ which we discussed previously, $14[14]-15$ and $11[9]-11$ were also found to be false edges. Indeed, inspection of Table 6.3 confirms that $14[14]-15$ is not a true connection, and rather its significance at the 2-node level was just due to occurrences of $14[8]-9$ followed by occurrences of $9[6]-15$. Likewise, $11[9]-11$ is not a true connection but was significant due to occurrences of $11[6]-12$ followed by $12[3]-11$.[4] Removing these 3 false edges raises our precision with $s_0 = 2$ from 0.63 to 0.68.

For our second simulation, we increased the number of post-synaptic targets per neuron to two, for a total of 50 true connections. We again simulated 20 seconds of data, counted all 2-node episodes, determined significant connections at the 2-node level, generated and counted candidate 3-node episodes, and used their counts to prune false edges. We repeated this procedure for simulations with 3 post-synaptic targets per neuron (75 total connections) as well. The true connectivity graphs for these simulations are shown as Figure 6.8. With pruning, we are able to infer both of these graphs from the spike data with perfect precision and recall (s_0=5 for Simulation #2, s_0=4 for Simulation #3). Figure 6.9 shows that pruning improves the F-measure performance of the test in both of these simulations for low settings of s_0.

6.3.2 Analysis of Cultured Cortical Neurons

Wagenaar et al. (2006) made available to the public an extensive set of multielectrode array (MEA) recordings from cultured cortical neurons. Half-hour recording

[4]These two connections, $11[6]-12$ and $12[3]-11$, constitute a cycle, thus our assumption that neuron 11 spikes as Bernoulli processes is violated. As stated in Sec. 6.2.1, our analysis method is technically valid only for directed acyclic graphs (DAGs). For our simulations, we chose the connections randomly and so did not force the network structure to be a DAG. We will come back to this point later in Sec. 6.4 section.

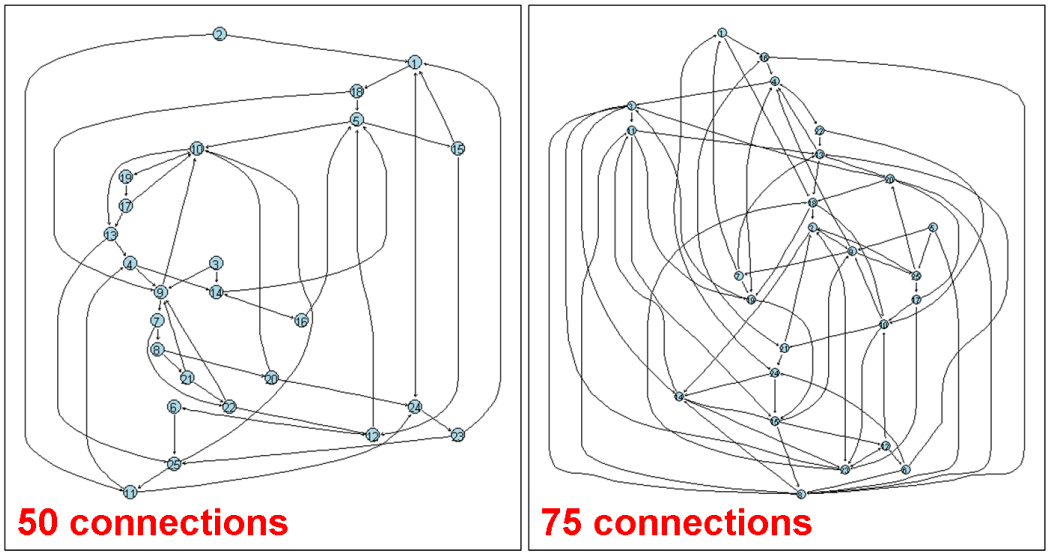

Figure 6.8: **(A)** For Simulation #2, each neuron has 2 post-synaptic targets for a total of 50 connections in the network. We can infer the true connectivity graph from the spike data with s_0=5 using pruning. **(B)** For Simulation #3, each neuron has 3 post-synaptic targets for a total of 75 connections. We can infer the true connectivity graph from the spike data with s_0=4 using pruning.

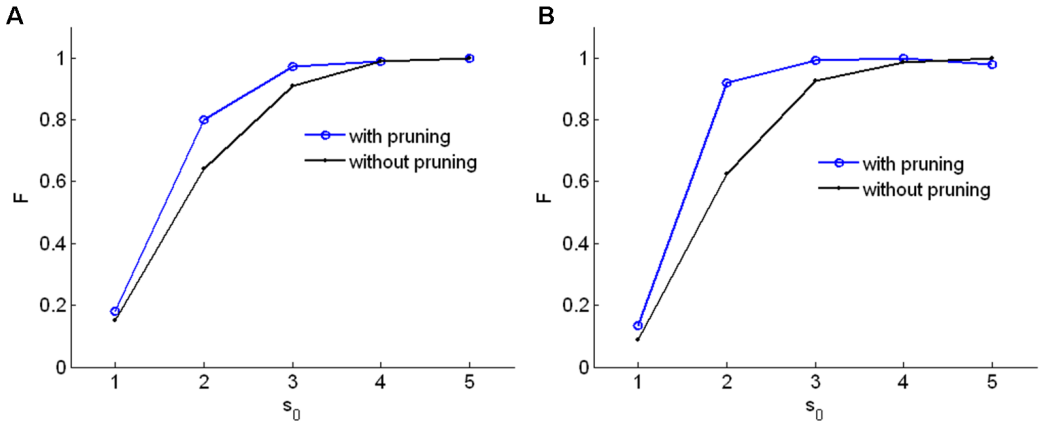

Figure 6.9: For Simulations #2 and #3, pruning gives a higher precision test for low settings of the s_0 threshold.

sessions were performed across 58 different cultures during their first five weeks of development. *Wagenaar et al.* (2006) focused on characterizing "population bursts" in the spiking activity of the cultures. Such bursts, defined as brief periods of time during which the firing rate of several cells or electrodes greatly exceeds the baseline rate, are a common feature observed in cultures of many different types of neurons. Here, our focus is not to characterize the bursts but rather to detect precisely timed spiking patterns involving multiple neurons. From these patterns we can estimate the strength of functional connectivity between different neurons in the culture. Our analysis methods assume that the firing rates of individual neurons are relatively stationary in the analysis window. Thus, for our analysis it is important that we choose analysis windows which do not contain bursts.

6.3.2.1 Data Pre-Processing

We began our analysis with culture 2-1-35, meaning the first culture from the second batch after 35 days *in vitro* (DIV). This culture was "densely" plated with approximately 50,000 cells, and on DIV 35 was characterized by *Wagenaar et al.* (2006) as having bursts of fixed size, with a frequency of between 2 and 10 bursts per minute. The input data for our analysis were the timestamps of the spikes recorded on 56 different electrodes (we did not work with the raw voltage waveforms themselves). For our analysis we discretized the time axis with a bin size of Δ=1 ms. To identify bursts we used the array-wide spike detection rate (ASDR) measure, defined in *Wagenaar et al.* (2006) as the number of spikes per unit time summed over all the electrodes in the array. Averaged over the entire 30 minute recording, the ASDR for a 100 ms window in culture 2-1-35 was about 20. We considered the culture to be bursting anytime the ASDR in a 100 ms window exceeded 50, corresponding to a 2.5-fold increase over the average. For example, we will consider the spikes in the first 120 seconds of recording from culture 2-1-35. In the raster plot shown in Figure

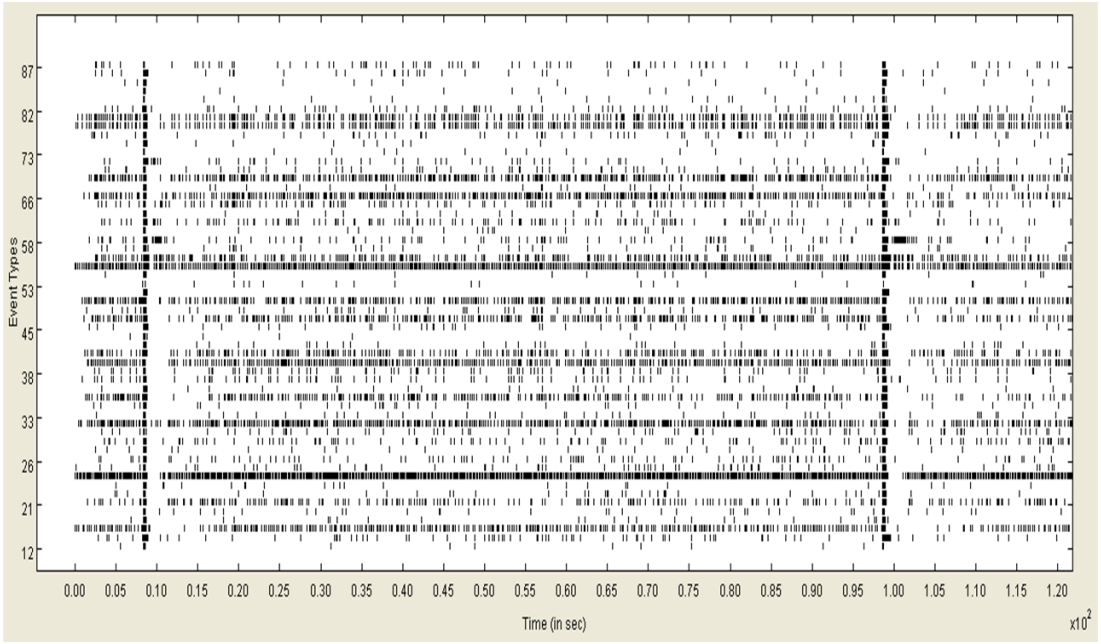

Figure 6.10: Spike raster of first 120 seconds from culture 2-1-35.

6.10, bursts are visible at around 10 and 100 seconds. In Figure 6.11, we see that the ASDR greatly exceeds the threshold of 50 during these bursts. The ASDR also exceeds 50 in windows around 40 and 57 seconds.

To obtain sections of the data suitable for our analysis, we looked for 20 second stretches which did not contain any windows that exceeded the threshold. Additionally, we required these 20 second segments to begin and end at least 2 seconds away from any window that exceeded the threshold (this was to avoid including any windows that happened to catch the very beginning of a burst, as well as the brief periods of extremely low spiking activity that appear to occur immediately following a burst). The first 120 seconds contained one such segment (60 to 80 seconds). In the 30 minutes of data from culture 2-1-35, we found 23 suitable segments. We analyzed each of these segments individually. (See Appendix C for an assessment of how well this dataset appears to meet our model assumptions).

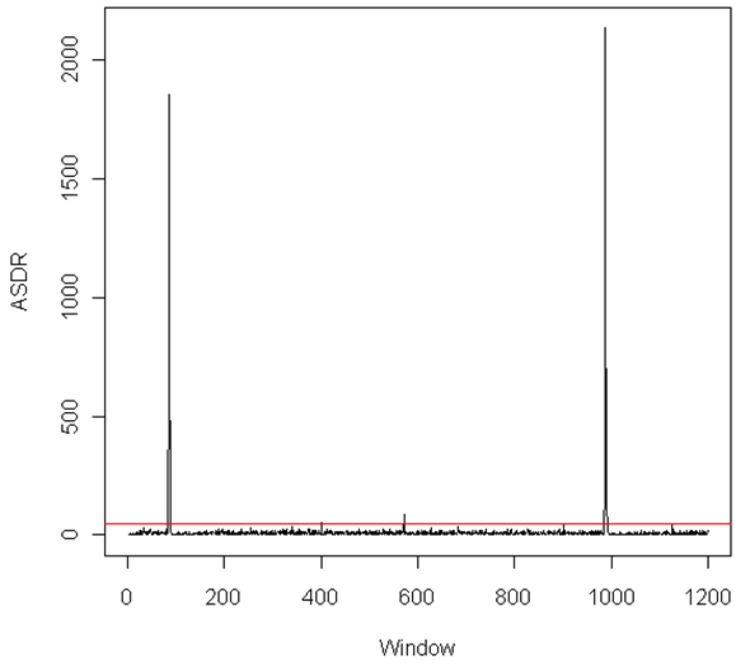

Figure 6.11: ASDR (window size 100 ms) of first 120 seconds from culture 2-1-35. Burst threshold of 50 shown in red.

6.3.2.2 Detecting Precisely Timed Spiking Patterns

In each segment, we looked for precisely timed spiking patterns by counting the number of non-overlapping occurrences of serial episodes. Recall that a 2-node serial episode is defined as a spike from any neuron i followed by a spike from another neuron j after a fixed delay of T time units. With 56 electrodes, there are 3,080 possible 2-node episodes (where $i \neq j$), and we counted the non-overlapping occurrences of all such episodes for $T = 1, 2, ..., 200$ ms. From these counts, we estimated the probability of each episode occurring in any bin using Equation 6.11, and then calculated 95% confidence intervals for each episode's $\hat{s}$ in each segment. If the lower confidence limit of $\hat{s}$ was greater than 1, then we considered that episode to be significant in that segment. We repeated this for each episode and each segment. Based on the set of significant 2-node episodes, we generated and counted candidate 3-node episodes and used these counts to obtain a CI for $\hat{s}'$ for each episode in each segment. Table 6.4 shows the 47 episodes that were significant in at least half of the 23 segments after

pruning of false edges.

#	$i[k]-j$		#	$i[k]-j$
1	37[6]-38		25	55[6]-77
2	42[1]-62		26	78[2]-77
3	78[1]-87		27	78[2]-48
4	68[1]-87		28	68[3]-77
5	41[2]-82		29	68[1]-78
6	41[1]-21		30	32[1]-21
7	78[1]-48		31	48[1]-46
8	42[1]-32		32	41[4]-21
9	48[1]-47		33	55[5]-77
10	78[1]-77		34	68[2]-78
11	41[3]-62		35	68[3]-48
12	46[1]-35		36	68[2]-77
13	42[1]-21		37	41[1]-32
14	68[1]-48		38	68[3]-78
15	41[1]-82		39	32[1]-46
16	41[3]-21		40	24[7]-28
17	41[2]-42		41	41[4]-32
18	41[3]-42		42	55[5]-78
19	55[1]-56		43	55[5]-48
20	41[4]-62		44	78[2]-68
21	77[1]-48		45	55[5]-68
22	68[1]-77		46	41[2]-32
23	78[1]-68		47	24[1]-32
24	41[3]-32			

Table 6.4: 2-node episodes significant in at least half of the 23 segments of culture 2-1-35

Although we considered episodes with delays of up to 200 ms, all the significant episodes had delays of less than 10 ms. Fast delays such as this are consistent with the timescale of the action for AMPA, a common excitatory neurotransmitter in the cortex.

Overall, our 2-node results are consistent with the patterns reported in a previous study of precisely timed patterns in these cultures (*Rolston et al.*, 2007). Specifically, of the thirteen 2-node patterns mentioned in *Rolston et al.* (2007), six of them were also found to be significant in our analysis (68-78, 78-77, 77-48, 41-42, 42-32, and 37-38).

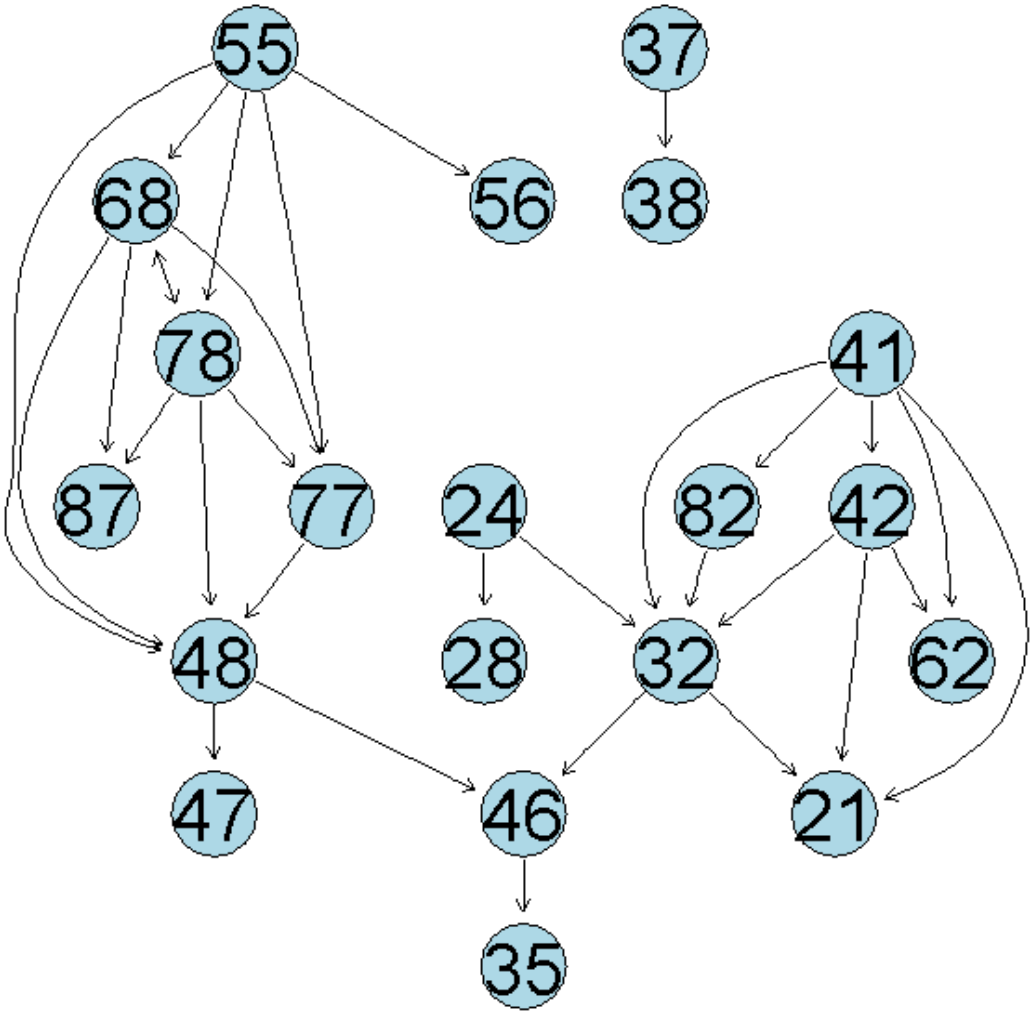

Figure 6.12: Functional connectivity in culture 2-1-35.

6.3.2.3 Tracking connections over time

To visualize the functional connectivity present in culture 2-1-35, we draw a network graph (Figure 6.12) based on our pruned list of significant 2-node episodes. If there is a significant episode with any delay for an $i-j$ pair, we draw a directed edge $i \rightarrow j$ connecting them.

We repeated our method for finding significant patterns in earlier recordings made from the same culture on DIV 33 and 34 (cultures 2-1-33 and 2-1-34). We find fewer significant connections on these days than we did on DIV 35, indicating that the

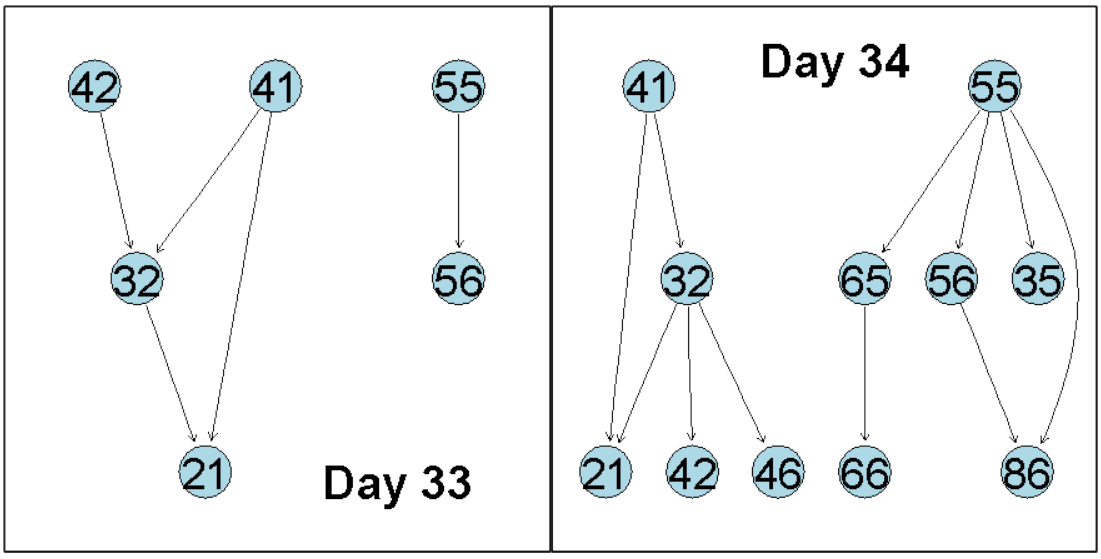

Figure 6.13: Functional connectivity in cultures 2-1-33 and 2-1-34.

connectivity in the culture is still evolving (Figure 6.13).

Some connections do show up as significant on all three days, namely 41-21 and 55-56. The 41-21 connection is actually significant at multiple different delays, as shown in Table 6.5.

$i[T] - j$	$\hat{s}_T$
55[1]-56	44.8
41[1]-21	67.8
41[3]-21	48.0
41[4]-21	22.2

Table 6.5: Average strength of 41[T]-21 and 55[T]-56 connections on 2-1-35

This may be due to multiple connections between 41 and 21, or due to a single connection with a variable, or "sloppy", delay. In either case, for the sake of comparison of the strength of connections among $i - j$ pairs it is useful to obtain some aggregate measure of the influence of i on j across multiple delays. We compute a strength ratio accounting for sloppy delays as follows. Say we are interested in delays 1 through n ms. If neurons i and j were independent, then the probability of a spike by neuron i being followed by a spike from neuron j in at least one of the following n time bins would simply be:

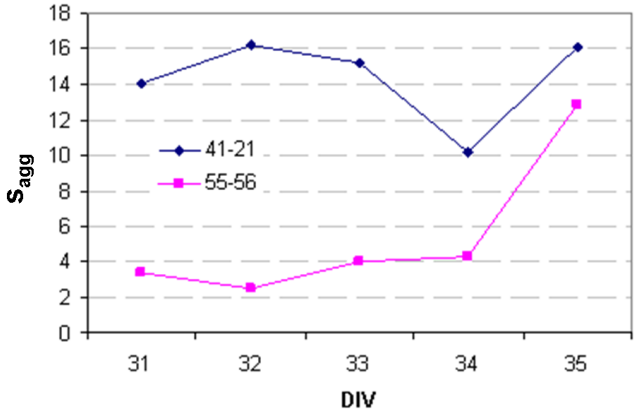

Figure 6.14: Average strength of connections 41→21 and 55→56 over several days.

$$P_{E_{agg}} = 1 - \prod_{T=1}^{n} (1 - P_{E_T}) \tag{6.15}$$

We calculated this aggregate $\hat{P}_{E_{agg}}$ for 41→21 and 55→56 with n=10. We then get an overall ratio as:

$$\hat{s}_{agg} = \frac{\hat{P}_{E_{agg}}}{n\hat{P}_i\hat{P}_j} \tag{6.16}$$

for culture 2-1 DIV 31 through 35 and plot the results as Figure 6.14.

We see that the strength of the 41→21 connection is relatively stable over the 5 days of recordings, while the strength of the 55→56 is relatively stable the first 4 days and then increases sharply on the last day.

6.4 Discussion

In this chapter, we developed a test of statistical significance for the number of non-overlapped occurrences of a serial episode. The motivation was that these are the type of counts obtained by data mining algorithms used in the literature to analyze multi-neuronal spike trains. We demonstrated through simulation of neuronal

networks that our methods are effective in estimating the strength of a connection between two neurons, and in inferring the graph representing functional connectivity among neurons. Due to our modeling assumption that neurons spike as Bernoulli processes, our methodology is technically valid only when the connectivity network among neurons is a directed acyclic graph. However, even when our simulated neuronal networks did include some cycles, our methods were still able to recover the connectivity graph. Nevertheless, methods that are technically valid for cyclic graphs will be explored in our future work.

Our method for inferring the connectivity graph uses 3-node episode counts to prune false edges that were determined to be significant at the 2-node level. In future work, we will extend this idea to higher-order structures, such as those represented by 4- and 5-node episodes. Doing so will require a framework that can handle the combinatorial difficulties associated with modeling higher-order patterns. In our preliminary work, directed loglinear models appear to be a promising solution to this problem (*Diekman et al.*, In Preparation).

CHAPTER VII

Conclusion

In Part I of this dissertation, we developed a detailed mathematical model of the electrophysiology of the SCN, the neuronal network responsible for the generation of circadian rhythms in mammals. In Part II, we developed statistical methods for inferring the functional connectivity of neuronal networks from multi-neuronal spike train data.

A natural extension of this dissertation is to infer the functional connectivity of the SCN from multi-neuronal spike train data recorded from SCN neurons. We will be pursuing this direction in future work. Some adjustments to our statistical methods may be required to make them well-suited for analysis of SCN data. For example, our methodology assumes stationarity of neuronal firing in the analysis window. While the electrical activity of SCN neurons is known to nonstationary on the 24-hour time scale, on a much shorter time scale the stationarity assumption may be reasonable. In addition, we have focused primarily on the detection of excitatory connections using our methods. Since the most prevalent neurotransmitter in the SCN is GABA, the majority of connections in the SCN are likely inhibitory. Our methods can be used to detect significant inhibitory connections, but doing so often requires a larger data analysis window. Larger analysis windows will increase the computational burden, and also potentially make the stationarity assumption less appropriate.

Several research groups have reported that GABA can also be excitatory in the SCN, but the extent of this phenomenon is not yet clear due to conflicts in the findings of the various reports. Most of these studies conducted intracellular recordings of SCN neurons. Instead, we could assess the evidence for excitatory connections in the SCN using extracellular recordings, by applying our statistical methods to SCN spike trains. *Freeman et al.* (2010) applied cross-correlation analysis to SCN spike trains, and found evidence for both excitatory and inhibitory communication between neurons. The level of connectivity was estimated to be 3-4% of that expected by all-to-all coupling. A study applying our methods to infer the level of connectivity in the SCN would provide a useful comparison to the results of *Freeman et al.* (2010).

The statistical methods we developed in Part II of this dissertation targeted assessing the significance of precise firing sequences with fixed time delays between neurons. Such sequential firing patterns were detected as *serial episodes*. A serial episode is an ordered tuple of event types (neurons), and is said to occur in the data stream only when the neurons making up the episode fire in the prescribed order. The frequent episode discovery framework can also be used to detect *parallel episodes* (*Patnaik et al.*, 2008). A parallel episode is an unordered set of neurons, and is said to occur in the data whenever all the neurons making up the episode fire within some prescribed time window, regardless of the order in which they fired. As such, counting the occurrences of parallel episodes in SCN spike trains could be used to detect evidence of the clustering of firing predicted by our SCN network model in Chapter 2. *Raajay* (2009) develops a method for estimating the statistical significance of parallel episodes. Alternatively, the computational algorithm presented in *Pipa et al.* (2008), NeuroXidence, could also be used to evaluate the evidence for clustering in SCN spike trains.

APPENDICES

APPENDIX A

Model Parameters and Equations

Model parameter values used for all simulations, unless specified otherwise in the text:

Table A.1: Parameter values

C	Whole cell capacitance	5.7 pF
g_{Na}	Sodium conductance	229 nS
E_{Na}	Sodium reversal potential	45 mV
g_K	Potassium conductance	14 ns (Ch. 2); 3 nS (Ch. 4)
E_K	Potassium reversal potential	-97 mV
g_{Ca}	Calcium conductance	65 nS (Ch. 2); 26 nS (Ch. 4)
E_{Ca}	Calcium reversal potential	61 mV (Ch. 2); 54 mV (Chs. 3,4)
g_L	Leak conductance	1/11 nS
E_L	Leak reversal potential	-29 mV (Ch. 2); -7 mV (Chs. 3,4)
$g_{K_{Ca}}$	Calcium-activated potassium conductance	4 nS

For the applied current (I_{app}) in Chapter 3, there were random IPSCs and EPSCs in Figs. 3.6-ACF, 3.8-ACF, 3.9-CEH, 3.10-ACF, and 3.12. There were random IPSCs in Figs. 3.6-B, 3.8-B, 3.9-D, and 3.10-B. There were random EPSCs in Figs. 3.6-DE, 3.8-DE, 3.9-FG, and 3.10-DE.

Equations for the gating variables of the voltage-dependent currents:

$$
\begin{aligned}
m_\infty &= \frac{1}{1+exp(-\frac{V+35.2}{8.1})} \\
\tau_m &= exp\left(-\frac{V+286}{170}\right) \\
h_\infty &= \frac{1}{1+exp(\frac{V+62}{4})} \quad \text{(Chs. 2,3)} \\
h_\infty &= \frac{1}{1+exp(\frac{V+62}{2})} \quad \text{(Ch. 4)} \\
\tau_h &= 0.51 + exp\left(-\frac{V+26.6}{7.1}\right) \\
n_\infty &= \frac{1}{(1+exp(\frac{V-14}{-17}))^{0.25}} \\
\tau_n &= exp\left(-\frac{V-67}{68}\right) \\
r_\infty &= \frac{1}{1+exp(-\frac{V+25}{7.5})} \\
\tau_r &= 3.1 \\
f_\infty &= \frac{1}{1+exp(\frac{V+260}{65})} \\
\tau_f &= exp\left(-\frac{V-444}{220}\right)
\end{aligned}
$$

APPENDIX B

Implementation of Existing Methods

The code used for performing spike jitter (*Date et al.*, 1998) and pattern jitter (*Harrison and Geman*, 2009) was downloaded from http://jitter.stat.cmu.edu. The source code for NeuroXidence (*Pipa et al.*, 2008) was downloaded from http://www.NeuroXidence.com. We used the NeuroXidence_Windowed_V3_34 Release.

Spike jitter: Each spike was independently and uniformly jittered over jitter windows of length L. This is repeated N times to create N surrogate spike trains. For the results reported in Fig. 5.6 we used the following parameter settings: N=1000, L=2 ms, $LMethod$ = 'centered', and $GMethod$ = 'integer'.

Pattern jitter: Again spikes are jittered over a window of length L, but the surrogate spike trains and the original spike train are required to have identical patterns of spiking (and not spiking) in the R bins preceding each spike (*Harrison and Geman*, 2009). The parameter R thus controls the amount of recent spike-history effects that are preserved. For the results reported in Fig. 5.6 we used the following parameter settings: N=1000, L=2 ms, R=50 ms, $LMethod$ = 'centered', and $GMethod$ = 'integer'.

NeuroXidence: While NeuroXidence is designed for analysis of synchronous spiking of neurons and not sequential patterns with fixed time delays, it can be used to analyze sequential patterns by shifting each spike train by the corresponding delays in the pattern to create synchronous spiking events (*Pipa et al.*, 2008). Therefore, for the analysis shown in Fig. 5.4, we first shifted the spike train of neuron I so that each spike occurred 8 ms earlier. Likewise we shifted the spike train of neuron C by 12 ms, neuron O by 6 ms, and neuron L by 11 ms. The 300 seconds of data was then divided up into 60 separate "trials" each 5 seconds in duration. The time scale of fine temporal cross-structures of interest, *Input.tau_c*, was set as 5 ms and the slow time scale, *Input.tau_r*, was set as 15 ms. NeuroXidence generates surrogate data by jittering entire spike trains by *Input.tau_r*. The number of surrogates was set as 25, and the p-values shown in Fig. 5.6 were the p-values for excess joint-spike events of I,S,C and W,O,L with the *Input.test_level* set at 0.01.

Smoothed Count Matrix: To implement the test for significance of precise firing sequences described in Sections 3.1 to 3.4 of *Abeles and Gat* (2001), a 20 ms by 20 ms count matrix was constructed and then smoothed using a Gaussian kernel with a standard deviation of 5 and a hole at (0,0) without correcting for edge effects. We only calculated p-values for our patterns of interest, I-S-C and W-O-L. The p-values reported in Fig. 5.6 do not include the adjustment shown as Eq. 3 in *Abeles and Gat* (2001).

APPENDIX C

Assessing the Model Assumptions

Our model for the occurrences of an episode assumes that the total number of occurrences, N, follows a binomial distribution with parameters $L-T$ and P_E. To test whether this assumption is appropriate for the cortical culture data analyzed here, we focused on the 41[1]-21 connection in culture 2-1-34. In this recording session, there were 63 different 20 second segments which did not contain and were not near any bursts. For each segment, we estimated $\hat{P}_E$ based on the number of occurrences of 41[1]-21 over the whole segment (L=20000), and then subdivided the segment further into 20 chunks. For each 1 s chunk, we then looked to see if we had 0, 1, or more than 1 occurrences of $41[1]-21$. The totals for each of these bins was then compared to what we would expect for a binomial distribution with a success probability of $\hat{P}_E$ with $L = 1000$. We performed a χ^2 goodness of fit test with 1 degree of freedom and P=0.05 for each of the 63 segments. The test failed to reject the null hypothesis in 58 out of the 63 segments, leading us to conclude that our model assumptions seem appropriate for this dataset.

BIBLIOGRAPHY

BIBLIOGRAPHY

Abeles, M. (1982), *Local Cortical Circuits: An Electrophysiological Study*, Springer-Verlang, New York.

Abeles, M. (1991), *Corticonics: Neural Circuits of the Cerebral Cortex*, Cambridge University Press, New York.

Abeles, M., and I. Gat (2001), Detecting precise firing sequences in experimental data, *J Neurosci*, *107*, 141–154.

Abeles, M., and G. Gerstein (1988), Detecting spatiotemporal firing patterns among simultaneously recorded single neurons, *J Neurophysiol*, *60*, 909–924.

Agrawal, R., T. Imielinski, and A. Swami (1993), Mining association rules between sets of items in large databases, *SIGMOD*, *22*, 207–216.

Amarasingham, A. (2004), *Statistical Methods for the Assessment of Temporal Structure in the Activity of the Nervous System*, Doctoral Dissertation, Division of Applied Mathematics, Brown University.

Antle, M., D. Foley, N. Foley, and R. Silver (2003), Gates and oscillators: a network model of the brain clock, *J Biol Rhythms*, *18*, 339–350.

Aton, S., and E. Herzog (2005), Come together, right... now: Synchronization of rhythms in a mammalian circadian clock, *Neuron*, *48*, 531–534.

Aton, S., C. Colwell, A. Harmar, J. Waschеck, and E. Herzog (2005), Vasoactive intestinal polypeptide mediates circadian rhythmicity and synchrony in mammalian clock neurons, *Nat Neurosci*, *8*, 476–18.

Belle, M., C. Diekman, D. Forger, and H. Piggins (2009), Daily electrical silencing in the mammalian circadian clock, *Science*, *326*, 281–284.

Bernard, S., D. Gonze, B. Cajavec, H. H, and A. Kramer (2007), Synchronization-induced rhymicity of circadian oscillators in the suprachiasmatic nucleus, *PLoS Comput Biol*, *3*, 667–679.

Booth, V., J. Rinzel, and O. Kiehn (1997), Compartmental model of vertebrate motoneurons for Ca^{2+}-dependent spiking and plateau potentials under pharmacological treatment, *J Neurophysiol*, *78*, 3371–3385.

Borisyuk, A., and J. Rinzel (2005), Understanding neuronal dynamics by geometrical dissection of minimal models, in *Models and Methods in Neurophysics*, *Proc Les Houches Summer School 2003, Elsevier*, vol. Session LXXXX, edited by C. Chow, B. Gutkin, D. Hansel, C. Meunier, and J. Dalibard, pp. 19–72.

Bouskila, Y., and F. Dudek (1993), Neuronal synchronization without calcium-dependent synaptic transmission in the hypothalamus, *Proc Natl Acad Sci USA*, *90*, 3207–3210.

Bouskila, Y., and F. Dudek (1995), A rapidly activating type of outward rectifier K^+ current and A-current in rat suprachiasmatic nucleus neurones, *J Physiol*, *488*, 339–350.

Brown, E., R. Kass, and P. Mitra (2004), Multiple neural spike train data analysis: state-of-the-art and future challenges, *Nat Neurosci*, *7*, 456–461.

Brown, T., and H. Piggins (2007), Electrophysiology of the suprachiasmatic circadian clock, *Prog Neurobiol*, *82*, 229–255.

Brown, T., and H. Piggins (2009), Spatiotemporal heterogeneity in the electrical activity of suprachiasmatic nucleus neurons and their response to photoperiod, *J Biol Rhythms*, *24*, 44–54.

Bush, W., and H. Siegelman (2006), Circadian synchrony in networks of protein rhythm drive neurons, *Complexity*, *12*, 67–72.

Chandrasekaran, L., V. Mateev, and A. Bose (2009), Multistability of clustered states in a globally inhibitory network, *Physica D*, *238*, 253–263.

Choi, H., et al. (2008), Excitatory actions of GABA in the suprachiasmatic nucleus, *J Neurosci*, *28*, 5450–5459.

Clay, J. (2009), Determining K+ channel activation curves from K+ channel currents often requires the Goldman-Hodgkin-Katz equation, *Front Cell Neurosci*, *3*, 1–6.

Cloues, R., and W. Sather (2003), Afterhyperpolarization regulates firing rate in neurons of the suprachiasmatic nucleus, *J Neurosci*, *23*, 1593–1604.

Conrad, E. (2006), *Bifurcation analysis and qualitative optimization of models in molecular cell biology with applications to the circadian clock*, Doctoral Dissertation, Department of Mathematics, Virginia Polytechnic Institute and State University.

Cutler, D., M. Haraura, H. Reed, S. Shen, W. Sheward, C. Morrison, H. Marston, A. Harmar, and H. Piggins (2003), The mouse VPAC(2) receptor confers suprachiasmatic nuclei cellular rhythmicity and responsiveness to vasoactive intestinal polypeptide in vitro, *Eur. J. Neurosci.*, *17*, 197–204.

Daan, S., and C. Berde (1978), Two coupled oscillators: Simulations of the circadian pacemaker in mammalian activity rhythms, *J Theor Biol*, *70*, 297–313.

Date, A., E. Bienenstock, and S. Geman (1998), *On the temporal resolution of neural activity*, Technical Report, Division of Applied Mathematics, Brown University.

Destexhe, A., and T. Sejnowski (2001), *Thalamocortical Assemblies: How ion channels, single neurons and large-scale networks organize sleep oscillations*, Oxford University Press, New York.

Diekman, C., K. Dasgupta, V. Nair, and K. Unnikrishnan (In Preparation), Statistical inference of functional connectivity in neuronal networks using frequent episodes.

Forger, D., and C. Peskin (2003), A detailed predictive movel of the mammalian circadian clock, *Proc Natl Acad Sci USA*, *100*, 14,806–14,811.

Forger, D., and C. Peskin (2005), Stochastic simulation of the mammalian circadian clock, *Proc Natl Acad Sci USA*, *102*, 321–324.

Forger, D., M. Jewett, and R. Kronauer (1999), A simpler model of the human circadian pacemaker, *J Biol Rhythms*, *14*, 532–537.

Forger, D., D. Gonze, D. Virshup, and D. Welsh (2007), Beyond intuitive modeling: Combining biophyscial models with innovative experiments to move the circadian clock field forward, *J Biol Rhythms*, *22*, 200–210.

Freeman, G., A. Webb, A. Sungwon, and E. Herzog (2008), For whom the bells toll: Networked circadian clocks, *Sleep Biol Rhythms*, *6*, 67–75.

Freeman, M., R. Krock, S. Aton, and E. Herzog (2010), Functional connectivity analysis in synchronized circadian networks, in *Society for Research on Biological Rhythms, Program Abstract P167*, 12th Biennial Meeting, Sandestin, FL.

Garcia-Ojalvo, J., M. Elowitz, and S. Strogatz (2004), Modeling a synthetic cellular clock: Rep, *Proc Natl Acad Sci USA*, *90*, 3207–3210.

Gerstein, G. (2004), Searching for significance in spatio-temporal firing patterns, *Acta Neurobiol Exp (Wars)*, *64*, 203–207.

Gillette, M., M. Medanic, A. McArthur, C. Liu, J. Ding, L. Faiman, E. Weber, T. Tcheng, and E. Gallman (1995), Intrinsic neuronal rhtyhms in the suprachiasmatic nuclei and their adjustment, in *Circadian Clocks and their Adjustment*, *CIBA Foundation Symposia*, vol. 183, pp. 134–144.

Golomb, D., and D. Hansel (2000), The number of synaptic inputs and the synchrony of large, sparse neural networks, *Neural Comput*, *12*, 1095–1139.

Golomb, D., and J. Rinzel (1994), Clustering in globally coupled inhibitory neurons, *Physica D*, *72*, 259–282.

Golomb, D., D. Hansel, B. Shraiman, and H. Sompolinsky (1992), Clustering in globally coupled phase oscillators, *Phys Rev A*, *45*, 3516–3530.

Gonze, D., S. Bernard, C. Waltermann, A. Kramer, and H. Herzel (2005), Spontaneous synchronization of coupled circadian oscillators, *Biophys J*, *89*, 120–129.

Guldner, F. (1984), Suprachiasmatic nucleus: Numbers of synaptic appositions and various types of synapses, *Cell Tissue Res*, *235*, 449–452.

Harrison, M., and S. Geman (2009), A rate and history-preserving resampling algorithm for neural spike trains, *Neural Comput*, *21*, 1244–1258.

Hatsopoulos, N., S. Geman, A. Amarasingham, and E. Bienenstock (2003), At what time scale does the nervous system operate?, *Neurocomputing*, *52*, 25–29.

Hebb, D. (1949), *The Organization of Behavior: A Neurophysiological Theory*, Wiley, New York.

Herzog, E. (2007), Neurons and networks in daily rhythms, *Nat Neurosci*, *8*, 790–802.

Hille, B. (2001), *Ion Channels of Excitable Membranes, 3rd Ed.*, Sinauer, Sunderland, MA.

Hines, M., T. Morse, M. Migliore, N. Carnevale, and G. Shepherd (2004), ModelDB: A Database to Support Computational Neuroscience, *J Comput Neurosci*, *17*, 7–11.

Hodgkin, A., and A. Huxley (1952), A quantitative description of membrane current and its application to conduction in nerve, *J Physiol*, *117*, 500–544.

Ikeda, M., T. Sugiyama, C. Wallace, H. Gompf, T. Yoshioka, A. Miyawaki, and C. Allen (2003), Circadian dynamics of cytosolic and nuclear Ca^{2+} in single suprachiasmatic nucleus neurons, *Neuron*, *38*, 253–263.

Ikegaya, Y., G. Aaron, R. Cossart, D. Aronov, I. Lampl, and D. e. a. Ferster (2004), Synfire chains and cortical songs: temporal modules of cortical activity, *Science*, *304*, 559–564.

Indic, P., W. Schwartz, E. Herzog, N. Foley, and M. Antle (2007), Modeling the behavior of coupled cellular oscillators in the suprachiasmatic nucleus, *J Biol Rhythms*, *22*, 211–219.

Indic, P., W. Schwartz, and D. Paydarfar (2008), Design principles for phase-splitting behaviour of coupled cellular oscillators: Clues from hamsters with 'split' circadian rhythms, *Journal of the Royal Society Interface*, *5*, 873–883.

Irwin, R., and C. Allen (2009), GABAergic signaling induces divergent neuronal Ca^{2+} responses in the suprachiasmatic nucleus network, *Eur J Neurosci*, *30*, 1462–1475.

Izhikevich, E. (2007), *Dynamical Systems in Neuroscience*, MIT Press, Cambridge, MA.

Jackson, A., G. Yao, and B. Bean (2004), Mechanism of spontaneous firing in dorsomedial suprachiasmatic nucleus neurons, *J Neurosci*, *24*, 7985–7998.

Jobst, E., and C. Allen (2002), Calbindin neurons in the hamster suprachiasmatic nucleus do not express a circadian rhythm in spontaneous firing rate, *Eur J Neurosci*, *16*, 2469–2474.

Kim, H., and J. Jeong (2008), Computational modeling of circadian rhythms in suprachiasmatic nucleus neurons, in *Lecture Notes in Computer Science*, *Springer-Verlag Berlin Heidelberg*, vol. 4985.

Kim, Y., and F. Dudek (1992), Intracellular electrophysiological study of suprachiasmatic nucleus neurons in rodent: Inhibitory synaptic mechanisms, *J Physiol*, *458*, 247–260.

Klein, D., R. Moore, and S. Reppert (1991), *Suprachiasmatic Nucleus: The Mind's Clock*, Oxford University Press.

Koch, C. (1999), *Biophysics of Computation*, Oxford University Press, New York.

Kononenko, N., and N. Berezetskaya (2010), Modeling the spontaneous activity in suprachiasmatic nucleus neurons: Role of cation single channels, *J Theor Biol*.

Kononenko, N., and F. Dudek (2004), Mechanism of irregular firing of suprachiasmatic nucleus neurons in rat hypothalamic slices, *J Neurophysiol*, *91*, 267–273.

Kronauer, R., D. Forger, and M. Jewett (1999), Quantifying human circadian pacemaker response to brief, extended, and repeated light stimuli over the phototopic range, *J Biol Rhythms*, *14*, 500–515.

Kuhlman, S., and D. McMahon (2004), Rhythmic regulation of membrane potential and potassium current persists in SCN neurons in the absence of environmental input, *Eur J Neurosci*, *20*, 1113–1117.

Laxman, S., P. Sastry, and K. Unnikrishnan (2005), Discovery of frequent episdoes and learning hidden markov models: A formal connection, *IEEE Transactions on Knowledge and Data Engineering*, *1*, 1505–1517.

Laxman, S., P. Sastry, and K. Unnikrishnan (2007), A fast algorithm for finding frequent episodes in event streams, in *Proc. ACM SIGKDD Int. Conf. Knowledge Discovery and Data Mining*, San Jose, CA.

Leloup, J., and A. Goldbeter (2003), Toward a detailed computational model for the mammalian circadian clock, *Proc Natl Acad Sci USA*, *100*, 7051–7056.

Liu, A., et al. (2007), Intercellular coupling confers robustness against mutation in the SCN circadian clock network, *Cell*, *129*, 605–616.

Lundkvist, G., and G. Block (2005), Role of neuronal membrane events in circadian rhythm generation, *Methods Enzymol*, *393*, 623–642.

Mannila, H., H. Toivonen, and A. Verkamo (1997), Discovery of frequent episdoes in event sequences, *Data Mining and Knowledge Discovery*, *1*, 259–289.

McCormick, D., and J. Huguenard (1992), A model of the electrophysiological properties of thalamocortical relay neurons, *J Neurophysiol*, *68*, 1384–1400.

Moore, R., and R. Silver (1998), Suprachiasmatic nucleus organization, *Chronobiol Int*, *15*, 475–487.

Mrugala, M., P. Zlomanczuk, A. Jagota, and W. Schwartz (2000), Rhythmic multiunit neural activity in slices of hamster suprachiasmatic nucleus reflect prior photoperiod, *Am. J. Physiol. Regul. Integr. Comp. Physiol.*, *278*, R987–R994.

Nadasdy, Z., H. Hirase, A. Czurko, J. Csicsvari, and G. Buzsaki (1999), Replay and time compression of recurring spike sequences in the hippocampus, *J Neurosci*, *19*, 9497–9507.

Nitabach, M., J. Blau, and T. Holmes (2002), Electrical silencing of *Drosophila* pacemaker neurons stops the free-running circadian clock, *Cell*, *109*, 485–495.

Nitabach, M., T. Holmes, and J. Blau (2005), Membranes, ions, and clocks: testing the Njus-Sulzman-Hastings model of the circadian oscillator, *Methods in Enzymology*, *393*, 682–693.

Okuda, K. (1993), Variety and generality of clustering in globally coupled oscillators, *Physica D*, *63*, 424–436.

Pakhotin, P., A. Harmar, A. Verkhratsky, and H. Piggins (2006), VIP receptors control excitability of suprachiasmatic nuclei neurons, *Pflugers Arch*, *452*, 7–15.

Patnaik, D., P. Sastry, and K. Unnikrishnan (2008), Inferring neuronal network connectivity from spike data: a temporal data mining approach, *Sci Programm*, *16*, 49–77.

Paydarfar, D., D. Forger, and J. Clay (2006), Noisy inputs and the induction of on-off switching behavior in a neuronal pacemaker, *J Neurophysiol*, *96*, 3338–3348.

Pennartz, C., R. Hamstra, and A. Geurtsen (2001), Enhanced NMDA receptor activity in retinal inputs to the rat suprachiasmatic nucleus in the subjective night, *J Physiol*, *532*, 181–194.

Pennartz, C., M. de Jeu, N. Bos, J. Schaap, and A. Geurtsen (2002), Diurnal modulation of pacemaker potentials and calcium current in the mammalian circadian clock, *Nature*, *416*, 286–290.

Piggins, H., and D. Cutler (2003), The roles of vasoactive intestinal polypeptide in the mammalian circadian clock, *J Endocrinology*, *177*, 7–15.

Pipa, G., D. Wheeler, W. Singer, and N. D (2008), NeuroXidence: reliable and efficient analysis of an excess or deficiency of joint-spike events, *J Comput Neurosci*, *25*, 64–88.

Pitts, G., H. Ohta, and D. McMahon (2006), Daily rhythmicity of large-conductance Ca^{2+}-activated K^+ currents in suprachiasmatic nucleus neurons, *Brain Research*, *1071*, 54–62.

Press, W., S. Teukolsky, W. Vetterling, and B. Flannery (1992), *Numerical Recipes in C*, Cambridge University Press, New York.

Prut, Y., E. Vaadia, H. Bergman, I. Haalman, H. Slovin, and M. Abeles (1998), Spatiotemporal structure of cortical activity: properties and behavioral relevance, *J Neurophysiol*, *79*, 2857–2874.

Quintero, J., S. Kuhlman, and D. McMahon (2003), The biological clock nucleus: A multiphasic oscillator network regulated by light, *J Neurosci*, *23*, 8070–8076.

Raajay, V. (2009), *Frequent episode mining and multi-neuronal spike train data analysis*, Master's Thesis, Department of Electrical Engineering, Indian Institute of Science.

Rinzel, J., and G. Ermentrout (1998), Analysis of neural excitability and oscillations, in *Methods in Neuronal Modeling, 2^{nd} Ed.*, MIT Press, Cambridge, MA, pp. 251–292.

Rohling, J., J. Meijer, H. Vanderleest, and J. Admiraal (2006a), Phase differences between SCN neurons and their role in photoperiodic encoding; a simulation of ensemble patterns using single unit electrical activity, *J Physiol Paris*, *100*, 261–270.

Rohling, J., L. Wolters, and J. Meijer (2006b), Simulation of day-length encoding in the SCN: From single-cell to tissue-level organization, *J Biol Rhythms*, *21*, 301–313.

Rolston, J., D. Wagenaar, and S. Potter (2007), Precisely timed spatiotemporal patterns of neural activity in dissociated cell cultures, *Neuroscience*, *148*, 294–303.

Ross, S. (1996), *Stochastic Processes, 2nd Ed*, Wiley, USA.

Sastry, P., and K. Unnikrishnan (2010), Conditional probability-based significance tests for sequential patterns in multi-neuronal spike trains, *Neural Comput*, *22*, 1025–1059.

Sim, C., and D. Forger (2007), Modeling the electrophysiology of suprachiasmatic nucleus neurons, *J Biol Rhythms*, *22*, 445–453.

Somjen, G. (2004), *Ions in the Brain*, Oxford University Press, New York.

Song, S., P. Sjostrom, M. Reigl, S. Nelson, and D. Chklovskii (2005), Highly nonrandom features of synaptic connectivity in local cortical circuits, *PLoS Biol*, *3*, 507–519.

Strogatz, S. (2000), From Kuramoto to Crawford: Exploring the onset of synchronization in populations of coupled oscillators, *Physica D*, *143*, 1–20.

Terman, D., S. Ahn, X. Wang, and W. Just (2008), Reducing neural networks to discrete dynamics, *Physica D*, *237*, 324–338.

Teshima, K., S. Kim, and C. Allen (2003), Characterization of an apamin-sensitive potassium current in suprachiasmatic nucleus neurons, *Neuroscience*, *120*, 65–73.

Tetko, I., and A. Villa (2001), A pattern grouping algorithm for analysis of spatiotemporal patterns in neuronal spike trains. 1.Detection of repeated patterns, *J Neurosci Methods*, *105*, 1–14.

Tiesinga, P., and J. Jose (2000), Synchronous clusters in a noisy inhibitory neural network, *Journal of Computational Neuroscience*, *9*, 49–65.

Tischkau, S., J. Mitchell, S. Tyan, G. Buchanan, and M. Gillette (2003), Ca^{2+}/cAMP response element-binding protein (CREB)-dependent activation of Per1 is required for light-induced signaling in the suprachiasmatic nucleus circadian clock, *J. Biol. Chem.*, *278*, 718–723.

To, T., M. Henson, E. Herzog, and F. Doyle (2007), A molecular model for intercellular synchronization in the mammalian circadian clock, *Biophys J*, *92*, 3792–3803.

Traub, R., M. Whittington, S. Colling, G. Buzsaki, and J. Jeffreys (1996), Analysis of gamma rhythms in the rat hippocampus in vitro and in vivo, *J Physiol*, *493*, 471–484.

van Rijsbergen, C. (1979), *Information Retrieval*, Butterworths, London.

Vasalou, C., and M. Henson (2010), A multiscale model to investigate circadian rhythmicity of pacemaker neurons in the suprachiasmatic nucleus, *PloS Comput Biol*, *6*, 1–15.

Verkhratsky, A., and E. Toescu (1998), *Integrative Aspects of Calcium Signalling*, Springer, London.

Wagenaar, D., J. Pine, and S. Potter (2006), An extremely rich repertoire of bursting patterns during the development of cortical cultures, *BMC Neuroscience*, *7*, 1–18.

Wagner, S., M. Castel, H. Gainer, and Y. Yarom (1997), GABA in the mammalian suprachiasmatic nucleus and its role in diurnal rhythmicity, *Nature*, *387*, 598–603.

Welsh, D., D. Logothetis, M. Meister, and S. Reppert (1995), Individual neurons dissociated from rat suprachiasmatic nucleus neurons dissociated from rat suprachiasmatic nucleus express independently phased circadian firing rhythms, *Neuron*, *14*, 697–706.

White, J., J. Rubinstein, and A. Kay (2000), Channel noise in neurons, *Trends Neurosci*, *23*, 131–137.

Wong, K., F. Dunn, and D. Berson (2005), Photoreceptor adaptation in intrinsically photosenstive retinal ganglion cells, *Neuron*, *48*, 1001–1010.

Wu, Y., G. Cao, and M. Nitabach (2008), Electrical silencing of PDF neurons advances the phase of non-PDF clock neurons in Drosophila, *J Biol Rhythms*, *23*, 117–128.

Yamada, W., C. Koch, and P. Adams (1998), Multiple channels and calcium dynamics, in *Methods in Neuronal Modeling: From Ions to Networks, 2nd Ed.*, MIT Press, Cambridge, MA.